JYU DISSERTATIONS 96

Maris Tali

Single-Event Radiation Effects in Hardened and State-of-the-art Components for Space and High-Energy Accelerator Applications

UNIVERSITY OF JYVÄSKYLÄ
FACULTY OF MATHEMATICS AND SCIENCE

JYU DISSERTATIONS 96

Maris Tali

Single-Event Radiation Effects in Hardened and State-of-the-art Components for Space and High-Energy Accelerator Applications

Esitetään Jyväskylän yliopiston matemaattis-luonnontieteellisen tiedekunnan suostumuksella julkisesti tarkastettavaksi yliopiston Ylistönrinteen salissa FYS1 kesäkuun 6. päivänä 2019 kello 12.

Academic dissertation to be publicly discussed, by permission of the Faculty of Mathematics and Science of the University of Jyväskylä, in Ylistönrinne, auditorium FYS1, on June 6, 2019 at 12 o'clock noon.

JYVÄSKYLÄN YLIOPISTO
UNIVERSITY OF JYVÄSKYLÄ

JYVÄSKYLÄ 2019

Editors
Timo Sajavaara
Department of Physics, University of Jyväskylä
Timo Hautala
Open Science Centre, University of Jyväskylä

Cover illustration: Freepik.com

Copyright © 2019, by University of Jyväskylä

Permanent link to this publication: http://urn.fi/URN:ISBN:978-951-39-7794-8

ISBN 978-951-39-7794-8 (PDF)
URN:ISBN:978-951-39-7794-8
ISSN 2489-9003

Abstract

Tali, Maris
Single-Event Radiation Effects in Hardened and State-of-the-art Components for Space and High-Energy Accelerator Applications
Jyväskylä: University of Jyväskylä, 2019, 105 p.
(JYU Dissertations
ISSN 2489-9003; 96;)
ISBN 978-951-39-7794-8 (PDF)
Diss.

In this work, the physical mechanisms of electron-induced single-event effects have been studied. Simulations using Monte Carlo codes such as FLUKA have been performed to study in more detailed the mechanisms by which electrons deposit charge in the sensitive volumes in modern electronic devices. Experimental results from several irradiation campaigns at facilities such as VESPER at CERN in Geneva, Switzerland, and RADEF in Jyväskylä, Finland have shown that electron-induced single-event effects are possible. Furthermore, experimental results suggest that these events can occur in even larger technology nodes as several device generations have been tested. Proof for potentially destructive single-event latch-up event has been shown both through experimental results and through simulations. In addition, the impact of low-energy protons in a mixed-field environment has been evaluated through simulations and through experimental campaigns at both the CHARM facility at CERN and at the RADEF facility. Recommendations for radiation hardness assurance for environments with an abundance of electrons such as the ESA JUICE mission have been made and a comparison to the more traditional strategies has been performed.

Keywords: Single-event effects, single-event upsets, electrons, radiation hardness assurance (RHA)

Preface

The work presented at this thesis has been carried out between 2015 and 2019 at CERN, the European Space Agency (ESA) and the University of Jyväskylä as a co-funded collaboration project.

First and foremost, I would like to thank my official supervisor at CERN - Rubén García Alía. I could not have asked for a better supervisor to guide me through my Ph.D. Your endless positivity, the long discussions about the research and the invaluable amount of support in my scientific endeavors is something I truly value. I believe this thesis would not have been possible without your support. Additionally, the first official supervisor at CERN, Markus Brugger, who is the reason I started my Ph.D and whose valuable input I always appreciated. Additionally, a huge thank you to Wilfrid Farabolini who spent countless hours helping me setting up the experiments and running the beam at the VESPER facility and of course also to the facility manager Roberto Corsini.

Secondly, I would like to thank the supervisors at the University of Jyväskylä, Arto Javanainen and Ari Virtanen. Thank you for the support for both the irradiation campaigns and for the guidance and advice for my research. Additionally, for helping me to navigate the way to completing my thesis, I am truly grateful for the organization and advice. Additionally, I would like to thank the RADEF collaboration for assistance for both the experimental and scientific work that was part of my thesis.

Thirdly, I would like to thank everyone who helped me at the European Space agency, Veronique Ferlet-Cavrois, Giovanni Santin, Cesar Boatella Polo and Ali Mohammadzadeh for the valuable scientific input for my research. Thank you also to Michele Muschitiello and Alessandra Costantino for the technical help at the irradiation facility and during experimental campaigns. Lastly, I would like to thank Eamon Daly who is the reason I started this Ph.D.

I would also like to thank Thijs for his unwavering support during the long process of writing and finishing the thesis. I greatly value your positivity and encouragement during these last months. Also, thank you to my closest friends at CERN: Tobias, Melanie and Romy. You have provided an invaluable amount of support and advice and I can not even begin to express how grateful I am to be able to have amazing friends like you. And of

course also to my other friends at CERN who are truly too many to fit in these pages.

Lastly, I would like to thank my family. Especially my mother, who is truly the reason why I chose to follow a technical field, why I am doing research and who made me believe I can do anything I want. Thank you also for the rest of my family for always being there when I needed them.

Contents

Abstract i

Preface iii

List of First Author Publications vii

List of Other Publications vii

1 Introduction 1

2 Background 5
- 2.1 Radiation Interaction with Matter . . . 5
- 2.2 Rutherford or Coulomb Scattering . . . 7
- 2.3 Electro- and Photo-Nuclear Interactions . . . 8
- 2.4 Radiation Effects in Electronics . . . 8
- 2.5 Electron-Induced SEE . . . 8

3 Simulation Tools 11
- 3.1 Monte Carlo Method . . . 11
- 3.2 FLUKA . . . 12
- 3.3 Spenvis/GRAS . . . 13
- 3.4 CRÉME MC . . . 15

4 Radiation Environments and Tested Devices 17
- 4.1 Jovian Radiation Environment . . . 17
- 4.2 VESPER Test Bench . . . 21
- 4.3 RADEF Facility . . . 28
- 4.4 CERN Radiation Environment and CHARM Facility . . . 31
- 4.5 Devices Overview . . . 32

5 Radiation Effects Simulation 37
- 5.1 Inelastic Interactions . . . 38
- 5.2 Silicon Recoils and Fragments . . . 39

5.3 Tungsten Fission Fragment Simulation 41
5.4 Monte Carlo Method for Estimation of SEE Rates 44
5.5 Energy Deposition Simulation 47
5.6 Effect of Tungsten on the Energy Deposition 52
5.7 Shielding Thickness and Material Impact on SEE Rates 54

6 Electron Single Event Upsets Testing 61
6.1 ESA SEU Monitor Electron Irradiation Results 61
6.2 Artix-7 BRAM Electron Irradiation Results 64

7 Electron Single-Event Latchup Testing 67
7.1 Brilliance Experimental Results 68
7.2 ISSI Experimental Results 68
7.3 Alliance Experimental Results 69
7.4 TID Effects Observed During SEL Testing 70
7.5 FLUKA Estimation of the SEL Cross-Sections 71

8 Low-Energy Proton Testing 75
8.1 Heavy Ion Testing of SRAM Memories 75
8.2 Proton Testing of the SRAM Memories 76
8.3 Low-Energy Proton Testing of Artix-7 80
8.4 Mixed-Field Testing of the SRAM Memories 81

9 Discussion and Radiation Hardness Assurance Implications 87
9.1 Possible Alternative Causes of Electron-Induced SEE 87
9.2 Electron-Induced SEE RHA 88
9.3 SEU Rate in the Jovian Atmosphere 90
9.4 Low-Energy Proton and Electron Contribution to the Mixed-Field 92

10 Conclusions and Future Work 95
10.1 Conclusions 95
10.2 Future Work 96

Bibliography 99

Publications 107

List of First Author Publications

The following publications are written in their entirety by the first author, all experiments were conducted, and text was written and all plotting and simulations were performed solely by the first author. The thesis is mainly based on the following articles, and they are also appended at the end of the thesis.

I M. Tali, R. Alia, M. Brugger, R. Corsini, W. Farabolini, V. Ferlet-Cavrois, A. Mohammadzadeh, G. Santin, and A. Virtanen, “High-energy Electron Induced SEUs and Jovian Environment Impact,” *IEEE Trans. Nucl. Sci.*, vol. 64, no. 8, pp. 2016 – 2022, Aug 2017

II M. Tali, R. Garcia Alia, M. Brugger, V. Ferlet-Cavrois, R. Corsini, W. Farabolini, A. Javanainen, M. Kastriotou, H. Kettunen *et al.*, “Mechanisms of Electron-Induced Single-Event Upsets in Medical and Experimental Linacs,” *IEEE Trans. on Nucl. Sci.*, vol. 65, no. 8, pp. 1715 – 1723, Jun 2018

III M. Tali, R. G. Alia, M. Brugger, V. Ferlet-Cavrois, R. Corsini, W. Farabolini, A. Javanainen, G. Santin, C. B. Polo, and A. Virtanen, “Mechanisms of electron-induced single event latchup,” *IEEE Trans. on Nucl. Sci.*, Aug 2018

List of Other Publications

The author provided either plots or information about the VESPER facility, or was part of the experimental campaign and provided some analysis for the beam conditions for the following publications

I R. G. Alía, P. F. Martínez, M. Kastriotou, M. Brugger, J. Bernhard, M. Cecchetto, F. Cerutti, N. Charitonidis, S. Danzeca *et al.*, “Ultra-Energetic Heavy Ion Beams in the CERN Accelerator Complex for Radiation Effects Testing,” *IEEE Transactions on Nuclear Science*, 2018

II R. G. Alia, M. Brugger, M. Cecchetto, F. Cerutti, S. Danzeca, M. Delrieux, M. Kastriotou, M. Tali, S. Uznanski *et al.*, "SEE testing in the 24 GeV proton beam at the CHARM facility," *IEEE Trans. on Nucl. Sci.*, vol. 65, no. 8, pp. 1750 – 1758, Apr. 2018

III F. Pozzi, R. Garcia Alia, M. Brugger, P. Carbonez, S. Danzeca, B. Gkotse, M. Richard Jaekel, F. Ravotti, M. Silari, and M. Tali, "CERN irradiation facilities," *Radiation protection dosimetry*, pp. 1–5, 2017

IV M. Glorieux, A. Evans, T. Lange, A.-D. In, D. Alexandrescu, C. Boatella-Polo, R. G. Alía, M. Tali, C. U. Ortega *et al.*, "Single-Event Characterization of Xilinx UltraScale+® MPSOC under Standard and Ultra-High Energy Heavy-Ion Irradiation," in *2018 IEEE Nuclear & Space Radiation Effects Conference (NSREC 2018).* IEEE, 2018, pp. 1–5

Author Maris Tali
Department of Physics / EN-STI-BMI / TEC-QEC
University of Jyväskylä / CERN / ESA/ESTEC
Finland / Geneva, Switzerland / Noordwijk, Netherlands

Supervisors Dr. Arto Javanainen
Department of Physics
University of Jyväskylä
Finland

Professor Ari Virtanen
Department of Physics
University of Jyväskylä
Finland

Dr. Ruben Garcia Alia
Engineering Department, STI/BMI section
CERN
Geneva, Switzerland

Dr. Cesar Boatella Polo
Technology Department
ESA/ESTEC
Noordwijk, Netherlands

Reviewers Research Assistant Professor Brian Sierawski
Institute for Space and Defense Electronics
Vanderbilt University
Nashville, Tennessee, USA

Dr. Marta Bagatin
Department of Information Engineering
University of Padova
Padova, Italy

Opponent Dr. Luigi Dilillo
Laboratory of Informatics, Robotics, and Microelectronics
Université de Montpellier
Montpellier, France

1 Introduction

High-energy physics experiments often feature environments of extreme radiation. Modern accelerators require large amounts of electronics both close to the accelerator ring itself and in nearby shielded alcoves. These electronics have to endure a high dose and a large flux of high-energy particles while at the same time operating reliably to provide high availability of the beam for the experiments. One of these large high-energy accelerators is the Large Hadron Collider at CERN in Geneva, Switzerland.

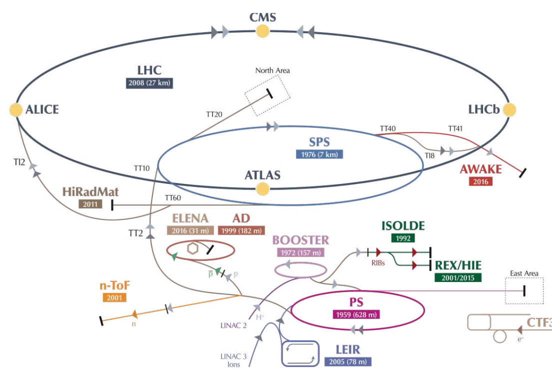

Figure 1.1: The CERN accelerator complex [8]

The proton beams inside the LHC reach energies of 7 TeV, and the beam-machine interactions produce a complex field of radiation. The CERN Radiation to Electronics (R2E) project was created to prevent unexpected beam dumps due to electronic failures. Its first mission was to mitigate the radiation damage in devices and later to conduct research into new radiation induced effects. Whereas a large amount of research exists for radiation induced damage by protons and neutrons, more research was needed into the damage caused by the mixed-field environment in which the electronics reside. For this purpose, the CHARM mixed-field facility was conceived [9]. In addition to evaluating the devices for potential mixed-field specific effects, the contributions from more rarely considered particles such as electrons and low-energy protons can be assessed, which are the focus of this work.

Similar to high-energy physics, modern space missions carry a large amount of highly-integrated electronic devices. These electronics have to endure the harsh radiation en-

vironment of space. Some radiation environments within our solar system pose unique challenges to the space missions. One of these missions is the JUICE mission by the European Space Agency (ESA), whose main task is to study the Jovian system and the icy moons of Jupiter [10, 11]. The Jovian system is characterized by high fluxes of trapped proton and electron radiation, the last of which is especially unique compared to the more common earth radiation environments. The highest energies of trapped electrons can read up to ~ 200 MeV, which is significantly higher than the ~ 5 MeV at the trapped radiation belts of the earth.

Figure 1.2: An illustration of the spacecraft for the JUICE mission to the Jovian system [12]

As the need for larger storage and lower power increases, the feature size of components has been steadily decreasing. As predicted in [13], the decreasing size of the active parts will lead to increased failures, both temporary and permanent. It was anticipated that modern sub-micron technologies would become susceptible to muons from cosmic ray showers in ground level applications. Highly integrated devices have been shown to be sensitive to singly charged particles, including protons, muons, and even electrons [14, 15] as well as to be sensitive to indirect ionization events [16]. Although modern devices are characterized mostly in terms of their sensitivity to neutrons, protons, and heavy ions, in recent years, partly due to the conception of the ESA JUICE mission, an increased interest in electron-induced SEE has driven further research and experiments exploring the subject [1, 16, 17].

This thesis will analyze the mechanisms by which these low-ionizing particles, with emphasis on electrons and low-energy protons, induce errors in highly-integrated devices. A thorough analysis through simulation and complementary experimental campaigns has been conducted. A new electron irradiation facility located at CERN, the VESPER facility [1], has been customized and calibrated to suit the needs of electronics irradiation campaigns. Also, tests at low-energy proton, intermediate-energy electron and heavy ion facility at RADEF have been performed. Moreover, the effect that the low-energy particles might have on a mixed-field environment such as the one present at the LHC was evaluated, through experiments at the CHARM facility at CERN.

All spacecraft deploy various thicknesses and materials of shielding to protect the electronics within. The usual choice for shielding thickness is dependent on the radiation environment and as a rule, is chosen as light as possible to save on the weight of the mission while at the same time providing enough protection. As a general rule, the thicker the shielding, the safer the sensitive devices inside. However, this notion is challenged in the presence of high-energy electrons, such as in the Jovian environment. As the trapped radiation passes through shielding, the secondary radiation generated by this interaction is another aspect that has to be taken into account. As the electrons pass through matter, they produce large amounts of photons through the process called Bremsstrahlung ("braking" radiation), which in return poses a threat to the electronics within the spaceship. This thesis will analyze the implications of this secondary effect and try to quantify the impact on a real mission, on the example of the JUICE mission.

2 Background

Highly-integrated electronic devices are an irreplaceable part of any modern technology-driven industry. Due to the ever-growing need for larger storage, speed and low power, the transistor sizes have been steadily decreasing with the number of them on single chips increasing rapidly. All electronics are to a varying degree vulnerable to radiation effects. The effects are stochastic by nature and therefore cannot be precisely predicted. Due to the higher level of integration and smaller transistor sizes, and therefore lower nominal supply voltages, the devices are becoming more sensitive to some of these effects.

In applications requiring high reliability, the quantification of the radiation effects in the systems is crucial. The reasons vary from the cost of intervention, notably in terms of the machine downtime, such as the high-energy accelerator environment, or interventions being impossible, such as space applications. Both of the fields mentioned above deal with harsh radiation environments where radiation hardness assurance is an absolute necessity.

As a consequence of the increased sensitivity, the devices also used in these applications are becoming more sensitive to radiation effects from particles not traditionally considered in standard radiation hardness assurance guidelines. The increased sensitivity also implies lower critical charges, which in turn means that particles with lower linear energy transfer (LET) values such as low-energy protons and electrons can contribute to the overall error rates.

2.1 Radiation Interaction with Matter

The core of this thesis is investigating the interaction mechanisms of electrons with matter, which result in a high enough energy deposition in the sensitive parts of electronics to cause measurable radiation-induced single-event effects. The interaction of radiation with matter allows us to study the underlying mechanisms. In general, for electron interaction with matter, we can divide nuclear radiation into two classes as shown in Table 2.1 [18].

The path of a charged particle passing through matter is dependent on the mass of the interacting particles. Due to the small mass of electrons compared to the heavier charged particles, the paths of electrons are altered continuously when passing through matter

Charged Particles	Non-charged Particles
Protons	Neutrons
Heavy ions	γ rays
Electrons	

Table 2.1: Particle classes for interaction with matter [18]

without the electron losing much energy. However, nuclear reactions between electrons and nucleus result in substantial energy losses and therefore high local energy deposition and can abruptly change the direction the particle is traveling. Besides, electron energy can be lost through a radiative process called Bremsstrahlung as well as Coulombic interactions (Rutherford scattering) [18, 19].

2.1.1 Electrons

Unlike heavy charged particles, the passage of electrons through material is usually described by large deviations in the tracks. These deviations result because the electron mass is much lower and its mass is now the same as the orbital electrons of the atoms, which in turn means that the deflections angles are much larger and the electrons themselves can lose a large amount of energy with each interaction. Another difference that electrons can lose their energy through a combination of radiative processes and Coulomb interactions [18, 19].

For fast electrons in material, the energy loss can be described as:

$$-\left(\frac{dE}{dx}\right)_{electron} = S_{electronic} + S_{radiative} \tag{2.1}$$

Which means that the total stopping power is a combination of collisional or electronic and radiative losses. Whereas the radiative process is specific to electrons, the electronic stopping power also applies to interactions between electrons and other charged particles [18, 19]. The electronic stopping power for electrons is written as:

$$\begin{aligned} S_{electronic} = -\left(\frac{dE}{dx}\right)_{electronic} = \frac{2\pi Z e^4 \rho_N}{m_e \nu^2}\Bigg[\ln\left(\frac{m_e \nu^2 E}{2I^2(1-\beta^2)}\right) - \\ \ln 2\left(2\sqrt{1-\beta^2} - 1 + \beta^2\right) + (1-\beta^2) + \frac{1}{8}\left(1-\sqrt{1-\beta^2}\right)^2\Bigg] \end{aligned} \tag{2.2}$$

where $\beta = \nu/c$, ν and e are the velocity and charge of the primary particle, m_e is the electron rest mass, Z and A are the atomic mass and atomic number of the absorber material and e is the electronic charge.

The expression for radiative stopping process is:

$$S_{radiative} = -\left(\frac{dE}{dx}\right)_{radiative} = \frac{(Z+1)Ze^4\rho_N E}{137m_e^2c^4}\left[3\ln\left(\frac{2E}{m_ec^2}\right) - \frac{4}{3}\right] \tag{2.3}$$

The ratio of the energy losses depends on the atomic number of the material Z and the energy of the electron in units of MeV [18, 19]. The radiative energy loss is most important for electrons with high energies and shielding materials with a high atomic number [18].

$$\frac{S_{radiative}}{S_{electronic}} \approx \frac{ZE}{800\,\text{MeV}} \tag{2.4}$$

As shown in Fig. 2.1, the total electron stopping power is dominated by collisional losses at lower energies and radiative stopping power at higher electron energies, i.e. $> 50\,\text{MeV}$ in silicon.

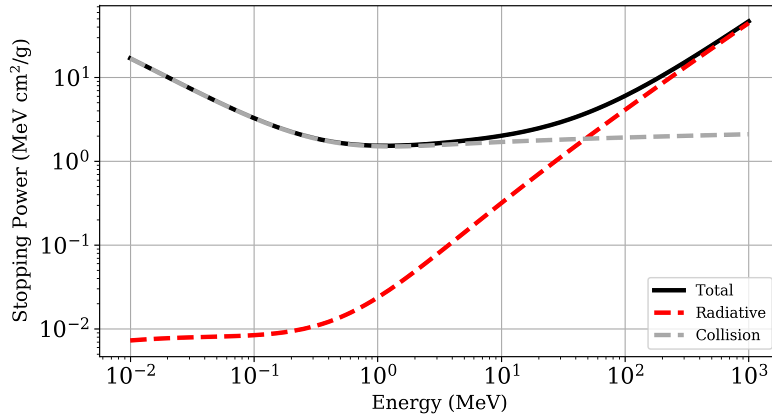

Figure 2.1: Total, Radiative and Collision Stopping power for electrons in Silicon from the ESTAR database [20]

2.2 Rutherford or Coulomb Scattering

Rutherford or Coulomb scattering refers to a type of elastic scattering where the electron feels the Coulomb or electric potential of a positively charged nucleus and is therefore deflected from its path [18]. The Coulomb force acting between a projectile of mass m, charge Z_1, and a target nucleus with charge Z_2 is given as:

$$F_{Coul} = \frac{Z_1 Z_2 e^2}{r^2} \tag{2.5}$$

where r is the distance between the projectile and target nuclei [18].

2.3 Electro- and Photo-Nuclear Interactions

Photo-nuclear reactions are a subset of nuclear reactions in which the incident projectile is a photon, and the emitted particles are either charged particles or neutrons. Examples of such reactions are reactions like (γ, p), (γ, n), (γ, α), and so forth [18].

Electro-nuclear reactions are very connected with Photo-nuclear reactions. They are sometimes called "Photo-nuclear" because the one-photon exchange mechanism dominates the reaction [21]. Therefore, the electromagnetic interaction of fast charged particles with nuclei can be reduced to the effective interaction of equivalent flux of photons distributed with some density n(ω) on a frequency (energy) spectrum [22].

2.4 Radiation Effects in Electronics

All radiation-induced damage in electronics is related to the process of energy deposition [23]. The radiation effects in electronics can in broad terms be divided into three:

- Total ionizing dose effects (TID)
- Single-Event Effects (SEE)
- Displacement Damage (DD)

In broad terms, the total ionizing dose effects (TID) deal with an accumulation of dose deposited by particles over period which leads to a degradation of the device's performance. The quantity which directly relates to the deterioration is absorbed dose which has the unit of Gy; defined as 1 J of energy absorbed by 1 kg of matter. The typical effects on devices are caused by the energy deposited in a semiconductor or insulating layers frees charge carriers. Similar to TID effects, displacement damage (DD) occurs as a cumulative effect. Here, the cumulative damage to the silicon lattice itself causes the degradation of the device properties [23].

Unlike the previously mentioned effects, single-event effects (SEE) are caused by a single charged particle depositing enough energy in the sensitive region of a device to cause a perturbation. Single-event effects can further be divided into hard and soft failure mechanisms. Soft failure mechanisms are either self-correcting or can be eliminated by a restart of the system, whereas hard failures can result in permanent damage or destruction of the device if not contained.

2.5 Electron-Induced SEE

Electron-induced single-event effects (SEE) are a relatively new topic, which has become more relevant as of late due to the decreasing critical charges of devices and space missions

planned to planetary systems with very harsh electron radiation spectra. There are several missions planned to the Jovian system, such as the JUpiter ICy moon Explorer (JUICE) mission by the European Space Agency (ESA). The Jovian system is especially interesting in this regard due to the high fluxes and energies of the trapped electrons in the radiation belts [10, 11].

Previously, electron-induced SEE have been studied mostly in highly-integrated technologies. Due to the lower critical charge, these devices have been theorized to be more susceptible to electron-induced SEE. One of the first studies like this was using up to 40 keV x-ray photoelectrons in 28 nm and 45 nm CMOS Static Random Access Memories (SRAM) [17]. However, this study biased the devices to up to 90 % and below of the nominal supply voltage, which significantly increases their susceptibility to single-event effects, as introduced in [24] and [25]. The results suggested that the SEE cross-section was exponentially related to the bias voltage applied to the SRAM cells during irradiation. The proposed cause of these SEE was theorized to be single energetic electron scattering events within the SRAM cells.

Further radiation tests performed on a 45 nm SRAM of an FPGA with electron energies up to 20 MeV confirm that electrons are capable of inducing SEUs [26]. However, this study concludes that the primary source of upsets in the SRAM is the ionizing energy loss by the primary and secondary electrons, generated through an electromagnetic shower, the cumulative charge of one or more electrons hitting the sensitive volume in a critical period. This cumulative charge is then shown to cause the upset in the device.

Another study looking at electron-induced upsets in 28 nm and 45 nm bulk SRAM used a mono-energetic electron beam from 40 keV to 100 keV [27]. The source of the SEU in this study was shown to be δ-rays produced by the primary electrons. Single-event upsets (SEU) observed in this study were attributed to energetic electrons generated by the incident δ-rays [27]. The study also highlighted that in a geostationary orbit (GEO), the upsets rates depend exponentially on the critical charge of the devices. For lower critical charges the SEU rate induced by electrons could be comparable or even more significant than that induced by protons [27].

A study using higher energy electrons at 20 MeV attributed the resulting SEU to rare-indirect ionization event - nuclear events [16]. The irradiated devices were 28 nm and 45 nm bulk SRAM in Field Programmable Gate Arrays (FPGA). This study was the first to show also through simulation how these rare nuclear events could be the source of the upsets. Depending on the device and irradiated cell, the upset cross section was between 1×10^{-17} and $1 \times 10^{-18}\,\mathrm{cm}^2/\mathrm{bit}$.

In addition to the inelastic electron-nuclei interactions, another source for the electron-induced upsets was proposed in [28]. The parallel process of Coulombic electron-nuclei interactions could be responsible for upsets caused by higher energy electrons. The

Coulombic interaction has an energy threshold similar to that of electronuclear events; therefore the work concluded that either effect could contribute to the upsets and that further studies were needed.

Further studies indicating electronuclear interactions as the source for electron-induced single-event upsets have been published. The experimental results were obtained using electron energies between 9 MeV to 52 MeV in 28 nm and 45 nm bulk SRAM-based FPGA [29].

In addition to single-event upsets, electrons were also capable of inducing multi-cell upsets (MCU), as shown in [30]. The study investigated 28 nm and 45 nm CMOS SRAM-based FPGAs, with beam energies from 9 MeV to 52 MeV. The significant finding in this paper was that with the scaling of technology the prevalence of MCUs increased.

Another study discussing the exact mechanism and the role of the Coulombic interaction in the electron-induced upset rate is [31]. Measurements were performed on the SRAM-based Xilinx 6 FPGA at 1 MeV to 6 MeV. The study concludes that elastic scattering, more specifically Rutherford scattering, is the dominant process above $\sim$ 10 MeV. Below $\sim$ 10 MeV, the inelastic scattering of electrons on other electrons is shown to be most significant. However, the study considers devices with low critical charges, below 0.6 fC and can therefore not explain the SEU in devices studied in this thesis with a critical charge of $\sim$ 10 fC since the processes described do not deposit enough energy. The discussion of the dominating mechanisms for these devices is discussed in chapter 5.

3 Simulation Tools

The radiation interaction with matter, which is the fundamental building block of the analysis of radiation effects in electronics, is a complex problem. The underlying complexity lies in the degrees of freedom this problem has. Due to the complexity, simulation packages using statistical methods, such as Monte Carlo, combined with well-defined microscopic interaction models have to be used. Below is a general introduction to the fundamental statistical method used by the various simulation toolkits - the Monte Carlo Method, and a short description of the tools used for the simulations presented in this thesis.

3.1 Monte Carlo Method

Monte Carlo is a form of numerical integration, in which finite summations are used to estimate definite integrals. As described in [32], the Monte Carlo method can be successfully applied to multidimensional integrals, where it often outperforms other numerical methods. Monte Carlo enables simplifying complex analytical problems through simulation [32]. Monte Carlo tools are extensively used in particle physics to simulate the particle interaction with matter. Some of the standard tools that will be described in this chapter and were used in the scope of this work are FLUKA [33, 34], Spenvis/GRAS [35, 36], which is based on Geant4 [37, 38] and CREME MC [39], which is based on the Geant4 [40−42].

The problems the Monte Carlo Method tries to predict in high energy physics are often random by nature, such as the exact time a radionuclide will disintegrate. Each such random variable has associated with it a probability density function (PDF), a cumulative distribution function, a population mean, and other measures of the variable's randomness [32]. The Monte Carlo method is based on two mathematical theorems: the law of large numbers and the central limit theorem, both of which are described in more detail in many sources, for example [32].

3.2 FLUKA

FLUKA [33, 34] is a multipurpose transport and Monte Carlo tool for calculations of particle transportation and interactions with matter. The FLUKA code is built on modern physical models, microscopic models are used whenever possible and available. The consistency between reaction steps is ensured and the results are checked against experimental data. Therefore, final predictions have a minimal amount of free parameters for any combination of particles and matter. FLUKA is therefore especially suited for complex cases where many materials and beams that are not readily available are present [43].

In general, no Fortran programming is needed, and FLUKA is used by specifying features to be activated or disabled using input files. The main parameters that have to be defined by the user are the geometry, the beam specifications, and special physics parameters. FLUKA can simulate the interaction and propagation of about 60 different particles in matter. Also, time evolution and tracking of emitted radiation from unstable residual nuclei can be performed online.

Another essential feature of FLUKA is its dual capability to be used in a biased mode as well as an entirely analog code. The biasing element becomes especially important when considering rare interactions, such as the interaction between electrons and the nuclei within the target material.

FLUKA handles complex geometries well by implementing an extended version of the Combinatorial Geometry. Besides, powerful visualization and geometry editing tools are available through the graphical user interface called Flair [44]. An example of a geometry of a memory cell can be seen in Fig. 3.1.

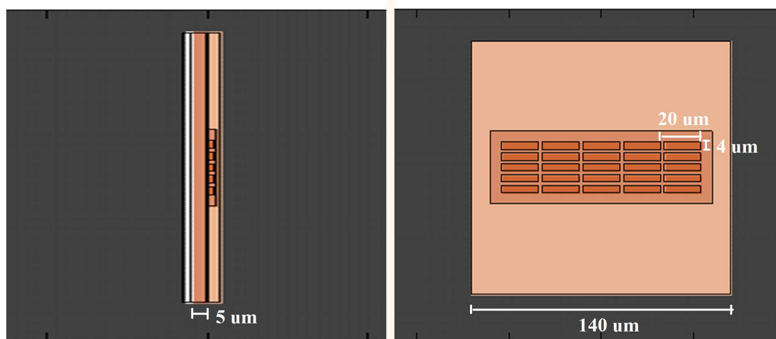

Figure 3.1: The geometry of a SEL-sensitive region used in a FLUKA energy deposition simulation [3]

There are various physics options available within FLUKA. For rare interactions, such as the photo- and electro-nuclear interactions biasing has to be used. The biasing applied in this work is the LAM-BIAS card to allow the biasing of inelastic interactions of electrons

and photons. The activation of the photo- and electro-nuclear options is shown in Fig. 3.2, this option is only available in the currently in the development version of FLUKA.

Figure 3.2: The activation of electro- and photo-nuclear options in FLUKA, available only in the developer version

Another important aspect of the simulations is the CPU-time or how much time is needed to simulate one particle undergoing all of the interactions. To enhance the CPU-time, especially for processes with low cross-sections such as electro-and photo-nuclear interactions, biasing needs to be used. The biasing used in the simulations performed in this work and its implications are discussed in more detail in chapter 5.

3.3 Spenvis/GRAS

SPENVIS or SPace ENVironment Information System is ESAs on-line web interface which is used for radiation effects modeling. SPENVIS takes into account cosmic rays, natural radiation belts, solar energetic particles, plasmas, gases, and "micro-particles" [35]. SPENVIS is made up of a collection of Geant4 tools, which is a toolkit for the Monte Carlo simulation of the passage of particles through matter. Its application areas include high-energy physics and nuclear experiments, medical, accelerator and space physics studies [37, 38].

The tool mainly used in this work is GRAS, which is a Geant4-based tool that provides a general space radiation analysis for 3D geometry models [36]. More specifically, GRAS allows the definition of a multi-volume 3D geometry and incident particle source. Then, using the Geant4 toolkit, it is possible to simulate radiation transport through the geometry, including electromagnetic and nuclear interactions [35]. Users can specify the incident particle, its energy spectrum and angular distribution using the “source particles” template that is common for all Geant4 tools in SPENVIS.

There are two execution modes available for the SPENVIS GRAS implementation: Mulassis or GDML. Mulassis allows the definition of a multi-layered, one-dimensional shield and incident particle source, and using the Geant4 toolkit allows the simulation of radiation transport through the geometry, treating electromagnetic and nuclear interactions.

The source geometry in GRAS can be either a point, a disk, or a sphere. In this work, a point source was used [35].

The analysis mode used in this work was fluence. This analysis mode allows scoring of the total fluence of desired particles through a surface, which is then normalised to fluence

```
/gras/geometry/type gemat

/geometry/layer/xysize                  5.0000 um
#
# Define the layers
#
/geometry/layer/delete 0
/geometry/layer/add  0 Silicon     12   3.000E+00 um
/geometry/layer/add  1 Aluminium   5    1.000E+00 um
/geometry/layer/add  2 Silicon     12   2.000E+00 um
/geometry/layer/add  3 Aluminium   5    5.000E-01 um
/geometry/layer/add  4 Sio2        12   5.000E-01 um
/geometry/layer/add  5 Aluminium   5    5.000E-01 um
/geometry/layer/add  6 Silicon     4    5.000E-01 um
/geometry/layer/add  7 Silicon     4    5.000E-01 um
/geometry/layer/list
#
# Define the depletion volumes
#
/geometry/SV/delete    0
/geometry/SV/add/box   7   0.00   0.00   1.50   1.50  0.00 G4_Si  10 um
/geometry/SV/list
```

Figure 3.3: An example of a GEMAT geometry of a Back-end-of-line of an electronic component

```
/gras/geometry/type mulassis

/geometry/layer/delete 0

/geometry/material/add Tantalum Ta 16.65
/geometry/material/add Lead Pb 11.34

/geometry/layer/shape sphere
/geometry/layer/add 0 Lead      1 1 mm
/geometry/layer/add 1 Aluminium 1 1 mm
/geometry/layer/add 2 Aluminium 1 6 mm
/geometry/layer/add 3 Aluminium 1 2 mm
/geometry/layer/add 4 Vacuum    1 0.01 mm

/geometry/layer/list
```

Figure 3.4: An example of a Mulassis geometry of a sphere

per source particle. The secondary radiation environment spectra of the Jovian trapped electron and proton spectra were transported through aluminium and tantalum shielding. The resulting secondary particle spectra were used to estimate the upset rates in the Jovian environment. The details of the simulation and the results can be found in [1] and are described in chapter 5.

3.4 CRÉME MC

The CRÉME website hosts the CRÉME MC, which is a physics-based Monte Carlo tool for estimation of SEE rates [39]. CRÉME MC is implementing MRED, which is a Geant4 application developed at Vanderbilt [41]. CRÉME MC allows for the specification and creation of geometries, the specification of radiation environments and the calculation of SEE rates [39]. CREME MC is conceived as an improvement of CREME96 [40−42] tool, specifically it considers nuclear reactions, energy loss variation, stopping and straggling of particles [39]. What is relevant for this work is that the nuclear effects and the respective biasing are available through this tool, which provides a convenient cross-check of the energy deposition by biased electro- and photo-nuclear interactions in other Monte Carlo tools, such as FLUKA, as shown in chapter 5.

4 Radiation Environments and Tested Devices

A vital part of radiation effects analysis is the understanding of the radiation environment for which the investigation is being performed. The environments described in this section can be divided according to their damaging effects on the electronics as:

- Electron-induced effects
  - Jovian environment, which contains large fluxes of high-energy electrons in the trapped radiation belts. Also, the secondary particle fluxes generated by the trapped particles passing through spacecraft shielding can be an essential contribution to the overall upset rates;
  - The high-energy electron facility VESPER is described as it was used for the bulk of the experimental work;
  - The electron linac at RADEF was used for intermediate-energy electron testing.
- Low-energy protons and heavy ions
  - RADEF facility was used for both intermediate and low-energy proton testing described in this work, as well as for heavy ions;
  - CHARM facility was used as a representative environment of the high-energy accelerator at CERN.

The environments are described in terms of the particle types and energies and also in terms of the various calibration steps taken to use them for radiation effects analysis. Several simulations have been run to estimate the secondary particle environment using both FLUKA and SPENVIS/GRAS.

4.1 Jovian Radiation Environment

The space environment is a challenge for all spacecraft reliability; even more so for the JUICE mission to explore Jupiter and its icy moons, planned to be launched by 2022 by ESA, presents an extraordinarily complicated problem. The radiation environment surrounding the planet is extremely harsh. To correctly assess the possible radiation

induced-effects on electronics, the environment has to be carefully studied. The exact specification of the mission environment provides a detailed description of the environment [11] [10]. The main difference between the two versions is the updated Jovian trapped proton model. The specification is based on the ECSS Space Environment Standard [45].

The main components of the radiation environment in the Jovian radiation environment are:

- The radiation belts - trapped radiation
- Solar particle events
- Galactic Cosmic Rays
- Secondary radiation (generated through the radiation interaction with the spacecraft shielding)

The trapped electrons will be the main contribution to the overall dose of the mission [10]. The total duration of the mission and the mission phases can be seen in Table 4.1. The radiation environment depends strongly on the phase of the mission.

Phase	**Description**	**Duration (days)**
Phase 0	Interplanetary transfer	2711
Phase 1	Transfer to Europa	458
Phase 2	Europa flybys	38
Phase 3	Jupiter high latitude phase with Callisto	248
Phase 4	Transfer to Ganymede	311
Phase 5a	Ganymede orbit insertion	152
Phase 5b	Ganymede 500 km altitude circular orbit	103
Phase 5c	Ganymede 200 km altitude circular orbit	30

Table 4.1: Description of JUICE mission phases

4.1.1 Radiation Belts

The primary particles of concern for radiation effects in the trapped radiation belts are electrons and protons. Because of the strength of the magnetic field of Jupiter, the radiation belts extend far into space, even beyond the major moons [10]. The differential flux of particles can be seen in Fig. 4.1.

The trapped radiation in the Jovian system is much harsher than in the earth radiation belts [11]. In Fig. 4.1 one can see that the differential trapped particle spectra is both much harsher in terms of energies that the particles reach but also in terms of the fluxes. The high energy electrons, with energies higher than about 5 MeV (maximum energy for trapped electrons in the GEO orbit) are the main focus of [1] and [2]. The motivation is

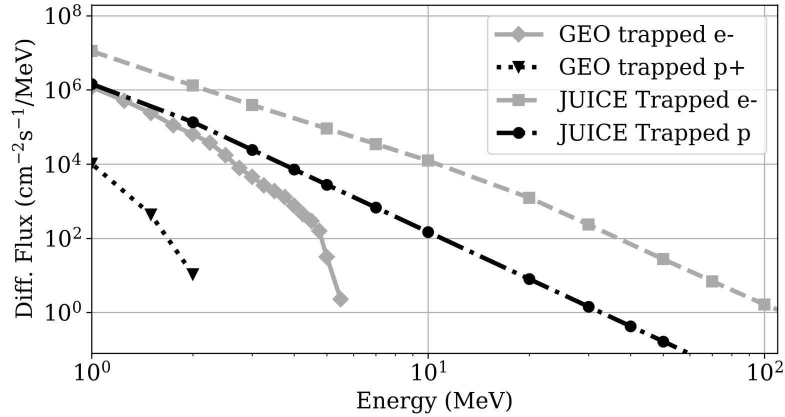

Figure 4.1: The average differential spectra of the trapped radiation in the Jovian system for phase 5a of the JUICE mission [10], which has one the most energetic trapped particle environments during the mission, compared to shielded electron spectra on geostationary (GEO) orbit from SPENVIS [35]

the relatively limited amount of work already existing for high energy electron induced SEE and the unknown mechanisms causing errors in the electronics in the spacecraft.

4.1.2 Secondary Radiation

The secondary radiation is generated by energetic radiation passing through the shielding of the spacecraft [10]. Several simulations have been presented in [1] describing the spectra of the radiation produced by the trapped electrons and protons and solar protons passing through the spacecraft shielding. The simulations were performed using GRAS [36], which is a Geant4 [37, 38] based radiation analysis package [1]. The results of this study are discussed in more detail in Section 4.1.3.

In addition to the generic shielding value provided in [1], a more detailed analysis of the material and the thickness of the shielding was performed in [2]. In this work, a more detailed shielding description existed for the JUICE spacecraft and the secondary radiation created by the different shielding materials and thicknesses could be estimated.

4.1.3 Secondary Radiation Environment Simulation

As a first approach, a worst-case estimate for a spacecraft shielding was created [1]. To be able to estimate the SEE cross-section of devices in the Jovian environment, a simulation was performed using GRAS. The geometry is a simple sphere with 20 mm aluminium and tantalum shielding in equal parts by weight. Since the density of tantalum is 16.65 g/cm^2 and the density of aluminium is 2.7 g/cm^2, an equal weight of each material results in 2.8 mm of tantalum and 17.2 mm of aluminium.

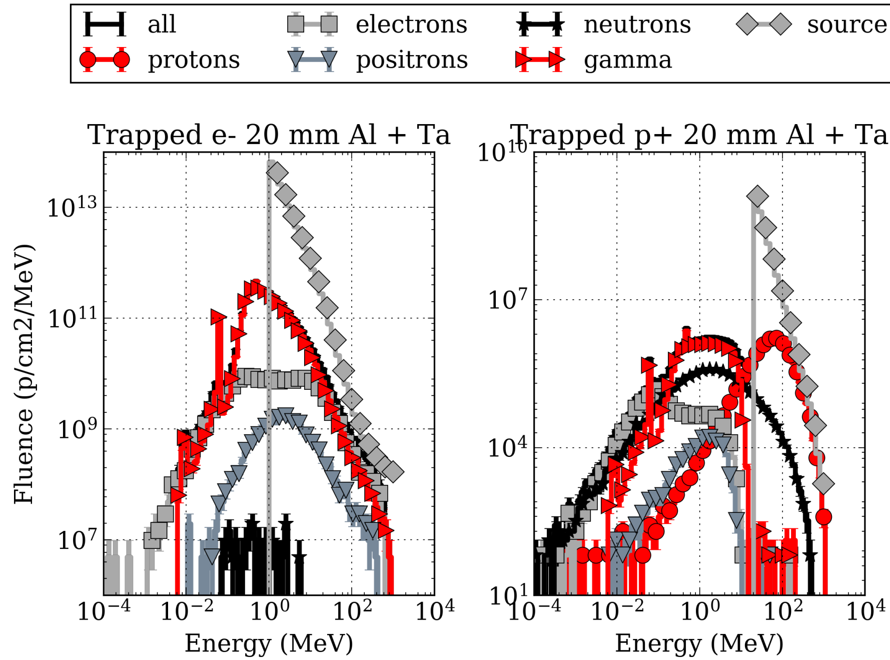

Figure 4.2: JUICE mission scored differential fluence of particles, spectra transported through 20 mm aluminium and tantalum shielding

The differential spectra of the trapped proton and electron fluxes, described in Section 4.1.1, were transported through the shielding. The resulting secondary radiation spectra can be seen in Fig. 4.2. What can be noted is the high fluence and high energy of the secondary gamma radiation created by the trapped electrons passing through the shielding materials. This gamma spectrum is generated by the Bremsstrahlung process described in Section 2.1.1. The implications and effect on the final SEE rate for the components were described in [1] and described in more detail in chapter 5.

As a first estimate of the impact the secondaries could have on the overall SEE rate, the integrated fluence of secondaries > 10 MeV generated are found. This energy range is generally regarded as relevant for SEE generation in embedded devices. As can be seen in Table 4.2, the trapped electrons create large amounts of photons. Also, the high-energy electron fluence remains high even after passing the shielding. Trapped protons generate a large number of neutrons, and the high-energy trapped proton fluence is attenuated more compared to the trapped electrons. Trapped protons generate also some photons; however, the fluence is six orders of magnitude lower than for trapped electrons.

Secondaries - Trapped Electrons	
Particle	**Int. Fluence > 10 MeV (p/cm^2)**
electrons	4.2×10^{10}
protons	0
neutrons	0
gamma	6.7×10^{10}
Secondaries - Trapped Protons	
Particle	**Int. Fluence > 10 MeV (p/cm^2)**
electrons	5.3×10^{2}
protons	1.7×10^{7}
neutrons	1.1×10^{6}
gamma	4.1×10^{4}

Table 4.2: The integrated flux over the complete JUICE mission of secondaries created by propagating the trapped particle spectra through 20 mm Aluminium + Tantalum shielding. The electron and positron contribution is summed under the electron contribution.

4.2 VESPER Test Bench

The VESPER test bench is a part of the CLEAR Test Facility CTF3 at CERN [1]. The primary focus for CLEAR is general accelerator research and development and component studies for existing and possible future machines at CERN [46]. The VESPER test bench is located at the CLEX experimental area, the layout and the location of which can be seen in Fig. 4.3.

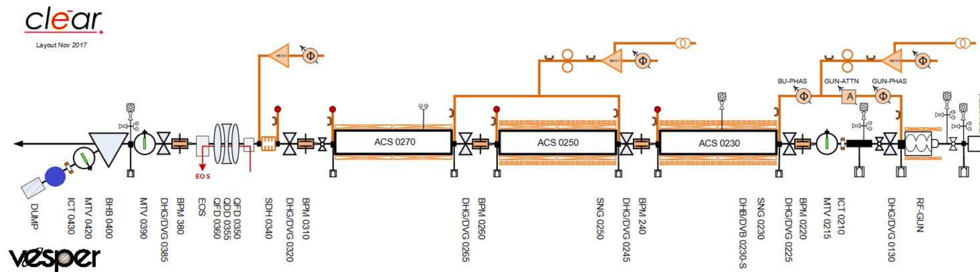

Figure 4.3: The location of the VESPER test bench (marked with a blue circle) at the CLEX hall, which is a part of the CLEAR facility [46]

The VESPER test bench can be used in several configurations, the most relevant for testing electronics is the beam mode in which the laser is not used to excite the electron beam, and only the leakage of the gun is accelerated - the dark current beam. The second type of beam is the laser-driven beam where the electrons are also excited with a laser, resulting in much higher fluxes. The main parameters of the dark current beam that can be chosen to change flux are the following:

The beam charge - can be varied from about 1 pC to 15 pC. The beam charge is actively monitored using the fast beam current monitor (FBCM); it can be seen in the foreground in Fig. 4.4. By using the conversion from charge to the number of electrons by using the charge of 1 electron being 1.6×10^{-19} C and the beam size, the flux of the beam can be estimated. A gold activation experiment was performed to calibrate the beam intensity, the results are described in detail in section 4.2.1.1.

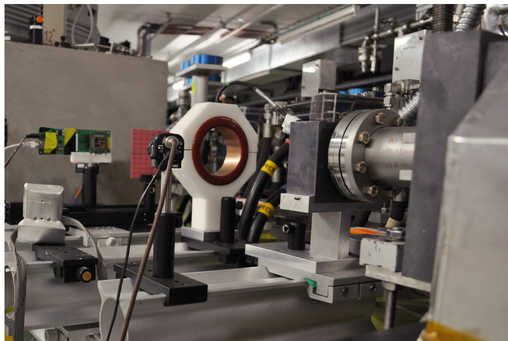

Figure 4.4: left) The Vesper test bench with the FBCT in the foreground and a device being tested in the background ©Ranveig Strøm, CERN

The beam energy - depending on how many accelerating structures are used in the beamline the energy can be varied from 60 MeV to 220 MeV. The beam energy is monitored at the test position with a beam TV (BTV). The BTV is a scintillating screen; it can be seen as the pink screen in the center in Fig. 4.4, through calibration, the beam energy can be estimated.

The beam size - is estimated by using the BTV screen. The BTV can be seen in Fig. 4.4. The BTV is composed of a scintillating screen made of chromox, and a camera, which is recording the emitted light produced by the scintillating reaction of the beam hitting the screen. A script is used to correlate the emitted light to the beam shape. The analysis of the BTV feed gives an accurate beam size and shape in both x and y position as well as the center of the beam spot.

The beam structure - The beam consists of pulses delivered at a frequency ranging from 0.8 Hz to 5 Hz. The beam consists of bunches which are delivered at a frequency of 3 GHz. The pulse duration is a free parameter and can be chosen from 0 to 5 µs, therefore the longest pulse of 5 µs consists of 15000 pulses, which would contain about 4170 electrons. The pulse structure can be seen in Fig. 4.5 [47].

4.2.1 Calibration of the Facility

The beam at the CTF3 facility, where the VESPER test bench is located, was not designed for radiation testing. Therefore, the dark current beam mode had to be used. The beam spot size was blown up using the magnets upstream of the test position. In addition, a

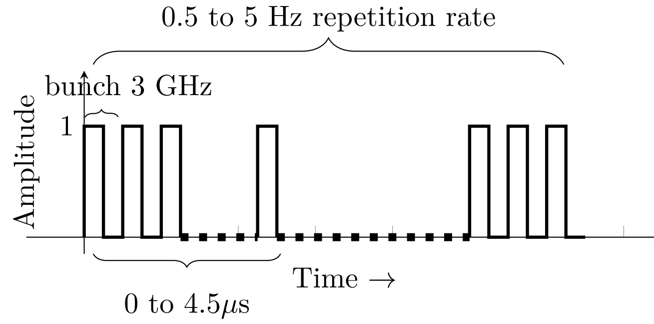

Figure 4.5: The structure of the pulsed electron beam at VESPER

screen composed of chromium oxide was used to scatter the beam further. The beam had to be calibrated in terms of the beam homogeneity, size and the beam flux. The calibration of the beam and the proposed modification of the VESPER test stand were performed as part of this thesis work. Several different calibration methods were used and are detailed below.

4.2.1.1 Gold Foil Activation Measurements

Experimental Setup Initially, there was no dedicated dosimetry system at the test position. Complementary measurements had to be performed to validate that the absolute intensity of the beam agrees with the beam charge measurements performed using the fast beam current transformer (FBCT) at the test position. The FBCT gives the beam current measurement in pC. The gold activation experiment provides, therefore, an independent absolute intensity measurement, with which to verify the calibration of the FBCT.

Gold activation measurements have been performed previously for a similar purpose at Pohang with a 2.5 GeV electron beam, and good agreement was seen between simulation and experiment [48]. The gold foil activation was simulated using the Monte Carlo code FLUKA [33, 49]. The reaction that was measured is the reaction ^{197}Au(γ, n) ^{196}Au [50]. This reaction is well benchmarked in the FLUKA code; good agreement is shown between the experimental and simulated cross sections. After irradiation of the sample, the activity of the dominant γ peak at 355 keV is measured using a germanium particle detector, and the total activity of the sample is derived.

For the experiment copper blocks with dimensions of 5 cm × 5 cm × 0.5 cm were interleaved with 1 mm thick gold foils, which can be seen in Fig. 4.6. The copper blocks generate additional photons through bremsstrahlung, which enhance the rate of activation of the gold leaves. This effect is analogous to the generation of secondary photons as the trapped charged particles in the Jovian system pass through the shielding materials, described in section 4.1.2, the implications of which are described in more detail in section 4.1.3. The characteristics of each irradiation run can be seen in Table 4.3, the sample was

irradiated, and then gamma spectroscopy was performed following the irradiation. The results reported from the activity measurements are the derived activities immediately following the irradiation.

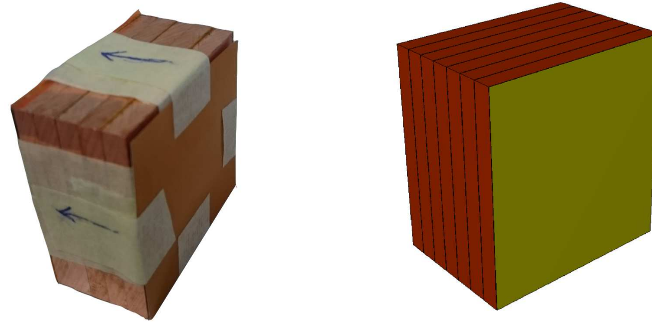

Figure 4.6: left) 5 cm × 5 cm × 0.5 cm copper blocks interleaved with gold foils. right) geometry model created in FLUKA.

Activation Simulation The FLUKA simulation was set up so that each copper block interleaved with gold foils, the first gold foil being at position z=0. The geometry of the FLUKA model can be seen in Fig. 4.6. The beam energy, charge, spot size, and center position were chosen for each simulation run to reflect the beam size and beam current measured by the BTV and FBCT respectively. The beam conditions measured during the irradiations can be seen in Table 4.3 [51].

Duration (h)	Charge /pulse (pC)	x0 (cm)	y0 (cm)	FWHM x (cm)	FWHM y (cm)	Energy center (MeV)
17.2	32.1	0.21	0.18	4.34	3.99	200
14.0	13.21	0.16	0.14	2.50	2.50	212

Table 4.3: Beam conditions measured with the BTV and the FBCT

After the completion of the simulations, the experimental results obtained through the spectroscopy were compared to the results obtained from FLUKA to verify the calibration of the FBCT. The results of the measurements and the simulations can be seen in Table 4.4. The comparison between simulation and experimental measurements shows an excellent agreement, with most of the result differing less than 10%. Therefore, the calibration of the FBCT could be trusted as the absolute measure of the beam intensity.

Beam Shape Validation A comparison between the readout of the BTV and radio-sensitive films was made to validate the beam shape. The films used are Gafchromic

	Run A Au-196					Run B Au-196				
	FLUKA		Meas.		FLUKA/ Meas	FLUKA		Meas.		FLUKA/ Meas
Foil	Data (Bq)	Err (Bq)	Data (Bq)	Err (Bq)		Data (Bq)	Err (Bq)	Data (Bq)	Err (Bq)	
1	126.2	8.35	170	15.3	0.74	180	20	186	4	0.97
2	1076	22.11	1200	108	0.90	1750	76	1720	328	1.02
3	1449	25.97	1600	144	0.91	2347	80	2380	617	0.99
4	1717	31.20	2000	180	0.86	2984	89	2660	771	1.12
5	1825	29.75	2000	180	0.91	-	-	-	-	-

Table 4.4: Run 3 and 14 - Comparisons of the FLUKA simulations and experimental measurements

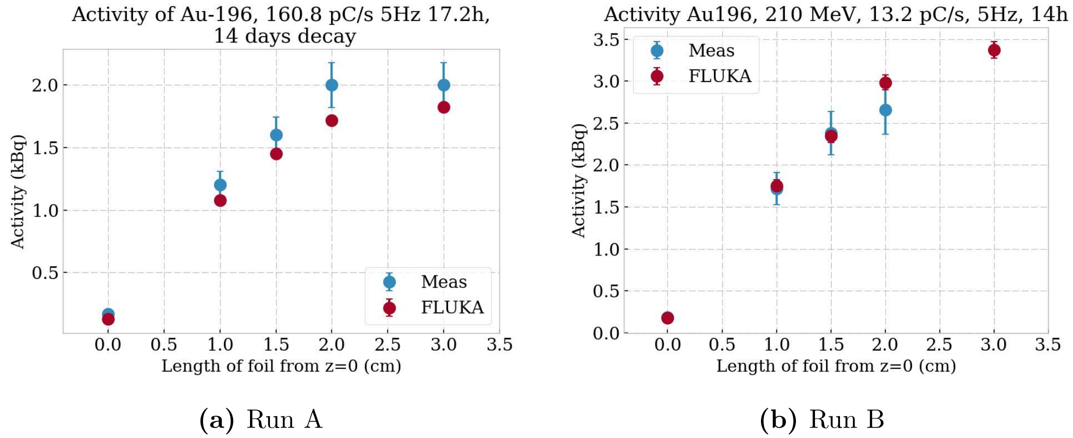

(a) Run A **(b)** Run B

Figure 4.7: Results of the gamma spectroscopy of the gold foils compared to the simulation performed in FLUKA

HD-V2 [52]. The films were placed directly on the DUT in the beam and later analyzed using a commercial image scanner. The images were analyzed, and the beam shape and relative intensity could be derived. Readouts from the Gafchromic film and the BTV can be directly compared to determine if the BTV, which is about 10 cm upstream of the DUT position. As a result, the readout and the beam shape at the DUT position were comparable. The readout from the BTV is in arbitrary units on the y-axis and in cm on the x-axis. The absolute position of the beam on the radio-sensitive film is relative to the side of the film. The X and Y positions on the plots seen in Fig. 4.8, describe then the center of the beam relative to the edge of the films and the σ is the standard deviation value of the Gaussian function fitted both cross-sections of the beam.

Also, in the scope of this thesis work, an absolute calibration for the HD-V2 has been performed at the RADEF facility in Jyväskylä, Finland, as described in section 4.2.2.

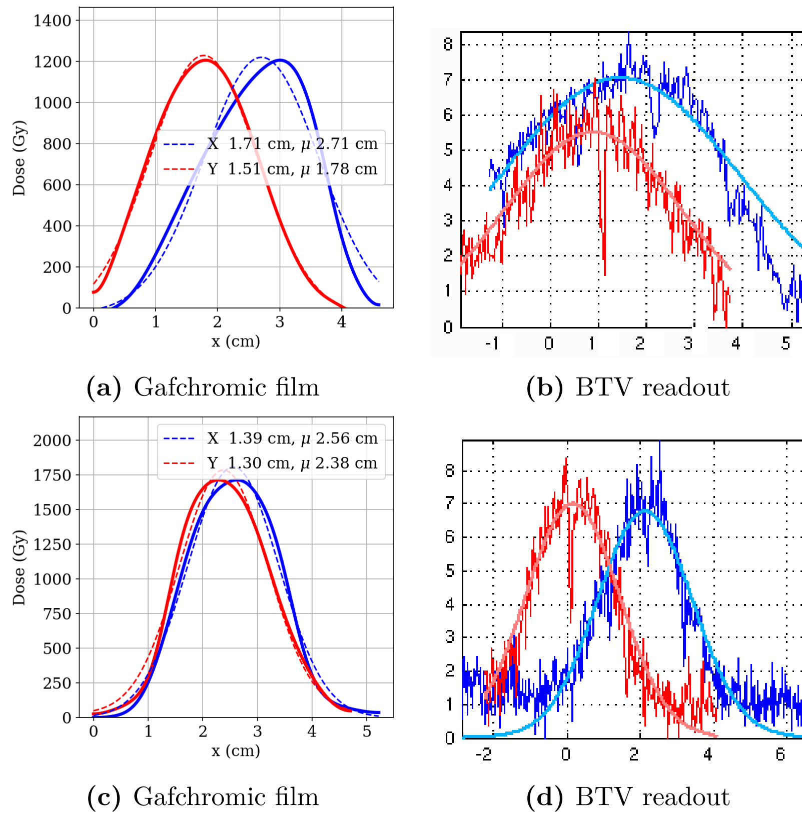

(a) Gafchromic film **(b)** BTV readout

(c) Gafchromic film **(d)** BTV readout

Figure 4.8: Radio-sensitive Film comparison with the BTV readout

4.2.2 Calibration of HD-V2 Radiosensitive Film

The radiosensitive film was calibrated in the electron clinac described in section 4.3.1 at the RADEF facility in Jyväskylä, Finland. The beam size used for the irradiations is 20 cm × 20 cm, the films were placed on a polyethylene slab on a table located in the cave [53].

As specified in the datasheet of the HD-V2 film the irradiation was performed in steps from 0 Gy to 1000 Gy, the summary of the irradiations and the readout of the films can be seen in Table 4.5. The films were scanned with a commercial photo scanner able to scan into raw 16 bit color depth.

The plot showing the results of the readout and the functions fitted to each color channel to retrieve the calibration curve per channel can be seen in Fig. . The calibration involves fitting the formula $dx(D) = a + b/(D - c)$, where D is the dose and a, b and c are constants to be determined. The final calibrated values of a, b and c for a 16-bit color depth are shown in Table 4.6.

sample	dose (Gy)	dose (rad)	R	G	B
0	0	0	52964	54530	15366
1	50	5000	32268	41736	18809
2	100	10000	24069	36971	22599
3	200	20000	14851	30183	21994
4	400	40000	10287	23419	20658
5	600	60000	7792	18908	18284
6	800	80000	9117	16863	17497
7	900	90000	8147	14986	16106
8	950	95000	7819	14598	15838
9	1000	100000	8330	14362	15774

Table 4.5: Experimental results

Channel	a	b	c
red	9.95×10^5	3.86×10^6	-9.33×10^1
green	1.59×10^8	-1.42×10^8	-3.26×10^2
blue	-2.28×10^8	2.66×10^8	-1.54×10^3

Table 4.6: HD-V2 calibration values assuming a 16-bit color profile

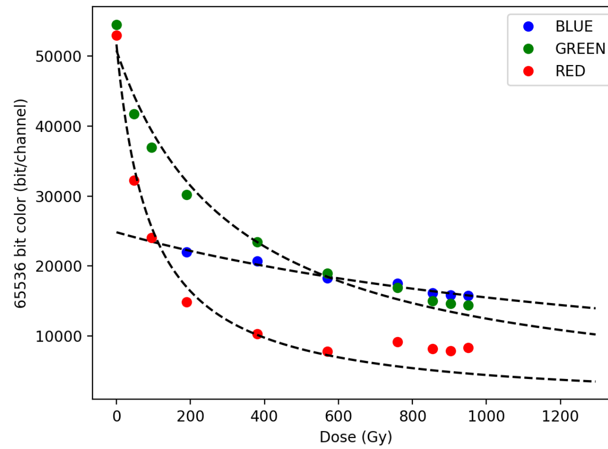

Figure 4.9: Results of the calibration of the HD-V2 film and the fits to each color channel

4.3 RADEF Facility

The RADiation Effects Facility (RADEF) is located in Jyväskylä, Finland and is a part of the Accelerator Laboratory (JYFL) at the University of Jyväskylä. The facility includes two beamlines in the same cave, dedicated to proton- and heavy-ion irradiation studies of semiconductor materials and devices, as well as a separate linear electron accelerator (medical linac) for electron and X-ray irradiation studies [2, 53–55].

The JYFL accelerator is a sector-focused K−130 cyclotron equipped with two ECR-ion sources for high-charge-state heavy ions and an H-minus ion source for intense protons [54, 56]. Its three external ion sources allow it to produce proton beams at energies ranging from about 500 keV to about 55 MeV, as well as heavy-ion beams; the general facility setup can be seen in Fig. 4.10.[53].

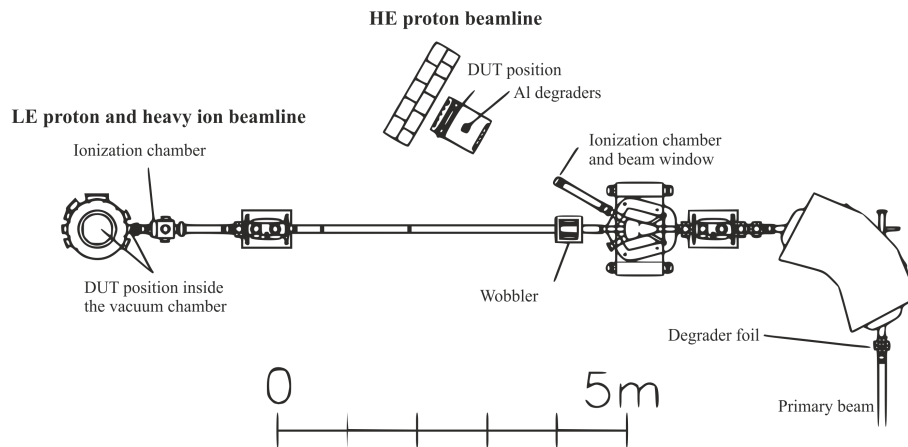

Figure 4.10: An overview of the beamlines at the RADEF facility with all of the beamlines and the main instrumentation visible. Figure from [57]

4.3.1 The Electron Clinac

The electron linac at the RADEF cave is a Varian 2100CD Clinac, which delivers both electron and X-ray beams. The electron energy can be chosen between 6 MeV and 20 MeV, the dose rates can be up to 1 krad(H_2O)/min. The dose rate is given as the maximum dose in water. At the maximum dose rate the beam consists of 5 µs pulses with a period of 5 ms [1]. The dose deposited by a single electron, and thus the dose relation to the electron flux, has been simulated using FLUKA [33], the simulation is described in more detail in section 4.3.2.

The main beam characteristics of the linac are period, 5.5 ms, pulse width 5 µs, frequency 180 Hz. For the experimental work at the linac a beam size of about 2 cm × 2 cm was used, the experimental results are discussed in detail in chapter 6. For the irradiations, the

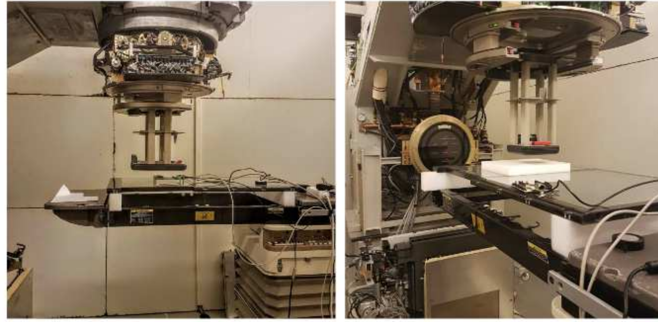

Figure 4.11: left) The Varian medical linac with the irradiation bench visible, center) Another view of the medical linac

components are placed on a table located in the cave and connected to a computer in the control room through a 20 m Ethernet cable [2]. The medical linac can be seen in Fig. 4.11.

4.3.2 Analysis of the Electron Beam at the RADEF Linac

The Varian 2100CD Clinac has two internal ionization chambers which monitor the dose delivered in real time. The linac at the RADEF cave has been previously characterized using two different detectors - PTW 30013 and PTW 34001 ionization chamber and a water phantom.

A FLUKA simulation was performed to estimate the upset rates caused by different particles generated by the primary beam interacting with the various elements in its path. The flux of the particles was characterized in terms of the energy spectra and the deposited dose. The main elements in the geometry were: the 4 mm beryllium beam exit window, the 2.5 mm aluminium diffusion foil and the two sets of 2.5 cm lead collimators. The primary purpose of the diffusion foil is spreading the pencil beam from the accelerator, while the collimators control the beam spot size[2].

The exact energy of the electron beam of the linac is 22.3 MeV [58]. A comparison between the experimental dose-depth curves obtained during the original calibration in water was performed to compare the FLUKA simulation response to the linac spectra. The maximum deviation between the curves was 15% up to a dose depth of 9 cm, the results are shown in Fig. 4.12. As a first estimate of the linac secondary particle spectra, the FLUKA simulation was therefore deemed suitable. The spectra of electrons, photons, and neutrons were scored to assess their contribution to the overall cross-section. The results highlighted the generation of a large amount of bremsstrahlung photons. Due to the large angles of the generated photons, the final beam at the DUT position was mostly comprised of electrons, and the photons contribution to the cross-section can, therefore, be deemed as negligible [2].

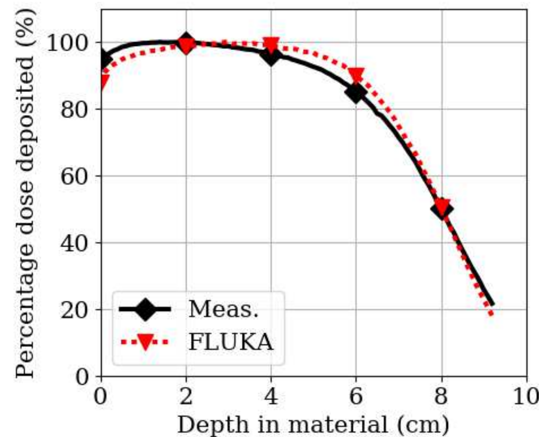

Figure 4.12: Relative comparison of the FLUKA simulation and experimental measurements at the electron linac of 20 MeV electrons in water. Values are normalized to the maximum deposited dose peak in water [2].

4.3.3 The Low Energy Proton Line

The low energy protons are generated by degrading the 6 MeV primary proton beam taken from JYFL K-130 cyclotron [56]. The beam energy is degraded using a movable wedge shaped aluminum degrader foil. The thickness of the foil is smoothly decreased from 500 µm down to 50 µm making the beam energy selection continuous [57].

Due to the magnetic selection, the energy distribution of the final beam is very narrow at the DUT (device under test) position, which is about 10 meters downstream from the magnet. About 25 keV full width at half maximum was measured for the final beam energy distribution with calibrated silicon detectors over the whole range of energies from 500 keV up to 5 MeV [57]. In addition to the energy selection, the use of dipole magnet ensures that the neutrons created in the interactions of the beam particles in the degrader foil cannot reach the DUT and possibly distort the results of the experiment [57].

The low-energy proton line can provide energies from about 500 keV to 6 MeV. The maximum flux is dependent on the energy, at 1.5 MeV this corresponds to about 5×10^7 p/cm^2/s. The components under test are attached to a movable backplate in a vacuum chamber [55, 57].

4.3.4 The Heavy Ion Line

The cyclotron can run "ion cocktails" which are mixtures of ions with near-identical charge-to-mass ratios [55]. The ions provided by the facility have linear energy transfer (LET) values in silicon of up to 62 MeV/(mg/cm^2) at normal incidence. The heavy ion cocktail at JYFL consists of N, Ne, Si, Ar, Fe, Kr and Xe ions at energies up to 9.3 MeV/nucleon

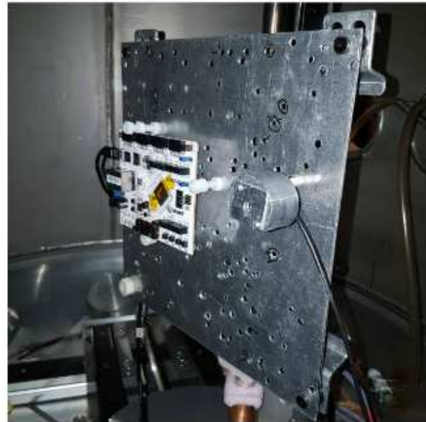

Figure 4.13: The vacuum chamber with a DUT installed at the low-energy proton and heavy-ion line

(1217 MeV for xenon) [54]. The irradiations at the heavy ion beamline are performed in the vacuum chamber, as seen in Fig. 4.13.

4.3.5 The High Energy Proton Line

The high energy proton beamline receives protons directly from the K130 cyclotron. The beam energy can be varied from 60 MeV down to about 10 MeV using degraders and by changing the energy of the beam from the cyclotron. The tests at this beamline are performed in air.

4.4 CERN Radiation Environment and CHARM Facility

The CHARM facility was conceived as a part of the Radiation to Electronics (R2E) project at CERN, Switzerland. The purpose of the facility was to provide a mixed-field environment which would emulate as closely as possible the radiation environment within the different areas of the CERN accelerator complex, notably the LHC. The radiation environment at the CERN accelerator complex is characterized by a high range of energies and fluences of protons, neutrons, photons muons and electrons in its accelerator complex. The CHARM mixed-field is achieved by shooting a 24 GeV proton beam one of the targets in the facility.

This representative mixed-field environment at CHARM can then be used to test and validate electronics meant to be used within the accelerator complex. In addition to the CERN radiation environment, depending on the facility configuration, the radiation field can also be used to test for different space- and ground level applications [9].

The three main components describe the facility configuration:

- The test position within the facility, as seen in Fig. 4.14
- The position of the four shielding walls within the facility
- The choice of one of the three targets, or no target in the beam

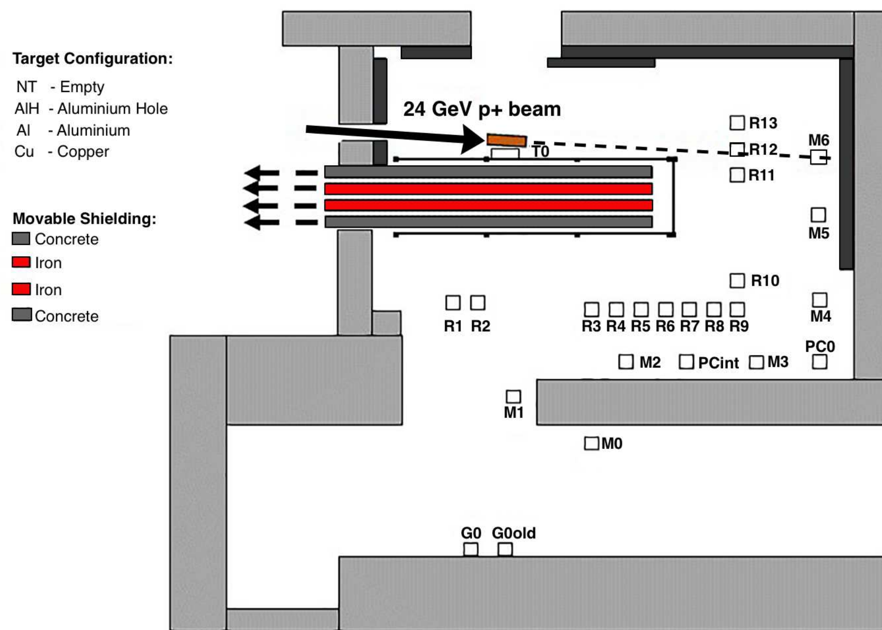

Figure 4.14: An overview of the test positions at the CHARM facility [59]. The test performed in the scope of this work were performed in position G0.

The choice of the target and the shielding materials modify the radiation field present in the irradiation area. Depending on the application, the target radiation environment and the required radiation exposure parameters (dose, fluence), the optimal settings can be achieved by also choosing the test position. A detailed study of the most crucial radiation parameters related to each facility configuration has been performed in [59]. The quantities that are most important for electronics testing are the high-energy hadron equivalent fluence (HEH) and the dose. The HEH fluence is defined as the fluence of hadrons (neutrons, protons, pions, and kaons) with energy above 20 MeV plus a weighted contribution from neutrons in the 12 MeV to 20 MeV range [9]. The HEH fluence is most relevant for the SEE research, as this quantity can be related to standard proton testing as described in [9].

4.5 Devices Overview

4.5.1 The ESA SEU Monitor

The first electron experiments conducted in this work were performed on the ESA SEU monitor, which will be used as a representative example of SEU simulation analysis, also

performed on other devices detailed in chapter 6. The ESA monitor is an SEU-based particle detector, which has been calibrated in a broad range of test facilities and can, therefore, be used as a reference when employed in test conditions for which it has been previously characterized [60–63]. The detector and an example of a readout of the 4 SRAM memories on the device can be seen in Fig. 4.15. The ESA Monitor is accompanied by software that allows monitoring the physical location of SEUs in the memories. Therefore, in addition to the SEU cross sections, beam homogeneity can also be evaluated.

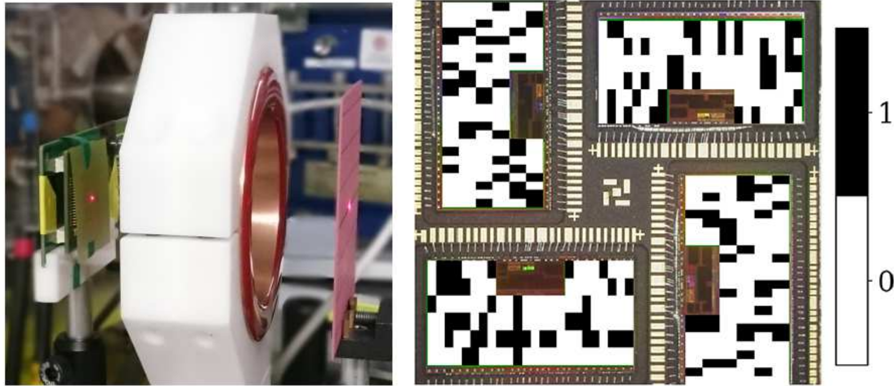

Figure 4.15: left) The ESA SEU Monitor depicted at the test position at the VESPER beamline behind a FBCT and the BTV detectors right) An example of a readout of the ESA SEU monitor during one of the tests showing the number of SEU read per block of SRAM memory and demonstrating the beam homogeneity [1, 2]

As a first step, since the ESA monitor electron-induced upset rate had not been characterized in an electron beam previously, its performance could be evaluated using a semi-empirical Monte Carlo based RPP (Rectangular Parallelepiped) model, as described in [64, 65]. The model uses both available data and assumptions about the sensitive volume and the surrounding geometries in combination with experimental data from proton test from the 30 MeV − 230 MeV energy range to estimate the cross-section for particles and energies for which the Monitor has not been tested for [66]; the procedure is described in more detail in chapter 5.

4.5.2 The Single-Event Latchup Memories

Another type of device mentioned in this chapter will be Static Random Access Memories (SRAM) which are sensitive to Single-Event Latchup (SEL). The memories discussed are shown in detail in Table 4.7. The memories were three SRAM memories from three different manufacturers (ISSI, Brilliance, and Alliance). A summary of the three memories can be seen in Table 4.7. The Brilliance device has been characterized by both a heavy-ion beam and proton beams [67, 68], where they were referred to as SRAM F and BS62 respectively [3]. The Alliance and the ISSI memories are referred to in [67] as SRAM C, and SRAM A respectively.

Table 4.7: A summary of the SRAM memories tested at VESPER [67]

Shorthand	Version	Size	Technology Node
Brilliance	BS62LV8001BIP55	8 Mbit	180 nm
ISSI	IS61LV5128AL-10TLI	4 Mbit	180 nm
Alliance	AS7C34098A-10TCN	4 Mbit	200 nm

The SEL memory experiments were conducted at the VESPER test bench located at the CLEAR experimental area at CERN [1]. The test board was attached to the movable table which was moved in the beam for testing [3]. The SEL memories can be seen in a testing setup on Fig. 4.16.

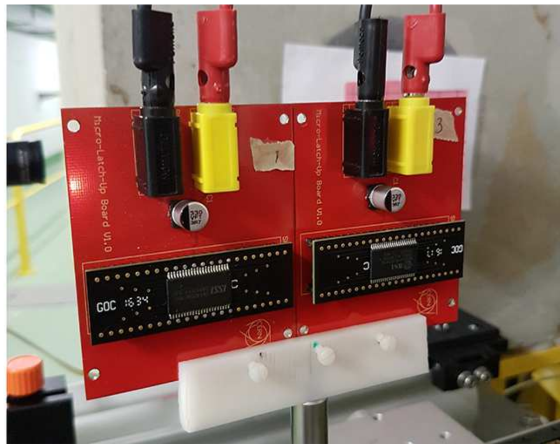

Figure 4.16: The SEL memories setup for latchup testing at the VESPER testbench [3]

4.5.3 Artix 7 Test Board Arty

The Arty is a 28 nm Artix-7 based FPGA test board. All of the Arty tests were performed on the Block memory (BRAM) of the FPGA at nominal voltage. The BRAM was programmed to a checkerboard pattern and periodically read back through the onboard UART connection. The Arty can be seen in Fig. 4.17 at the test position of the RADEF facility medical linac. The package of the Artix-7 FPGA on the board was opened before low-energy proton testing.

4.5.4 CERN SEU Tester

The CERN SEU Tester is a generic SRAM memory tester developed by the TEC-EPC-CCE and EN-STI-BMI sections as a part of this thesis work. The SRAM tester is based on a radiation hard Microsemi FPGA which controls the SRAM memory and also the UART

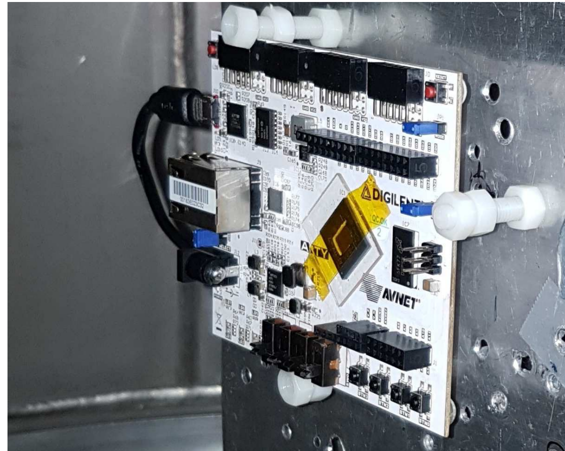

Figure 4.17: The 28 nm Artix-7 based FPGA test board Arty at the RADEF facility

communication with the tester itself. The tester, which can be seen in Fig. 4.18, has two external power inputs: the 5 V input for the FPGA and the DUT power input which can be varied and is nominally 3.3 V. The main parts of the tester are the tester board itself and daughter boards where various SRAM memories can be attached, for different memories only the FPGA has to be reprogrammed; therefore the tester can be used with any SRAM memory as long as a program is prepared for it in advance.

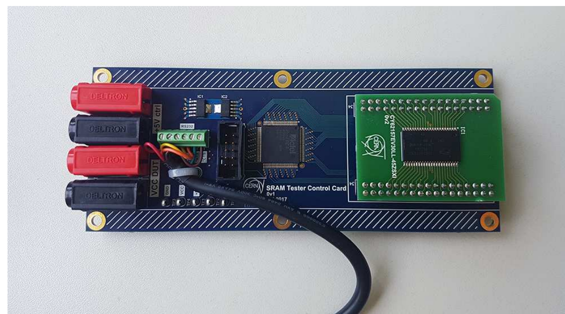

Figure 4.18: The CERN SEU Tester board. External power connections, the UART connection and the FPGA on the left. The SRAM daughter-board with one of the SRAM connected on the right.

The main program for the tester writes a checkerboard pattern to the SRAM and then reads the memory back when a read command is sent to it. Currently, the tester has been set up for the following memories

- Cypress CY62157EV30LL-45ZSXI - 90 nm tech.
- Cypress CY62167EV30LL-45ZXA - 90 nm tech.
- ISSI IS6164WV204816BLL - 65 nm tech.

In addition to the electronics, a PyQt5 based graphical user interface (GUI) has been created as a part of the thesis work. The user interface offers an easy way to control the SRAM tester independently of which memory is connected. The GUI overview with a

few SRAM testers under test can be seen in Fig. 4.19. The output of the tester is in hexadecimal format, and the output is converted to a human-readable form by the GUI, which also shows the live updates for the upsets in the device.

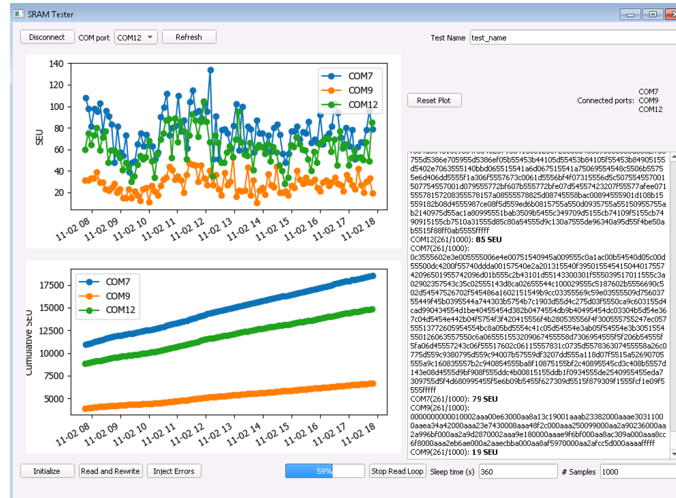

Figure 4.19: The CERN SEU Tester GUI developed as a part of the thesis work

5 Radiation Effects Simulation

As in the standard cases of ions and protons, the probability of electron-induced single-event effects in devices depend on a variety of test, beam particle type and energy and device sensitive region parameters. Some of the considerations that have to be included in the analysis are:

- The energy of the beam particle. Depending on the energy range of the incoming electron, different mechanisms causing the upsets in the electronics dominate;
- The particle type. Depending on the particle type, the energy deposition mechanisms are different. Understanding the dominant physical mechanism is the only way to accurately interpret and describe the radiation hardness of a device, relating the electron-induced effects to other particle types gives essential insight into the kind of mechanisms caused by electrons;
- The physical mechanisms of the effect that is considered;
- The back-end-of-line composition, as the material in and surrounding the sensitive volume might generate additional particles or enhance the total error rate;
- The materials around the electronics. Due to electrons creating a large amount of secondaries due to bremsstrahlung and nuclear interactions, the energy spectra of the particles, the deposited energy in the sensitive areas and the LET-values of the generated secondaries have to be carefully considered. Due to the secondary particles having different mechanisms for causing upsets, all of the secondary particles have to be taken into account for the final upset rate;
- The technology node and the type of device for which the effects are considered. Given that the critical energy of the technology nodes is different, different effects dominate the upset rate. Depending on the amount of energy each effect deposits, the overall energy range and cross-section of the upsets can vary by a significant amount.

There are guidelines for radiation hardness assurance commonly used by industrial actors and enforced by agencies for example for space missions or high-energy physics environments. The standards most frequently used by the European Space Agency are called the European Space Component Coordination (ECSS) Radiation Standards and Guidelines which give guidelines also for the actual testing procedures, which in turn can be used to guide the simulations performed to estimate the upset rates, where testing in the real environment is

not possible or reasonable.

Several generations of devices, described in chapter 4, have been tested as a part of this thesis work, as detailed in chapter 6. The choice and details of the related simulations performed in FLUKA can be found in [1, 2].

5.1 Inelastic Interactions

Several hypotheses exist in terms of which dominating physical mechanism is behind electron-induced single-event effects, as detailed in section 2.5. One of the possible hypothesis is the electro-nuclear effects [1, 29], and for lower critical charges Rutherford electron/nuclei elastic scattering as shown in [31], as well as direct ionization.

Single event effects caused by high-energetic electrons in devices with high critical charges, such as the ESA SEU monitor, introduced in section 4.5.1, can be attributed mainly to fragments produced by the indirect interaction of electrons and photons with the silicon nuclei in or near the sensitive volumes [16]. This is similar to the mechanism through which protons cause single event effects [69], however, the probability of such events occurring due to electrons is much lower, due to the lower inelastic interaction cross-section of electrons compared to protons. To estimate the differences in single-event cross-sections, as a first estimate the raw cross-sections of the different particles: electrons, photons, and protons were obtained from FLUKA [33].

Also, the inelastic interaction cross-section was simulated using FLUKA, which clearly shows this higher probability for proton interactions compared to electrons and photons in Fig. 5.1. One can also note the great dipole resonance at around 20 MeV for photons. This resonance is expected to contribute to the sudden increase in SEU cross-section for photons around this energy range.

The cross-section for electrons is about an order of magnitude lower than for photons for energies above the resonance. The relative difference in inelastic cross-sections can also be observed when performing experiments where the photons are generated by introducing a target material. The change in cross-section will be discussed in chapter 6. In addition, the difference between electrons and protons is about three orders of magnitude, which is also reflected in the SEE cross-sections shown in chapter 6. Due to this, a link between the inelastic interactions and the upsets in the devices tested can be assumed, provided that, as will be shown later, the generated fragments are similar. As discussed in [1, 2], due to the critical charge of the device and therefore the required amount of deposited charge, the experimental results for the high critical charge (10 fC) device point to nuclear interactions.

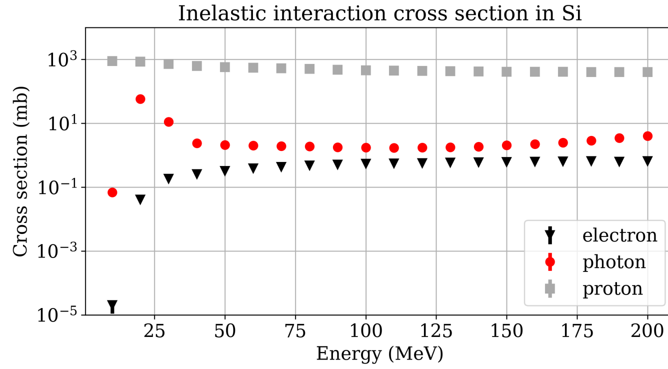

Figure 5.1: Inelastic interaction cross-section for photons, neutrons and electrons interacting with a Si target [1]

5.2 Silicon Recoils and Fragments

Nuclear interactions of electrons and silicon atoms generate a variety of recoils and fragments. These products can deposit a large amount of charge in a tiny volume. If the reaction occurs within or near the sensitive region of the device, the charge deposited by the recoils can be sufficient to cause an upset. To further study these interactions, several FLUKA simulations were performed.

The FLUKA simulation were performed using a 200 MeV electron, photon and proton beam impinging on a 5 µm side cubic silicon target, as seen in Fig.5.2, and then scoring for the desired quantities.

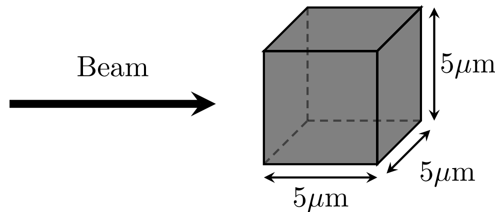

Figure 5.2: The FLUKA geometry of the silicon recoil simulation. The silicon target and the beam direction are shown

The results for the distribution of the LET, seen in Fig. 5.5, and charge, seen in Fig. 5.3, of all nuclear reaction products created was analyzed. In addition, simulations to compare the kinetic energy per nucleon, seen in Fig. 5.4, and scattering angle, seen in Fig. 5.6 of only the heavier recoils ($Z > 9$) were performed. All of the resulting simulations were normalized to the inelastic interaction cross-section for a direct comparison between the particles.

The simulations showed a very similar distribution of charge and kinetic energy for photons and protons, while the electron value for electrons was about one order of magnitude

smaller for larger energies. The same result was seen for the LET distribution, here the highest LET produced by protons and photons is about 15 MeVcm^2/mg while for electron it's about 14 MeVcm^2/mg. The distribution of the scattering angles is much more uniform for electrons, while protons and neutrons have mostly smaller scattering angles. The maximum charge of the recoils is also similarly lower for electrons.

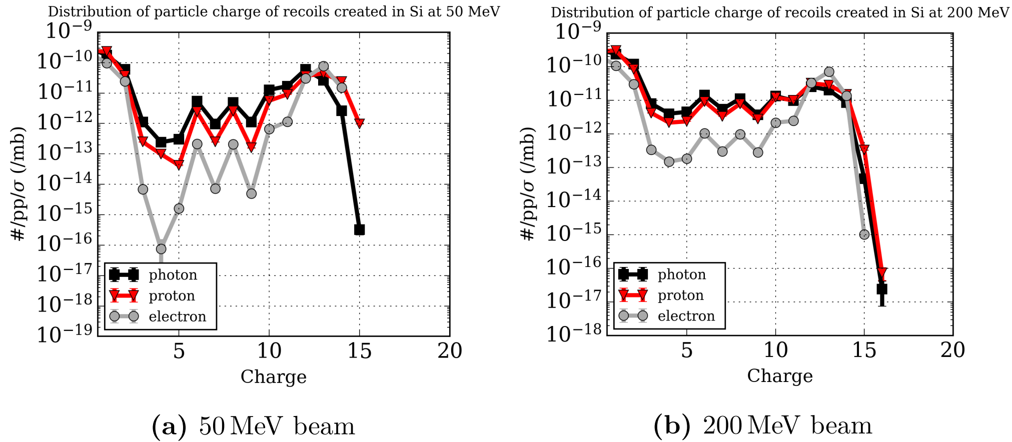

(a) 50 MeV beam **(b)** 200 MeV beam

Figure 5.3: Distribution of charge of recoils from electron beam interaction with silicon [1]

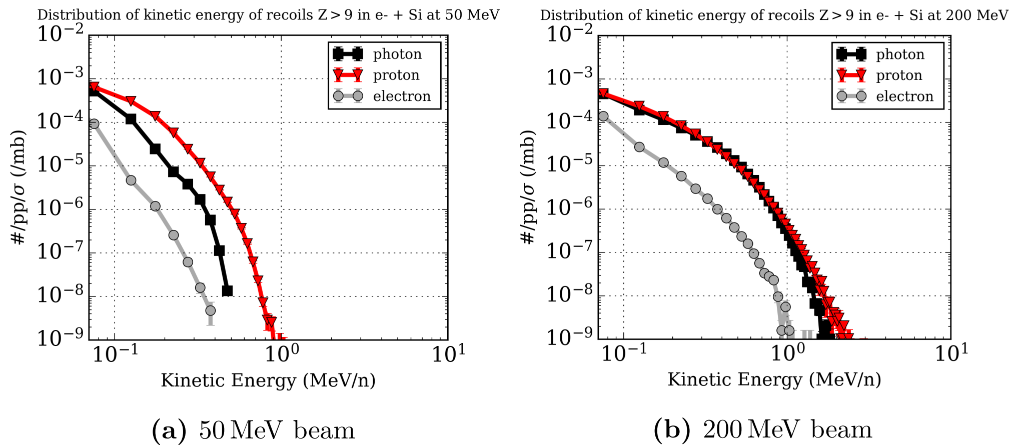

(a) 50 MeV beam **(b)** 200 MeV beam

Figure 5.4: Distribution of kinetic energy of recoils from electron beam interaction with silicon [1]

A significant result from the simulations is the fact that both the kinetic energies and LET distributions of recoils generated by photons and electrons are sufficient to cause upsets in certain classes of electronic devices. It can, therefore, be assumed that at higher energies the mechanism by which upsets are created in electronic devices with a high critical charge is similar for both electrons and protons, i.e. nuclear reactions.

What is more, the LET of the nuclear reaction products created here is much higher than that of the Rutherford or Coulomb scattering. For an elastic electron/Si scattering recoil to cause an upset, the deposited charge needs to be higher than the critical charge for a given device. For the ESA SEU monitor, the critical charge is considered to be about

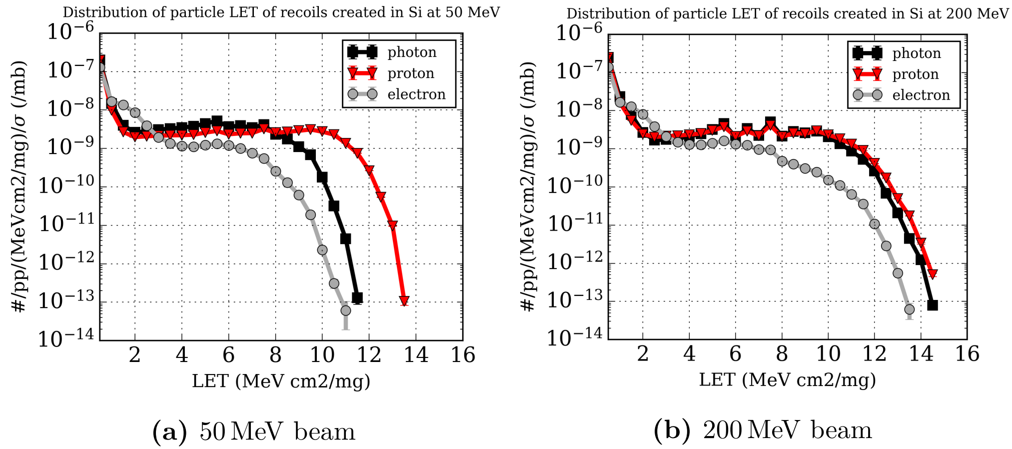

(a) 50 MeV beam **(b)** 200 MeV beam

Figure 5.5: Distribution of LET of recoils from electron beam interaction with silicon [1]

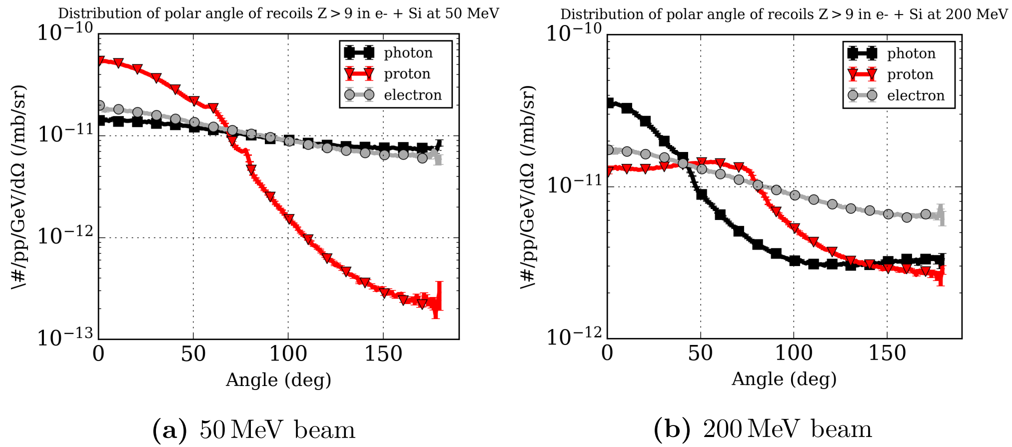

(a) 50 MeV beam **(b)** 200 MeV beam

Figure 5.6: Distribution of angle of recoils from electron beam interaction with silicon [1]

10 fC [70]. As discussed in [28], the maximum charge an elastic recoil can deposit when interacting with a 20 MeV electron is about 0.5 fC. Therefore, it is impossible that an upset caused by an elastic interaction recoil takes place in the ESA SEU monitor leading to the conclusion that for irradiations at medical linacs operating up to 20 MeV, the mechanism is disregarded as a contributor to the total SEU cross section for high critical charge (10 fC) devices [2].

5.3 Tungsten Fission Fragment Simulation

Modern electronic devices often contain high-Z materials such as tungsten near the sensitive volumes in the layer interconnects. Previously, the nuclear reaction products or fission fragments created by particles interacting with these materials was performed for protons in [71]. Simulations were performed as a part of this thesis to extend this work and

Table 5.1: Inelastic interaction cross-section for electron, photons and protons used to normalize the results of the FLUKA tungsten recoil simulation

Energy (MeV)	Electron XS (mb)	Photon XS (mb)	Proton XS (mb)
50.0	0.325	2.1	578.0
200	0.648	3.98	403.0

characterize the nuclear reaction products created by photons and electrons in tungsten [3].

It was previously shown in [72] that heavy-Z materials such as tungsten near sensitive volumes in devices increase the SEU cross-section for proton testing. The increase is due to the fission fragments created by nuclear reactions between protons and tungsten, which deposit large amounts of energy in the sensitive volumes in the device. A FLUKA simulation was performed to investigate if the increase in the cross-section is also present with an electron beam. The simulation consisted of beams of protons, photons or electrons hitting a 5 µm × 5 µm × 5 µm side tungsten cube. The following parameters of the fission fragments were scored: LET in silicon, seen in Fig. 5.7, the charge, seen in Fig. 5.8 and the kinetic energy seen in Fig. 5.9. All these scored quantities were normalized to the inelastic interaction cross-section, as seen in Table 5.1 [3].

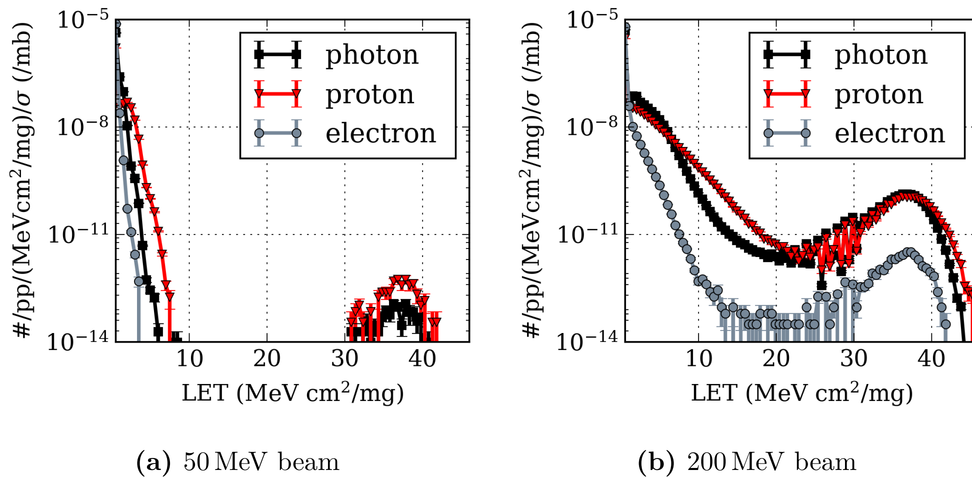

(a) 50 MeV beam **(b)** 200 MeV beam

Figure 5.7: Simulation of the LET of fragments generated by interaction with tungsten of protons, electrons and photons.

As shown in Fig. 5.7, the fission fragments created by the proton beam interaction with tungsten have LETs up to ∼45 MeV cm^2/mg. As shown in [71], these high-LET fragments are the root cause for the increase in cross-section in devices with high LET threshold

values in proton beams with energies between 200 MeV and 500 MeV. As seen in Fig. 5.7, electrons are similarly capable of creating these high-LET fission fragments, reaching LET values of ∼40 MeV cm^2/mg. Therefore, in theory, electrons are equally capable of inducing the increase in cross-sections with high enough beam energies. The increase in cross-section creates a strong energy dependence in the cross-sections. As both protons and electrons are capable of producing fission fragments with high enough LETs, this dependence is therefore present in both electron and proton beams. As discussed in chapter 9, this can have strong implications for the related radiation hardness assurance. As seen in Fig. 5.7 on the left, at lower beam energies only silicon-like and tungsten-like secondary recoils are present [3]. As the beam energy increases, tungsten fragments around Z∼ 37 Z_w/Z are produced in a more significant proportion.

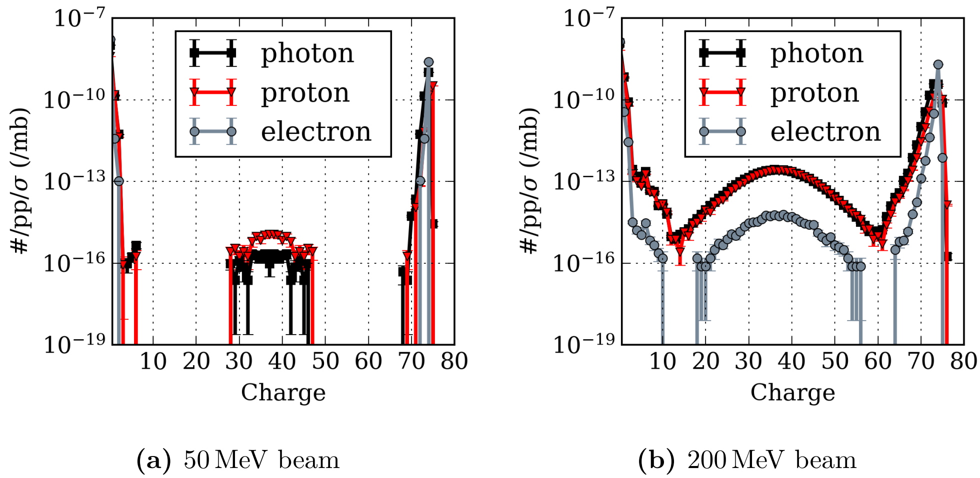

(a) 50 MeV beam

(b) 200 MeV beam

Figure 5.8: Simulation of the atomic number of the fission fragments generated by interaction with tungsten by protons, electrons and photons [3].

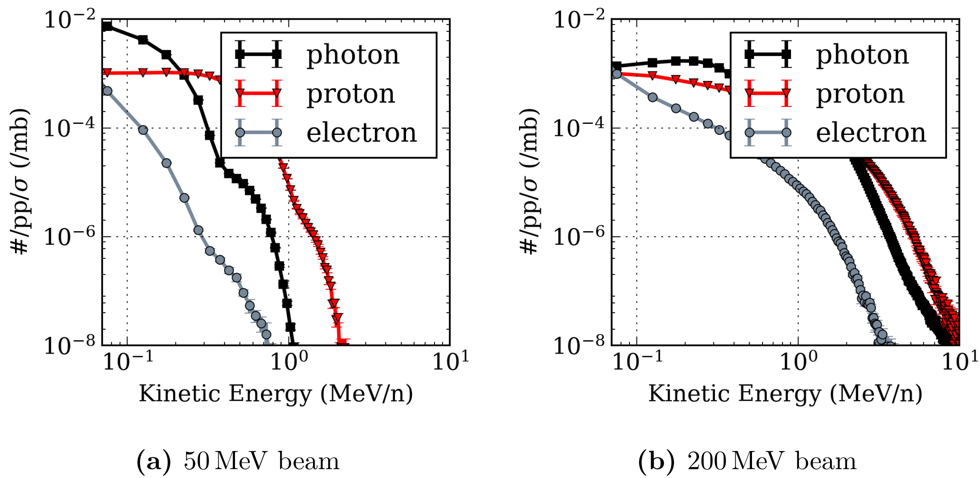

(a) 50 MeV beam

(b) 200 MeV beam

Figure 5.9: Simulation of the kinetic energy of recoils generated by interaction with tungsten by protons, electrons and photons.

5.4 Monte Carlo Method for Estimation of SEE Rates

5.4.1 Event-by-Event Energy Deposition Simulation

An important aspect in trying to understand the exact mechanisms by which electrons deposit energy in the device is to look at the event-by-event distribution of the charge deposited in the sensitive volumes of the device under test.

A set of FLUKA user routines was developed by Ketil Røed, as specified in [70], for scoring of the energy deposition events in specified sensitive volumes. These routines provide a versatile means of scoring these events. The routines have also been extended by R. Garcia Alia in [70] to include biasing, the use of heavy ions and use of particle spectrum as a source, in addition to defining different charge collection efficiency regions within the sensitive volume.

The scoring routine is based on two standard FLUKA routines: the comscw.f routine, called after every energy deposition step, and the urseou.f routine, called after each primary particle run. The information about the energy deposition steps in the scoring regions is stored in the comscw.f variables and processed in usreou.f from where the event-by-event energy deposition histogram is filled. A detailed description of all the FLUKA cards and their purpose is detailed in [70]. The output by the event-by-event energy deposition is a histogram with the number of event per incident particle and energy bin.

As an example of the approach, the ESA SEU monitor, with transistor size of 0.25 µm, a geometry with a sensitive volume dimensions of 3 µm × 3 µm × 0.5 µm was chosen, the geometry can be seen in Fig. 5.10. As detailed in [1, 2], the choice of the sensitive volume depends on the technology node of the device. In addition, an understanding of the layers above the sensitive volume, the so-called back-end of line (BEOL), is necessary. The geometry BEOL is a stack of aluminium and silicon dioxide layers (no high-Z materials are present in this geometry), with the bottom layer representing the active silicon, which also contains cubes of sensitive volumes for energy deposition scoring, which can be seen in Fig. 5.10. The sensitive volumes were replicated 25 times to improve the statistics of the simulation [1].

5.4.2 Monte Carlo Method for Estimation Using Energy Deposition Curves

As described in more detail in [70], once the differential event-by-event energy deposition histograms are produced, the corresponding SEE cross section can be estimated as a function of the response function of the component. For deposited energy or charge E_{dep},

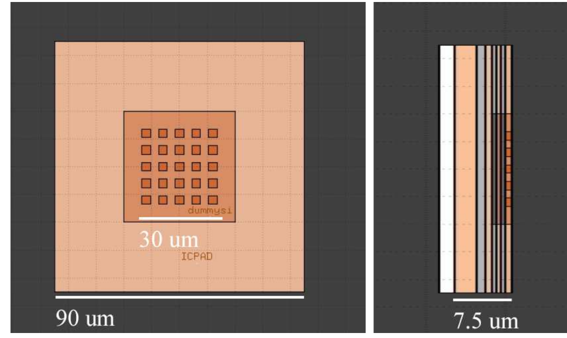

Figure 5.10: Geometry used for the simulation of energy deposition for the ESA SEU monitor detailed in [1].

we can assume there is an associated probability $w(E_{dep})$ that the event will lead to an SEE. The general form to calculate the cross-section of a device is

$$\sigma = \frac{N}{\Phi} \tag{5.1}$$

where Φ is the beam fluence in cm^2 and N is the number of SEE. Then the simulation can be used in a similar manner where the beam surface S is equal to the fluence Φ and the number of upsets N becomes the probability of convoluting the differential energy deposition curve with the SEE probability function. In a simplified assumption, for the beam to be able to cause an SEE, the beam has to deposit a larger amount of energy than a specific threshold charge. The value is an intrinsic property of the device and upset type and is called the critical charge. The energy spectra in converted to charge using

$$\text{eV to fC} = 1.602 \times 10^{-19} * 1 \times 10^{15}/3.6 \tag{5.2}$$

where 1.602×10^{-19} C is the elementary charge and 3.6 eV is the energy required to create an electron-hole pair in silicon. The typical value used is also 22.5 MeV pC^{-1}. With the assumption of the critical energy threshold, the probability function becomes a step function. As explained in [70] and shown in Eq. 5.3, the cross-section, or probability, value is then the reverse integral of the energy differential energy deposition curve H_{ecrit} above the critical energy.

$$\sigma = \frac{N}{\Phi} = \frac{H_{ecrit}}{1/S} \tag{5.3}$$

Examples of this approach can be seen in section 5.5.4, section 5.5.1 and section 5.5.2.

The estimation of the cross-section given by the step-function method typically overestimates the actual cross-section and the probability function chosen in real-life situations is the 4-parameter Weibull function seen in Eq. 5.4, where σ_{sat} is the saturation cross-section, E_i is the current energy being analyzed, E_0 is the onset energy, s is the shape and

w is the width parameter of the Weibull function.

$$\sigma(E) = \sigma_{sat}\left(1 - \exp\left(-\frac{E_i - E_0}{w}\right)^s\right) \tag{5.4}$$

5.4.3 Estimation of SEE Rates with Experimental Heavy Ion Data

Assumptions have to be made about device sensitivity to radiation to estimate its SEE cross-section. The assumed sensitivity can be described by a probability function using knowledge about the device properties (SV size, BEOL composition), as described in section 5.4.2, or obtained experimentally through heavy-ion testing.

The heavy-ion cross section is folded with the differential event-by-event energy deposition curves discussed in section 5.4.1 to estimate the cross-section of the device for other particles. An example for the ESA monitor Weibull fit together with an example of one of the energy deposition curves can be seen in Fig. 5.11.

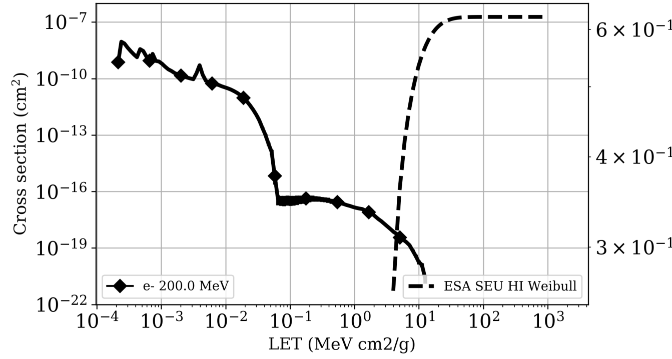

Figure 5.11: The ESA SEU monitor experimental heavy ion Weibull fit and a FLUKA simulated energy deposition curve or $p(E_p, E_d)$ in Eq. 5.5, here shown as a function of LET, whereas the folding is equally applicable as a function of energy. The folding of these curves will yield in a cross-section estimation for the simulated beam energy.

The folding of the curves is described in Eq. 5.5.

$$\sigma_p(E_p) = \int \sigma_{HI}(E_d) p(E_p, E_d)\; dE_d \tag{5.5}$$

where $\sigma_p(E_p)$ is the experimental SEU cross-section for each particle, σ_{HI} is the SEU monitor heavy ion cross-section, $p(E_p, E_d)$ is the probability of depositing a charge E_d in the sensitive volumes in the ESA SEU monitor RPP model [70, 73], and correspond to the differential distributions shown in Fig. 5.11. The variables for the heavy-ion Weibull fit are: saturation cross-section of 3.72×10^{-8} cm^2/bit, a LET threshold of 3.0 MeV cm^2/mg, W of 21.78 MeV cm^2/mg and s of 0.66 [1].

5.4.4 Estimation of SEE in a Simulated Environment

The estimation of upset rates is also possible using simulated radiation environments by using the particle-specific cross-sections obtained through the heavy-ion cross-section, as explained in section 5.4.3. This becomes useful when the exact particle composition and energy spectra of the beam are essential, or the environment is complex, consisting of many particles and energies, such as the CHARM facility at CERN or the Jovian Radiation environment. The simulation allows in addition to assessing the amount of secondary radiation created by the beam passing through various components in the beamline, such as for the VESPER facility.

The simulated particle fluxes are folded with the Weibull responses for each particle to estimate the contribution of each particle to the total cross section, these were estimated in [1]. The folding of the simulated fluxes and the Weibull function is described as:

$$N_i/pp = \int \frac{d\phi_i(E)/pp}{dE} \cdot \sigma_i(E)\, dE \tag{5.6}$$

where N_i is the expected number of upsets per primary particle from FLUKA, $\frac{d\phi_i(E)/pp}{dE}$ is the differential flux per primary particle in #/MeV/pp and $\sigma_i(E)$ is the Weibull estimated cross section for the given particle.

Finally, to obtain the estimated cross section σ_{calc}, the result N_i/pp has to be normalized to the total integrated flux of electrons per primary particle ϕ/pp. Therefore the estimated cross-section σ_{calc} can be found as

$$\sigma_{calc} = \frac{N_i/pp}{\int \phi(E)/pp\, dE} \tag{5.7}$$

It is to be noted that even if Eq. 5.7 the electron flux is considered for the cross-section calculations, the contribution to the latter of the secondary particles (e.g. photons produced in component package) is found through Eq. 5.6.

5.5 Energy Deposition Simulation

The geometry for the ESA SEU monitor, shown in Fig. 5.10, is used for the following energy deposition simulations performed in FLUKA.

5.5.1 FLUKA Biasing Validation

An important aspect of the simulation is the biasing of electro- and photo-nuclear interactions in FLUKA. Both electro- and photo-nuclear cross-section require a long simulation time to produce even a single reaction. Therefore, due to the exceedingly low cross-sections

heavy biasing was used for both electron and photon beam simulations, as seen in Fig. 5.12. The biasing option that was used is the LAM-BIAS, which is used to bias the inelastic nuclear interaction length of hadrons, photons, electrons, and muons [43].

LAM-BIAS Mat: SIO2_2 ▾	Type: INEPRI ▾ Part: 3-HELIUM ▾	× mean life: to Part: @LASTPAR ▾	× λ inelastic: 2E-3 Step:
LAM-BIAS Mat: Si_2 ▾	Type: INEPRI ▾ Part: 3-HELIUM ▾	× mean life: to Part: @LASTPAR ▾	× λ inelastic: 2E-3 Step:
LAM-BIAS Mat: Al_2 ▾	Type: INEPRI ▾ Part: 3-HELIUM ▾	× mean life: to Part: @LASTPAR ▾	× λ inelastic: 2E-3 Step:
LAM-BIAS Mat: SILICON ▾	Type: INEPRI ▾ Part: 3-HELIUM ▾	× mean life: to Part: @LASTPAR ▾	× λ inelastic: 2E-3 Step:
LAM-BIAS Mat: ALUMINUM ▾	Type: INEPRI ▾ Part: 3-HELIUM ▾	× mean life: to Part: @LASTPAR ▾	× λ inelastic: 2E-3 Step:
LAM-BIAS Mat: Si_sens ▾	Type: INEPRI ▾ Part: 3-HELIUM ▾	× mean life: to Part: @LASTPAR ▾	× λ inelastic: 2E-3 Step:
LAM-BIAS Mat: SIO2 ▾	Type: INEPRI ▾ Part: 3-HELIUM ▾	× mean life: to Part: @LASTPAR ▾	× λ inelastic: 2E-3 Step:

Figure 5.12: Biasing applied to different regions of the geometry to enhance the photo- and electro-nuclear interaction cross-sections

An essential aspect of biasing is the need to ensure that the biasing result is normalized so that the final result does not differ from the unbiased result. Therefore, to verify that this is the case, a comparison between the energy deposition between FLUKA and CRÉME MC was performed.

To compare the tools, a simulation with an equivalent BEOL and sensitive volume dimensions were performed. The differences were that in CRÉME MC only a single SV was placed, the CREME MC geometry can be seen in Fig. 5.13. In addition, as there was only one SV and the maximum number of primary particles is limited to the user, the CRÉME MC results have a somewhat lower statistics for electrons due to the small cross-section of electro-nuclear interactions.

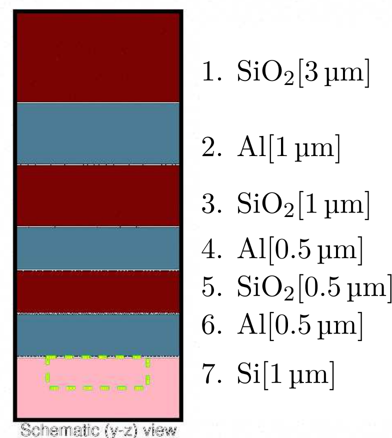

Figure 5.13: CRÉME MC 3 µm side sensitive volume geometry, $\lambda_{inelastic} = 2 \times 10^{-3}$ is equal to biasing factor of 5×10^2

However, what can be seen from the comparison shown in Fig. 5.14, the results have a very good overall match for both proton and electrons. Therefore, even when heavy biasing is

applied in the FLUKA simulations, the total cross-section results do not change, when compared to benchmark tools.

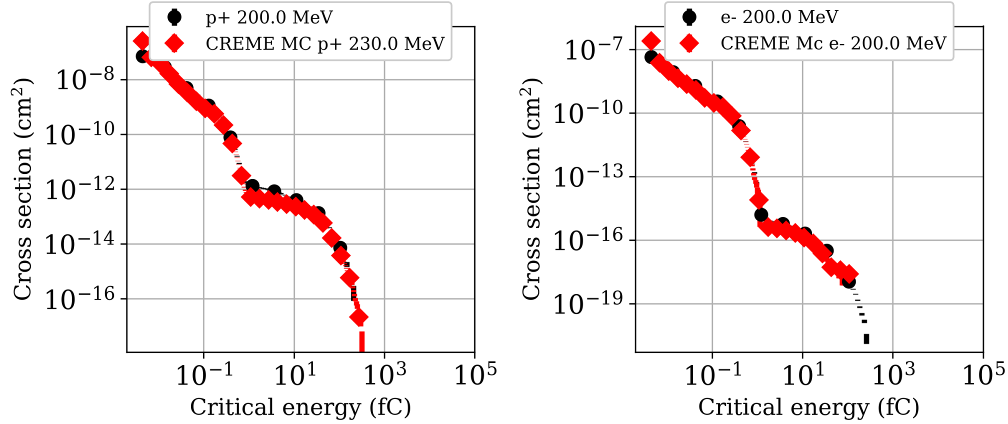

Figure 5.14: Comparison between CREME MC and FLUKA results for a 3 µm side sensitive volume geometry

5.5.2 Energy Deposition Curve per Particle Type

Simulations showing the energy deposition curves by electrons, protons, photons, and neutrons for beam energies of 10, 20, 50, 200 MeV in the geometry shown in Fig. 5.10 can be seen in Fig. 5.15.

The comparison between the energies demonstrates how the deposited charge increases with the increase of beam energy. In addition, the energy deposition curves for charged particles display a clear distinction between the direct and the indirect ionization modes. The direct ionization corresponds to the large cross-section at low deposited charges. On the contrary, the indirect ionization deposits the most significant amount of charge in the sensitive volumes, but the cross-section is much lower due to the low probability of a nuclear interaction occurring at the vicinity of the sensitive volume. While for electrons the direct ionization curve remains roughly the same for different energies (lower deposited charges), for protons and neutrons the change in beam energy has a larger effect. For indirect ionization (high deposited charges, nuclear effects) the impact of increasing energy is visible for all particles, but more so for electrons and photons. This is due to the inelastic interaction cross-section, shown in Fig. 5.1, having a definite energy dependence for these particles.

5.5.3 Effect of Beam Energy on Energy Deposition Curves

A reverse integral of an energy deposition simulation using a 200 MeV beam on the 3 µm × 3 µm × 0.5 µm side sensitive volume geometry is shown in Fig. 5.16. An important

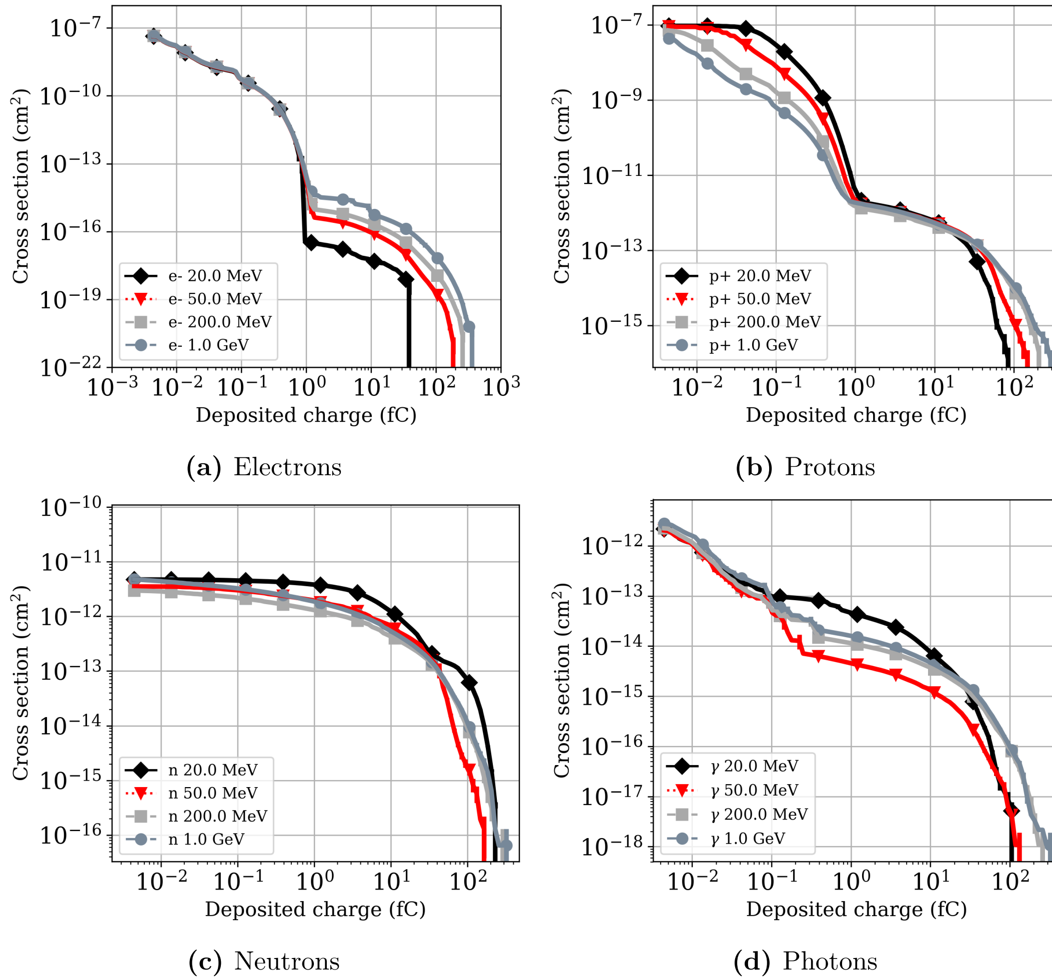

(a) Electrons **(b)** Protons

(c) Neutrons **(d)** Photons

Figure 5.15: energy deposition curves by electrons, protons, photons and neutrons for beam energies of 10, 20, 50, 200 MeV in the geometry shown in Fig. 5.10. Note the different scales used on the y-axis.

finding of these simulations is that one can observe the similar shape but lower cross-section of the energy deposition curve for electrons compared to protons. While the direct ionization curve has a similar cross-section for protons and electrons, the indirect ionization part of the curve has a much lower SEE cross-section. This would indicate that devices having a large enough critical charge value are expected to have a strong energy dependence in the SEE cross-sections, for devices with lower critical charges the cross-section would remain constant with the change of energy. To further study the link between the critical charge of a device and energy-dependence of the SEE cross-sections, further analysis is performed in the following section.

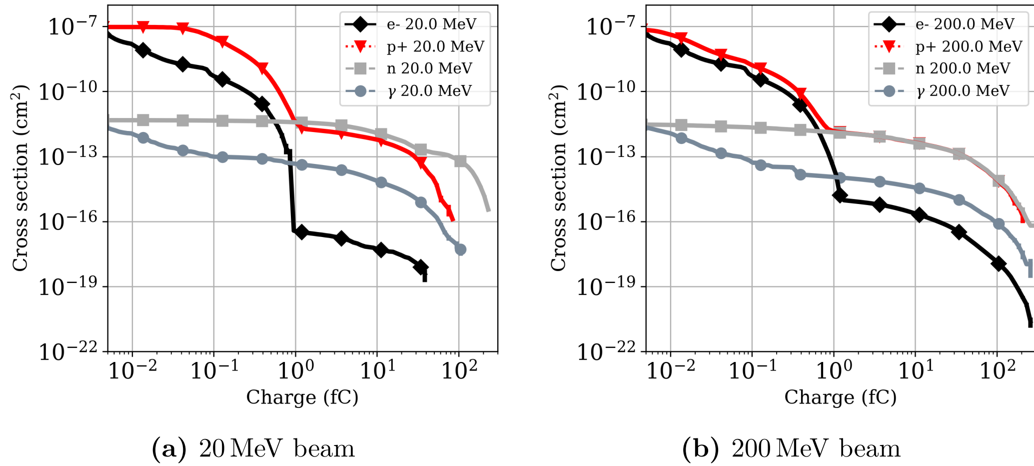

(a) 20 MeV beam

(b) 200 MeV beam

Figure 5.16: Reverse integral energy deposition estimation for the ESA SEU monitor equivalent geometry in FLUKA. [1]

5.5.4 Cross-Section Dependence on Critical Charge

To evaluate how the SEE cross-section as a function of energy depends on the critical charge of a device, the cross-section can be assessed at each considered critical charge. The plots of the dependence can be seen in Fig. 5.17. What emerges from these plots is the clear separation between the direct and indirect ionization dominated cross-sections. For electrons, as seen in Fig. 5.17a, for critical charges larger than 2 fC one can see a cross-section value that is orders of magnitude lower than for 0.8 fC, even for high energies. For protons, seen in Fig. 5.17b, a similar effect can be seen for lower energies, however, for higher energies the difference is not as pronounced as for electrons.

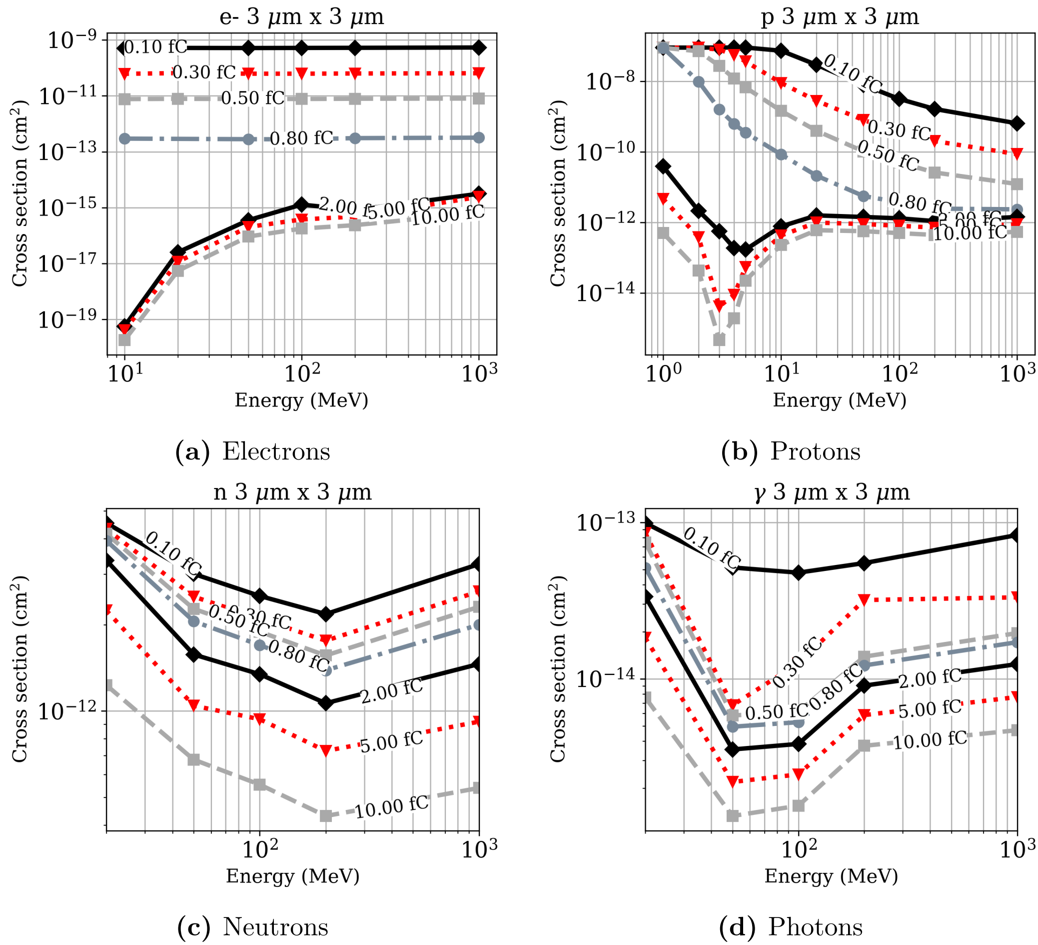

(a) Electrons

(b) Protons

(c) Neutrons

(d) Photons

Figure 5.17: Cross-Section Dependence on Critical Charge

5.6 Effect of Tungsten on the Energy Deposition

To study the effect tungsten, or other high-Z materials have on the cross-section of actual device geometry, a FLUKA simulation was performed on the geometry used in [68, 74]. The geometry in question is of SEL-sensitive SRAM memories, the electron irradiation of which is described in chapter 7 and the memories itself in section 4.5.2. As described previously, electrons and protons cause high-LET fission fragments through nuclear interactions through a similar mechanism; therefore, as the geometry has been already verified for proton testing, it can be assumed to be fitting for electron testing as well. The geometry is shown in Fig. 5.18. The ISSI and Alliance memories were represented with an SV thickness of 2.5 µm and 3.2 µm respectively in [67]. As a first assessment, a 2 µm sensitive volume thickness to describe the various memories was chosen [3].

The geometry consists of 20 µm × 2 µm × 4 µm sensitive volumes arranged in a 5 by 5 grid. The back-end-of-line (BEOL) consists of 5 µm of SiO_2, with a 122 nm layer of tungsten, which is placed 200 nm above the sensitive volumes. The tungsten layer represents the

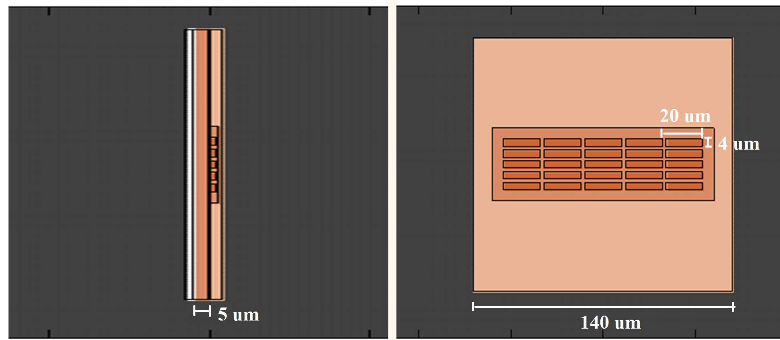

Figure 5.18: Geometry of the sensitive volumes and Back-end-of-line for the tungsten fission fragment simulation

tungsten in interconnects that can be found in many modern devices, such as the SEL-sensitive SRAM described in this work. Although, the BEOL of 5 µm of SiO_2 is a simplification of the actual device geometry, as described in [74], since the cross-section is dominated by silicon fragments, adding SiO_2 or aluminium will not have a significant impact on the overall cross-section.

The FLUKA simulation consisted of a beam of either protons, photons or electrons hitting the BEOL, the cross-section as a function of deposited energy was scored. The resulting cross-section curve can be seen in Fig. 5.19. The cross-section has been normalized by the simulated beam surface and the actual sensitive volume surface [67].

The energy deposition curves for electrons and protons have several noteworthy features. (I) The overall shape of the energy deposition curves is similar between protons and electrons - there is a direct ionization region marked with A, as seen in Fig. 5.19 and an indirect ionization region marked with B. The indirect ionization region is comprised of mostly nuclear interaction products created by the interaction between electrons and protons and silicon atoms. (II) As can be seen in Fig. 5.19, the indirect energy deposition region B shows a very strong dependence on energy for electrons, which is not the case for protons. Points (I) and (II) have been studied in more detail in [1]. (III) The 122 nm tungsten layer in the BEOL of the SRAM geometry enhances the cross-section in region C, as seen in Fig. 5.19. This enhancement is due to the high-LET fission fragments created by the nuclear interactions between the electrons and proton beams and tungsten, as discussed in [71] for protons and shown through FLUKA simulations earlier in this work. The tungsten enhancement effect is stronger for protons due to the higher probability of creating these fragments and their higher LET values. For protons, region C shows a strong dependence of beam energy, confirming the enhancement effect having a strong energy dependence [3].

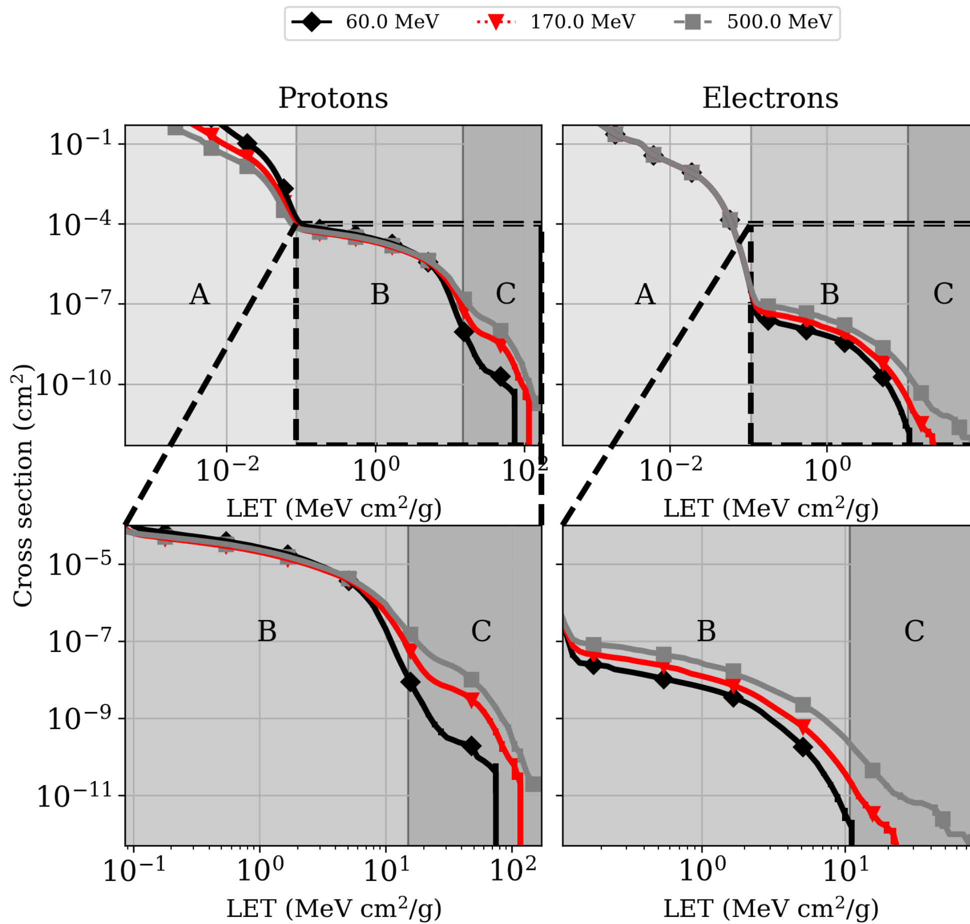

Figure 5.19: Cross-section as a function of LET for the SEL-sensitive SRAM geometry. Bottom row is a zoomed version of the top row to highlight the increase in cross-section due to the tungsten recoils. A) Direct ionisation region B) Indirect ionisation region, silicon recoils C) The tertiary region created by recoils from particle-tungsten interaction [3]

5.7 Shielding Thickness and Material Impact on SEE Rates

The shielding thickness and material are essential considerations when designing spacecraft that have to endure harsh radiation conditions in space. As discussed in section 2.1.1, electrons interacting with materials produce secondary products. As discussed in section 4.1.2, this secondary radiation is an important concern for the JUICE mission which passes through the energetic Jovian radiation belts which contain high fluxes of high-energetic trapped protons and electrons. High-energetic electrons especially produce a large number of secondary photons through Bremsstrahlung. FLUKA studies were performed to assess the effect this secondary radiation could have on the electronics in the Jovian environment.

The FLUKA geometry consisted of different thicknesses of lead, tantalum and, aluminium,

which are common shielding materials, and copper for comparison with experimental results between [1] and [2]. Beams of either electrons, protons, neutrons, and photons were shot on the targets composed of materials above. The impact on the electronics in the spacecraft was assessed in terms of the flux of the secondary radiation related to shielding thickness, the dose increase related to shielding thickness and finally the cross-section increase in a representative device, which in the case of this thesis work was the ESA SEU monitor [3].

5.7.1 Dose

The FLUKA dose simulation scored the evolution of the dose as a function of shielding thickness by adding the shielding materials in front of either a 20 MeV or a 200 MeV electron beam. The shielding thickness is given in terms of g/cm^2, which normalizes material to its density and effectively translates to a weight of shielding and allows for an easier comparison between shielding materials. The comparison between the different shielding materials, seen in Fig.5.20 shows clearly, that while it is possible to successfully shield 20 MeV electrons with even a relatively thin shielding thickness, it is not the case for 200 MeV electrons. The comparison between 20 MeV and 200 MeV beam for the four different materials can be seen in Fig. 5.21, which further highlights the higher deposited dose for the higher beam energies. The higher energy electrons produce a large number of secondaries and these deposit dose within the spacecraft. For all of the shielding materials, a thick shielding is necessary to shield for high energy electrons, which means that it is not practical for space missions. It is worth mentioning, however, that the dose in the trapped electron belts in the Jovian system is expected to be dominated by few tens of MeV of electrons. Therefore the overall shielding effect is still effective at reducing the dose levels inside the spacecraft.

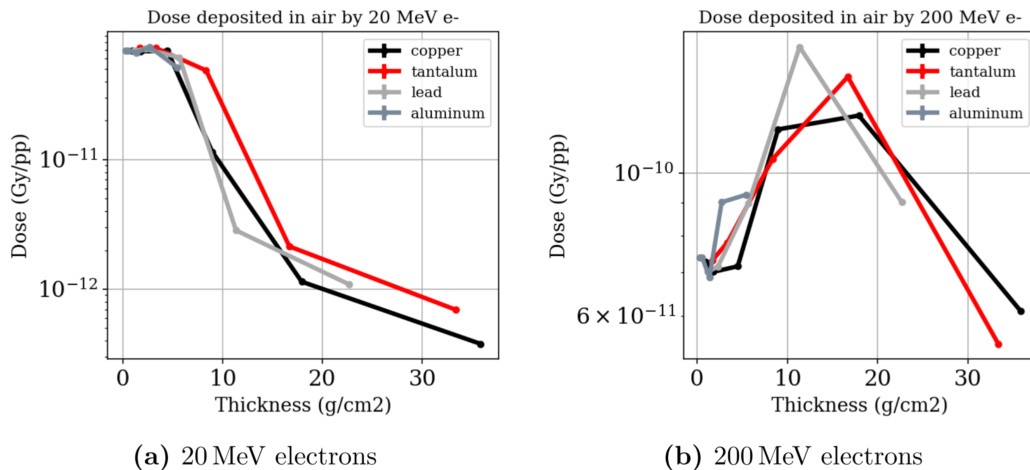

(a) 20 MeV electrons **(b)** 200 MeV electrons

Figure 5.20: Evolution of the deposited dose in air by adding aluminium, copper, tantalum or lead as shielding material in front of an electron beam

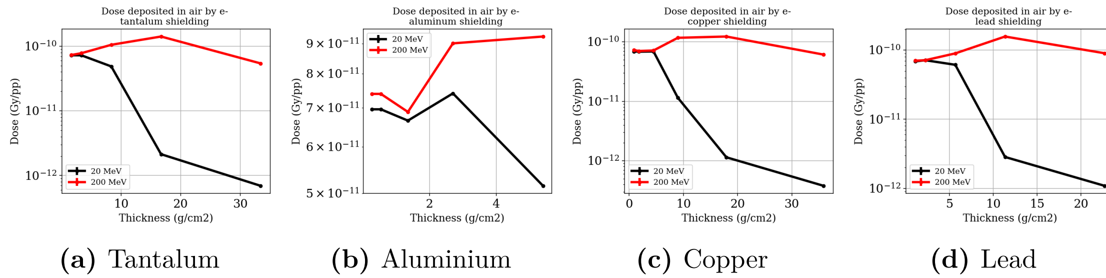

(a) Tantalum **(b)** Aluminium **(c)** Copper **(d)** Lead

Figure 5.21: Evolution of the deposited dose in air by adding aluminium, copper, tantalum or lead as shielding material in front of an electron beam of 20 MeV and 200 MeV

5.7.2 Flux

The flux of the secondaries produced by the passage of particles through shielding material is directly linked to the number of upsets generated in the SEE-sensitive electronics within the spacecraft. A simulation was performed with shielding thicknesses from 1 mm to 40 mm in 20 MeV and 200 MeV photon, electron, and neutron beams. The flux of the particles was scored behind the shielding material, and the resulting flux plots can be seen in Fig. 5.22, where the 200 MeV tantalum and aluminium fluxes are shown as an example.

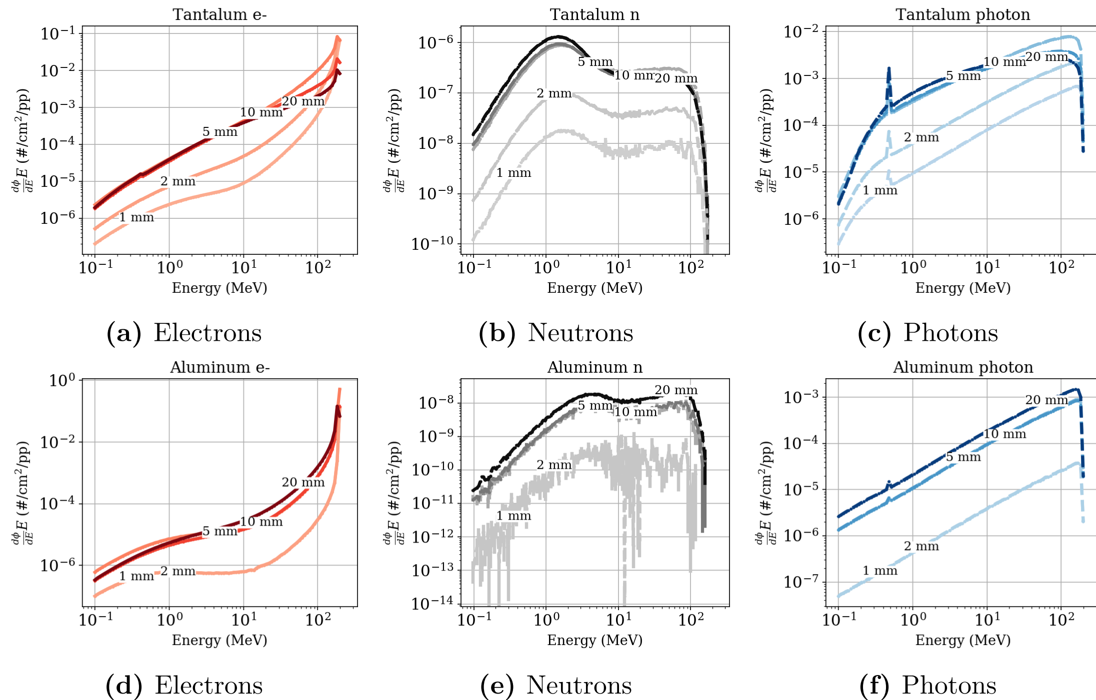

(a) Electrons **(b)** Neutrons **(c)** Photons

(d) Electrons **(e)** Neutrons **(f)** Photons

Figure 5.22: Evolution of the flux of the secondaries created by various thicknesses of shielding materials for a 200 MeV electron beam

Additionally, integrated secondary particle fluxes from 10 MeV to beam energy can be seen in Fig. 5.23. The flux is integrated from 10 MeV because particles with energies higher than this value commonly induce single-event upsets for standard critical charges (see Fig.

5.17) and are therefore the most relevant in terms of analyzing the SEE impact of the secondary particles. The integrated fluxes demonstrate the initial increase of the flux of secondary particles.

The simulations show that

- The flux of secondary radiation increases by several orders of magnitude even after relatively small shielding thicknesses.
- As expected, the denser materials tantalum and lead produce more secondaries, and the particle fluxes are therefore higher than for the less dense aluminium and copper.
- The absolute electron fluxes remain relatively constant regardless of shielding material and thickness.
- It is also worth noting that, as can be seen in Fig. 5.23c, the lower-density materials copper and aluminium did not generate enough secondary neutrons to have any meaningful impact on the cross-section and are therefore excluded.

5.7.3 SEE Cross-Section

To analyze the contributions of different particles to the SEU cross section of the ESA SEU monitor, the various particle spectra, seen in Fig. 5.23, were folded with the corresponding Weibull response for each particle, described in [1], of the monitor and the results can be seen in Fig. 5.25.

The contribution of electrons, neutrons, and photons in the shielding materials can be seen in Fig. 5.24. The result of the folding shows that the contribution of photons to the cross-section is dominant after a few g/cm^2 of shielding materials as can be seen in Fig. 5.24a, the increase of the cross-section for aluminium is about two orders of magnitude for photons. Since aluminium is a commonly used shielding material due to the light weight, the analysis demonstrates the challenges this radiation environment poses for even a relatively old technology. Even though the SEU cross-section for electrons is relatively constant, the real increase in the cross-section induced by the high-energy electrons is due to the secondary photons produced by Bremsstrahlung as the high-energetic electrons travel through the shielding materials [2].

A shown in [1], an experiment was conducted with the ESA SEU monitor by placing a slab of 0.5 cm of copper in front of the SRAM. The increase of the cross-section was factor ~ 5. Both the non-shielded and the shielded test results can be seen in Fig. 5.25. The plot contains the sum of all the contributions to the cross-section from both electrons, neutrons, and photons. The increase in the cross-section through the shielding fits well with the FLUKA simulation results and confirms the effect the secondary photons have on the overall cross-section in electron beams [1]. Fig. 5.24 also shows that for copper

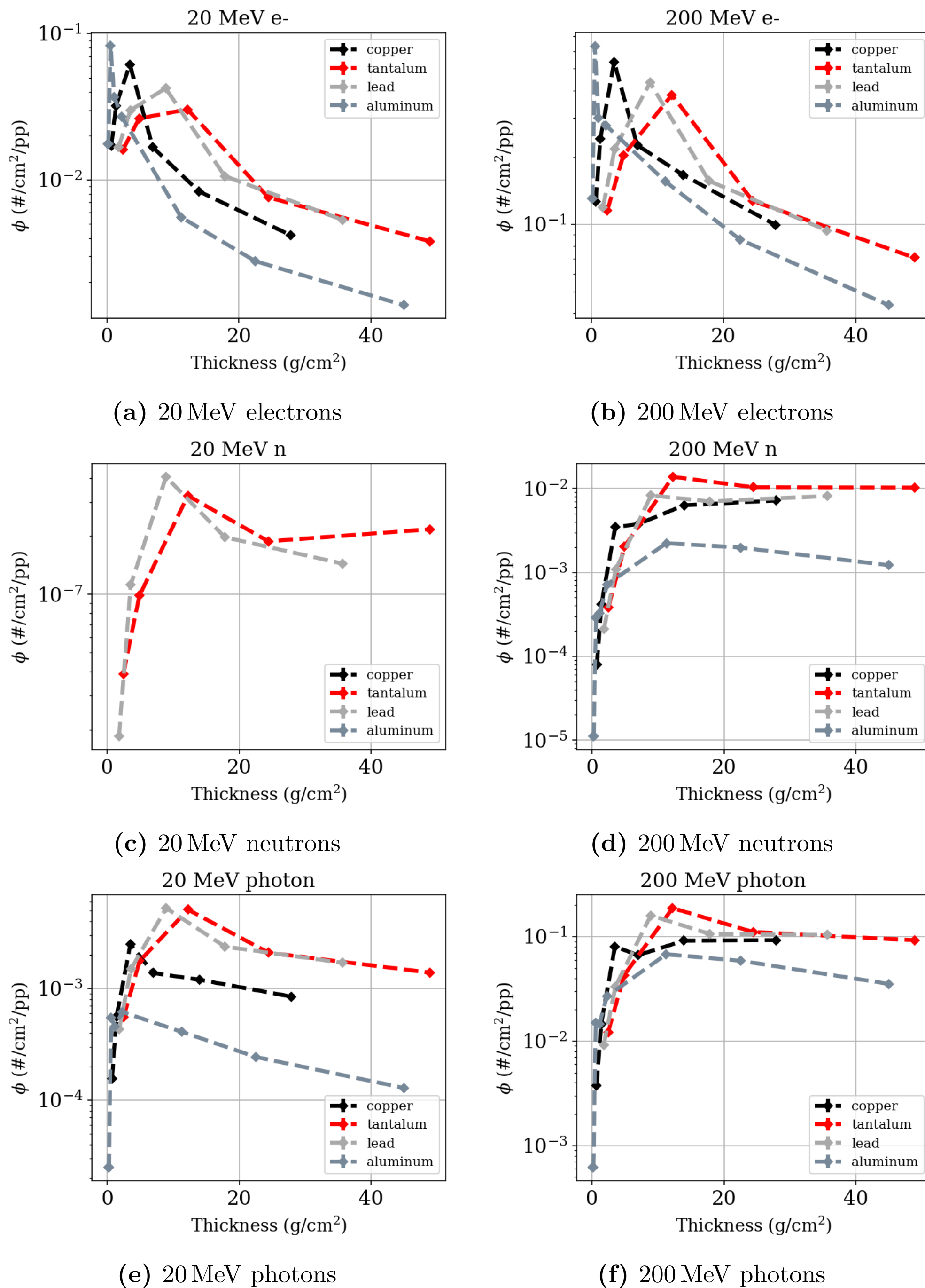

(a) 20 MeV electrons

(b) 200 MeV electrons

(c) 20 MeV neutrons

(d) 200 MeV neutrons

(e) 20 MeV photons

(f) 200 MeV photons

Figure 5.23: Integrated flux over 10 MeV to beam energy over the secondary particles created by a 200 MeV electron beam passing through various thicknesses of shielding materials

and aluminium, a saturation cross-section as a function of depth is reached already at relatively small shielding thicknesses.

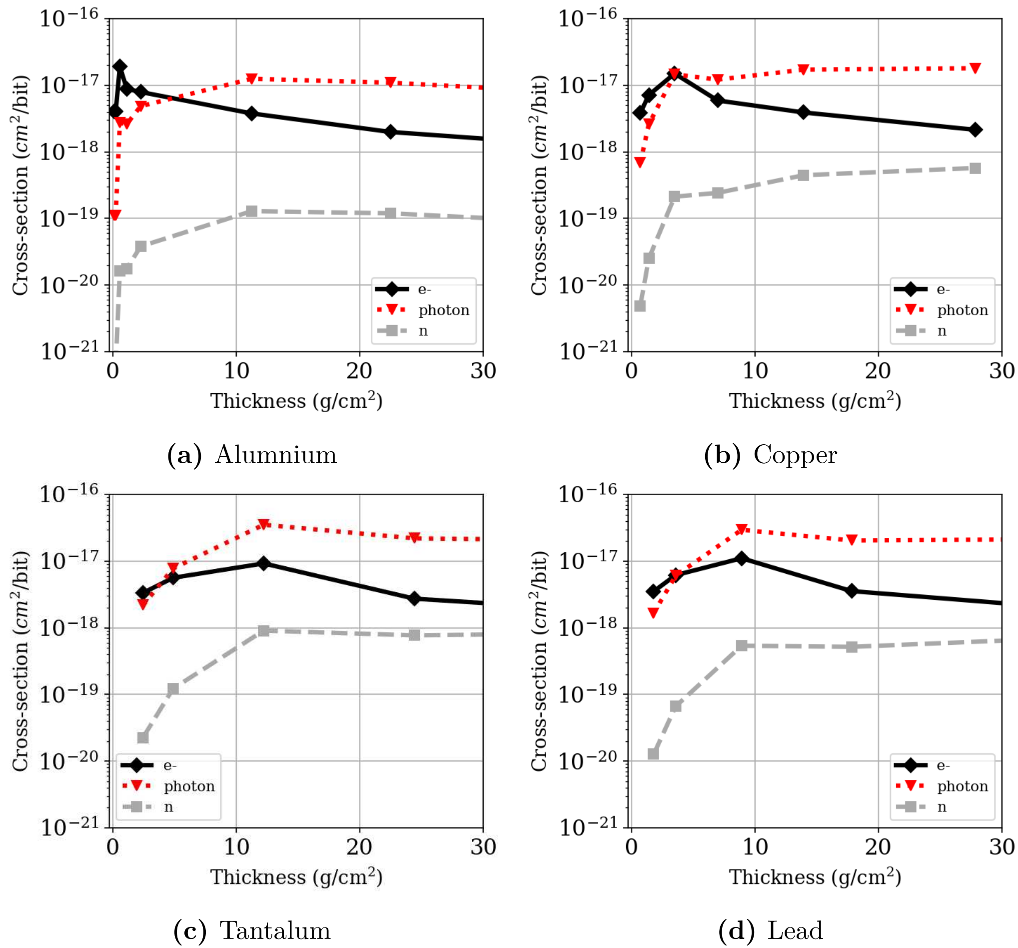

(a) Alumnium **(b)** Copper

(c) Tantalum **(d)** Lead

Figure 5.24: The cross-section of the folding between the ESA SEU monitor Weibull estimates and the flux of secondaries generated by a 200 MeV beam of electrons. Secondary electrons, neutrons, electrons or photons generated in the shielding materials are used for the analysis

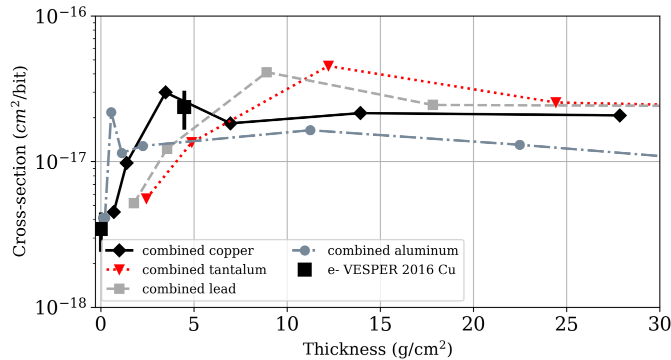

Figure 5.25: SEU cross-section contribution for secondary electrons, neutrons and photons produced by a 200 MeV electron beam transported through common shielding materials for the ESA SEU monitor. The black squares represent the experimental points of the irradiations performed at VESPER [2].

6 Electron Single Event Upsets Testing

The electron-single event testing included in this thesis work was mainly conducted in the VESPER facility at CERN and the electron linac at the RADEF facility in Jyväskylä, Finland, described in chapter 4. The experimental work was described in detail in [1] and [2].

The devices that were tested for electron-induced single-event upsets were the ESA SEU monitor and the Artix-7 based FPGA Arty. The ESA SEU monitor is a good candidate for these tests because it is a relatively large technology (250 nm) and has a high critical charge of about 10 fC. Due to the high critical charge, some of the alternative mechanisms that could be causing the upsets are ruled out as discussed in more detail in chapter 9. The Arty was chosen as it is a more integrated technology (28 nm).

6.1 ESA SEU Monitor Electron Irradiation Results

6.1.1 RADEF results

The ESA SEU monitor was tested with 20 MeV, 16 MeV and 12 MeV electrons at the electron linac at the RADEF facility. The beam flux was varied to rule out the pile-up effect, as described in [1]. The test was performed in static conditions: the device was programmed, the desired fluence was delivered to the device, and the errors were read out after the irradiation. SEUs were detected at the 20 MeV and 16 MeV energies. No upsets were recorded at 12 MeV in the available beam time, so therefore the cross-section for this energy is below the threshold. The results can be seen in Table 6.1 and in [2]. A detailed description of the conversion from dose to fluence is given in [2].

RADEF linac				
Energy (MeV)	**Avg. Dose rate (rad/min)**	**Total Dose (krad)**	**SEUs**	**Cross section (cm^2/bit)**
20.0	1.00×10^3	160	115	1.17×10^{-18}
20.0	3.00×10^2	13.3	10	1.14×10^{-18}
20.0	1.00×10^2	6	5	1.36×10^{-18}
16.0	1.00×10^3	60	2	5.44×10^{-20}
12.0	1.00×10^3	10	0	$*1.63 \times 10^{-19}$
VESPER linac				
Energy (MeV)	**Duration(h)**	**Fluence (e-/cm^2)**	**SEUs**	**Cross section (cm^2/bit)**
VESPER 2017				
62	19.0	1.39×10^{13}	277	2.45×10^{-18}
60	58.0	1.79×10^{14}	2974	2.08×10^{-18}
115	17.0	1.39×10^{13}	374	3.33×10^{-18}
175	7.9	1.16×10^{13}	579	6.17×10^{-18}
175	11.8	1.72×10^{13}	653	4.67×10^{-18}
VESPER 2016				
133	15.1	3.95×10^{12}	81	1.87×10^{-18}
133	14.8	4.20×10^{12}	141	3.42×10^{-18}
170	8.1	3.01×10^{12}	143	4.29×10^{-18}
170	13.9	5.09×10^{12}	169	2.88×10^{-18}
206	16.0	2.60×10^{13}	1558	5.97×10^{-18}
206	7.5	5.30×10^{12}	283	5.09×10^{-18}
206	16.0	1.04×10^{13}	545	4.68×10^{-18}

Table 6.1: ESA SEU monitor electron irradiation results at the RADEF and VESPER linac, *an upper bound (the inverse of fluence) has been given for the 12 MeV irradiation. For the VESPER linac runs which have been grouped together for the Weibull fit are shown with brackets [2].

6.1.2 VESPER results

SEU measurements at VESPER are a collection of measurements collected at VESPER and described in detail in [1, 2]. The measurements range from 60 MeV to 200 MeV. The VESPER facility is described in detail in section 4. Due to the high fluxes that can be reached at the facility, a high number of SEUs could be gathered despite the low cross-section for the electron-induced SEUs. In addition, measurements were performed with varying beam charge (or electron flux per pulse), rule out the pile-up effect and with the addition of shielding material slabs for experimental results for the shielding material simulations described in chapter 5 [1, 2]. The results are shown in Table 6.1.

6.1.3 Experimental Weibull fit for the ESA SEU monitor

The electron irradiation campaigns performed in VESPER as a part of [1] and [2], form a complete set of SEU cross-section measurements. The relevant experimental points and the Weibull fit can be seen in Fig. 6.1. The exact fit parameters can be seen in Table 6.2 [2].

Parameter	Value
XSsat	$3.84 \times 10^{-18}\,\mathrm{cm^2/bit}$
Lo	16.0 MeV
W	45.3 MeV
s	0.62

Table 6.2: The total electron-induced SEU cross-section Weibull fit for the ESA SEU monitor [2].

As the electrons in the beamline interact with the beamline elements, such as the BTV screen or the beam exit window, other particles are created through these interactions. It was shown in [1] that the amount of neutrons generated is not enough to affect the final cross-section. However, due to a large number of photons created through electrons passing through matter, the increase is more likely, as discussed in chapter 5. A FLUKA simulation with various shielding materials was performed to investigate this in further detail. The results of the simulations are shown in detail in chapter 5. Irradiations were performed with and without a 1 cm aluminium slab placed directly in front of the ESA SEU monitor to verify the increase predicted by the FLUKA simulation [2]. Previously, some irradiations with a copper slab were performed as well [1].

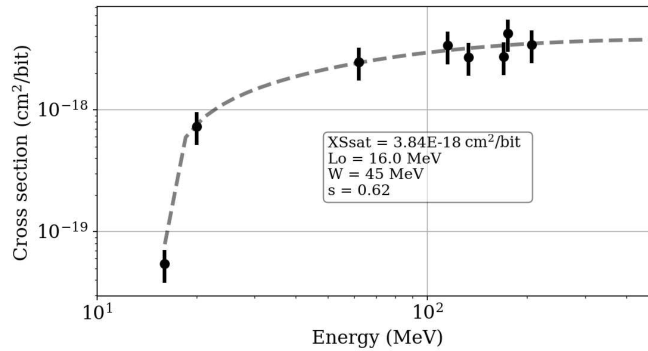

Figure 6.1: The Weibull fit for electron induced SEU for the ESA SEU monitor based on measurements from the VESPER and the RADEF facility [2].

The resulting cross-section at 175 MeV was 3.26×10^{-17} cm^2/bit, and 5.26×10^{-18} cm^2/bit without the aluminium slab, the cross-section with the added material is then about six times higher. The irradiation results confirm the simulations presented in chapter 5, showing that even this thicknesses of shielding materials increase the SEU cross-section

and that the increase is caused by the photons generated by electrons passing through matter [2].

In addition, due to the increased flux, the presence of a pile-up effect had been experimentally ruled out. Consequently, two measurements were performed at the same beam energy but different beam charges: 9 pC and 2 pC. As shown by [17] and discussed in chapter 9, if prompt dose effects indeed caused the upsets, the cross-section would vary exponentially with the increase of intensity. The measured cross-section for 9 pC is 3.22×10^{-17} cm^2/bit and for 2 pC the cross-section was 3.07×10^{-17}cm^2/bit. The difference between the two results is 5% and therefore within statistical uncertainties. Since the cross-section does not vary exponentially with the varying pulse intensity, we can conclude that the upsets were not due to the pile-up effect [1, 2].

6.2 Artix-7 BRAM Electron Irradiation Results

The Artix-7 was irradiated both at the RADEF facility with intermediate-energy electrons and at the VESPER facility with high-energy electrons.

The RADEF facility irradiations were performed at the maximum available beam energy of 20 MeV and the dose rate used was 100 krad s^{-1}(H_2O). Only two upsets were observed in the BRAM, and the measured cross-section was 3.81×10^{-19} cm^2/bit [2].

The VESPER irradiations were performed at 60 MeV and 200 MeV, the resulting cross-sections were reported as 2.01×10^{-17} cm^2/bit and 4.76×10^{-17} cm^2/bit in [2] respectively. However subsequently an offset was believed to appear in the calibration of the flux measurement for these results due to an error in the calibration procedure. Therefore, the measurements were repeated with the correct calibration procedure. The new irradiations were performed at 70 MeV, 140 MeV and 200 MeV, the resulting cross-sections were measured as 1.46×10^{-18} cm^2/bit, 4.08×10^{-18} cm^2/bit and 4.92×10^{-18} cm^2/bit. The new measurement results at VESPER in addition to the RADEF results are shown in Table 6.3. The repeated measurements confirm the original offset in the facility calibration and prove that the electron cross-section is similar for devices with different device technologies, such as the ESA SEU monitor and the Artix-7, as was expected.

6.2.1 Experimental electron Weibull fit for the Artix-7 BRAM

A FLUKA energy deposition simulation was performed to estimate the SEU cross-section of the Artix-7. The simulation is very similar to the ESA SEU monitor simulations described in chapter 5. To adjust the geometry in the FLUKA simulation to the Artix-7 (28 nm) from the ESA SEU monitor (250 nm) a sensitive volume size of 0.3 µm × 0.3 µm × 0.5 µm was chosen as an estimate. The proton energy deposition curve was used to find a critical

RADEF Electron				
Energy (MeV)	**Dose rate (rad/min)**	**Total Dose (krad)**	**SEUs**	**Cross section (cm^2/bit)**
20.0	1.00×10^2	100	2	3.81×10^{-19}
VESPER 2019				
Energy (MeV)	**Duration(min)**	**Fluence (e-/cm^2)**	**SEUs**	**Cross section (cm^2/bit)**
71	46	2.4×10^{12}	5	1.46×10^{-18}
142	1.8	1.7×10^{12}	10	4.08×10^{-18}
200	130	3.8×10^{12}	27	4.92×10^{-18}

Table 6.3: Artix-7 irradiation results at the electron lines at RADEF and the VESPER facility. fields marked with * are the upper bounds for the cross sections

charge for the Artix-7 to cross-check if the estimate was accurate. For this an experimental SEU measurement performed in [75] was used, the reported saturation cross-section is 9×10^{-15} cm^2/bit. A critical charge of 3.7 fC was found using the experimental proton cross-section on the proton energy deposition curve. An estimation of the electron SEU cross-section was found as 4×10^{-18} cm^2/bit at 200 MeV using this same critical charge. The procedure is shown in Fig. 6.2, where both the proton and electron energy deposition curves are visible.

The estimation for the Artix-7 SEU cross-section is similar to the experimental saturation cross-section of 6×10^{-18} cm^2/bit, which is the result one would expect in case of indirect energy deposition as the dominating mechanism. It has been shown that the cross-section should remain constant with the change of technology node because although the cross-section is higher for devices from smaller critical charges, the sensitive volume size is smaller. Therefore, we can assume that if the cross-section remains constant, one can expect that the mechanism responsible for inducing the SEU in the device is the same. As was discussed in detail in section 5, the mechanism is believed to be electro- and photo-nuclear reaction in or near the sensitive volumes. The experimental and simulation results confirm that the electron-induced SEU cross-section remains comparable across very different technology nodes. As explained in [31], given that the critical charge of a device is low enough, additional effects such as the Rutherford scattering can become the dominating mechanism for the electron-induced SEU. However, in this case, the device would also be expected to be sensitive to direct ionization by low-energy particles, such as electrons and protons. This is not the case for the Artix-7 BRAM, as shown with experimental results in chapter 8 and therefore, nuclear interactions can be considered as the underlying mechanisms of high-energy SEU induction also for the studies 28 nm technology node.

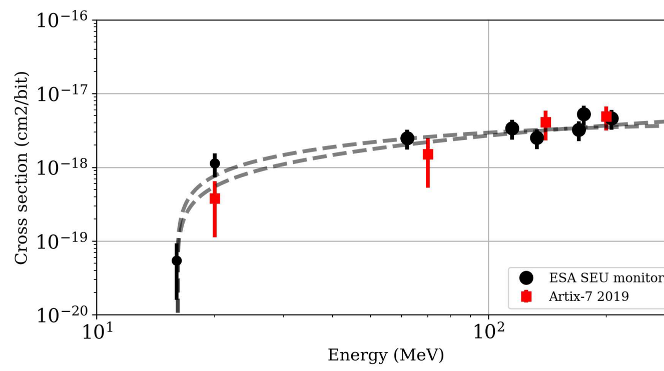

Figure 6.2: The Weibull fit for electron induced SEU for the Artix-7 and the ESA SEU monitor

7 Electron Single-Event Latchup Testing

As shown in chapter 5, electrons are capable of producing fission fragments in silicon with LET values up to 13 MeV cm^2/mg, which is similar to the highest LET fragments generated by protons at 13 MeV cm^2/mg. Although the LET values are similar, the fragments are created at a much lower rate through electron interactions due to their lower nuclear interaction cross-section, as shown in chapter 5. Therefore, devices that are sensitive to proton-induced destructive events such as the latch-up should in theory also be sensitive to electron-induced events given that their sensitivity is low enough. As the cross-section of the fragment generation is lower, in theory also the cross-section should be smaller. To test this theory, three SRAM memories, described in more detail in section 4 from ISSI, Alliance and Brilliance manufacturers, were tested at the VESPER electron beam facility. All of the memories have a relatively high onset LET value, and should, therefore, be sensitive only to mechanisms requiring a large amount of deposited energy, such as the nuclear reaction, similar to the single-event upsets shown in section 6. During the testing at the VESPER facility, a calibration error of the FBCT lead to a systematic offset of the results due to an error in the calibration software. Although the absolute cross-section of the SEL measurements performed at the facility have a larger uncertainty in the dosimetry as first assumed, the experimental results still confirm that electrons can induce SEL in the SRAM memories. The memories have been previously characterized with both protons, and heavy ions and their experimental heavy-ion Weibull fits can be seen in Table 7.1.

Memory	**XSsat (cm^2)**	**Lo (MeV cm^2/mg)**	**$L_{1\%}$ (MeV cm^2/mg)**	**W (MeV cm^2/mg)**	**s**
ISSI	0.24	2.1	6.5	16.8	3.4
Alliance	0.13	0*(<5)	15	27.6	7.4
Brilliance	0.60	2.4	3.7	13.7	1.8

Table 7.1: A summary of the Weibull parameters of the SEL-sensitive SRAM memories tested at VESPER [3]

7.1 Brilliance Experimental Results

The Brilliance memory was tested with 160 MeV and 215 MeV electrons at the VESPER facility. The LET threshold for this memory is 2.4 MeV cm^2/mg, so it is expected to be sensitive to silicon fission fragments generated through the nuclear interactions of electrons with silicon near the sensitive volumes, as described in section 5. The memory was found to be sensitive to electron-induced SEL, and the experimental cross-sections are shown in Table 7.2. As the Brilliance memory has the highest saturation cross-section of the three tested memories for the heavy ions irradiations, the cross-section is expected to be the highest for electrons as well, which was also measured experimentally. The memory is shown to have a cross-section which is ~ 3 times higher at 215 MeV than for the second most sensitive memory, the ISSI.

Shown later in this chapter, since the electron-induced SEL cross-section is very low, the devices start to suffer from the increase of the standby current due to the deposited dose. Therefore, the number of SEL is limited by the dose and the statistics obtained in the measurement have some statistical uncertainty [3].

Energy (MeV)	Beam Charge (pC)	Beam size x (mm)	Beam size y (mm)	Total time (min)	Recorded SELs	cross-section (cm^2/Device)
160	11	12	13	25	26	6.14×10^{-11}
215	11	15	12	360	84	1.34×10^{-10}

Table 7.2: Brilliance SRAM memory irradiation results at VESPER

7.2 ISSI Experimental Results

The ISSI memory was irradiated at 60 MeV, 160 MeV and 215 MeV. It has a LET threshold of 2.1 MeV cm^2/mg and a heavy ion saturation cross-section of 0.24 cm^2, which is about factor 3 less than for the Brilliance memory. Therefore, the expected electron-induced SEL cross-section is expected to be similarly lower. Due to the low LET threshold, the cross-section is also likely to be dominated by the silicon nuclear interaction products. The experimental results show that the cross-section has an energy dependence. This energy dependence was also observed for protons in [67], and therefore fits well with the assumption that the events are induced by nuclear interactions, analogous to the proton case. Due to only a few counts at lower energies, the energy dependence cannot be confirmed, and higher statistics would be needed to validate this dependence experimentally. The irradiation results can be seen in Table 7.3[3].

Measurements at different beam charges were performed additionally to rule out events caused by more than one electron depositing charge in the same sensitive volume and the cumulative charge being responsible for the events. The measurements were performed at 210 MeV. The cross-section was measured as $(3.2^{+5.9}_{-1.0}) \times 10^{-11}$ cm^2 for 3.5 pC and as $(1.76^{+3.83}_{-0.65}) \times 10^{-11}$ cm^2 for 15 pC. The upper and lower bounds are given with a 95% confidence bounds. Due to the small number of counts the uncertainty is therefore limited by the number of errors, rather than the dosimetry of the facility. However, the difference between the cross-section is compatible with the statistical uncertainty and what is more, the average cross-section value for the lower beam charge is higher, further confirming that this is not a pile-up effect. Since a cumulative effect would mean an exponential increase in cross-section as shown in [16] it can be ruled out [3].

Energy (MeV)	Beam Charge (pC)	Beam size x (mm)	Beam size y (mm)	Total time (min)	Recorded SELs	Cross-section (cm^2/Device)
60	12	24	15	31	0	2.91×10^{-12}*
155	11	19	20	51	8	1.42×10^{-11}
160	12	13	13	30	5	9.84×10^{-12}
210	3.5	15	24	105	13	3.20×10^{-11}
210	4	15	24	50	6	2.72×10^{-11}
210	4	15	24	27	4	3.35×10^{-11}
215	15	12	13	196	6	1.76×10^{-11}

Table 7.3: ISSI SRAM memory irradiation results at VESPER, *an upper bound has been given for the 60 MeV irradiation [3]

7.3 Alliance Experimental Results

Since no LET threshold was experimentally found for the Alliance memory, the $L_{1\%}$ is used instead and it is given as 15 MeV cm^2/mg [74]. This threshold value is higher than for the other two memories and also higher than the nuclear reaction products induced by electrons in silicon of 13 MeV cm^2/mg; one would expect a very low count rate or no events at all for this memory. The events that would be recorded would be expected to be induced by the tungsten fission fragments, which have a much lower cross-section compared to the silicon products.

As shown experimentally, no events were recorded in this memory. Instead, a dose induced current increase was noted in the memories before any events could be recorded. The current increase is explained in more detail in the following section. The irradiation results are shown in Table 7.4[3].

Energy (MeV)	Beam Charge (pC)	Beam size x (mm)	Beam size y (mm)	Total time (min)	Recorded SELs	Cross-section (cm^2/Device)
60	16.6	24	15	296	0	1.83×10^{-12}*
155	10	18	20	50	0	7.98×10^{-13}*
210	11	15	24	110	0	2.35×10^{-12}*

Table 7.4: Alliance SRAM memory irradiation results at VESPER, *an upper bound has been given for the irradiations as no SEL was observed during the tests [3]

7.4 TID Effects Observed During SEL Testing

As explained in the previous sections, the electron-induced SEL cross-section is low. Due to this, the devices under test receive a relatively large fluence and dose before experiencing a meaningful number of SEL. After a certain amount of time, an increase of the standby current of the memories tested could be observed as seen in Fig 7.1. This increase was attributed to the deposited dose. Due to the rise of the standby current possibly changing the SEL cross-section, all of the events recorded after the current increase were not included in the final analysis [3].

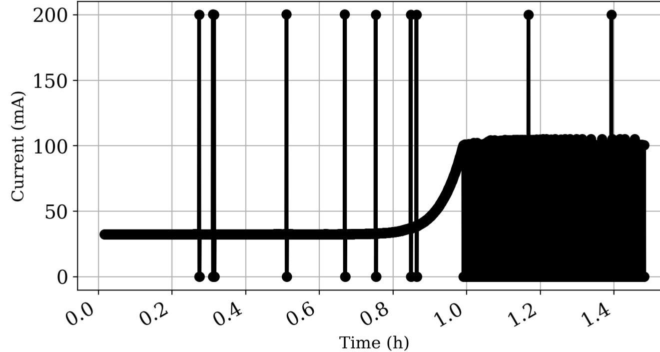

Figure 7.1: An example of the current readout during the irradiation of the ISSI memory, SEL detection threshold was set to 100 mA, therefore the device entered an endless reset loop. All of the events recorded after the current increase were not included in the final analysis [3].

To experimentally test whether the cumulative dose caused the increase in standby current, an irradiation was performed in a Co-60 facility at ESTEC in the Netherlands. All of the three memories were biased to the nominal 3.3 V and the current consumption of each memory was monitored during gamma exposure. For the Brilliance memory, the CE and the $\overline{CE}$ pin were connected according to specification so that the memory was turned off [3].

The increase in the standby current consumption of each memory plotted against the dose can be seen in Fig. 7.2. All three of the memories displayed an increase in standby current

characteristic of a TID test. The current increase began after 270 Gy for the Brilliance, after 330 Gy for the ISSI and after 550 Gy for the Alliance memory. The memories that were more sensitive to the dose also had a higher SEL cross-section, as was expected. It can be concluded from the test that for electron-induced SEL testing of the memories the lower sensitive memories will most likely fail due to the deposited dose before experiencing any latch-up events [3].

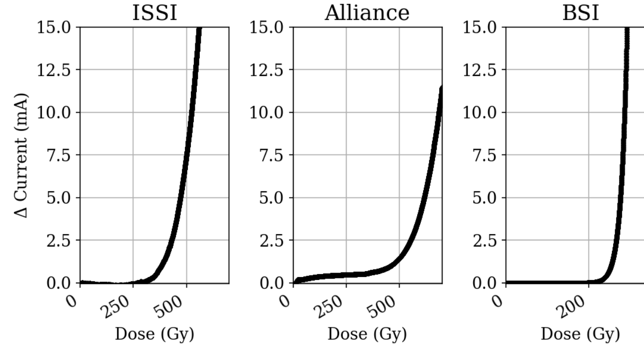

Figure 7.2: The relative standby current for each of the three memories plotted against the dose at the Co-60 facility at ESTEC [3] IEEE®.

7.5 FLUKA Estimation of the SEL Cross-Sections

A comparison was performed with the simulated cross-section values, obtained through a FLUKA energy deposition simulation folding, to put the experimental results into context, described as follows.

The experimental heavy-ion Weibull fits of the three memories were plotted against the LET, as can be seen in Fig. 7.3, to get a first estimate of the expected sensitivities of the memories to the electron-induced SEL. The region of interest for estimating the events is the region where the highest nuclear interaction products of electrons and silicon, which is 13 MeV cm^2/mg. The same value for protons is 15 MeV cm^2/mg, the area between these two numbers is shaded. As can be seen, the cross-sections for these memories are quite different in this region with the Brilliance memory being most sensitive, the ISSI memory having a sensitivity which is about two times lower and the Alliance memory being an order of magnitude less sensitive than the Brilliance memory. The experimental results correspond well with this first estimation [3].

The general outline of the procedure is described in more detail in [67] and chapter 5. In short, the experimental heavy ion cross-sections are measured at different LET values, and a Weibull fit is found for the results. The resulting Weibull fit is then folded with the simulated particle spectra for the facility. The simulation for the particle spectra and the folding procedure are described in more detail in chapter 5. This procedure results in

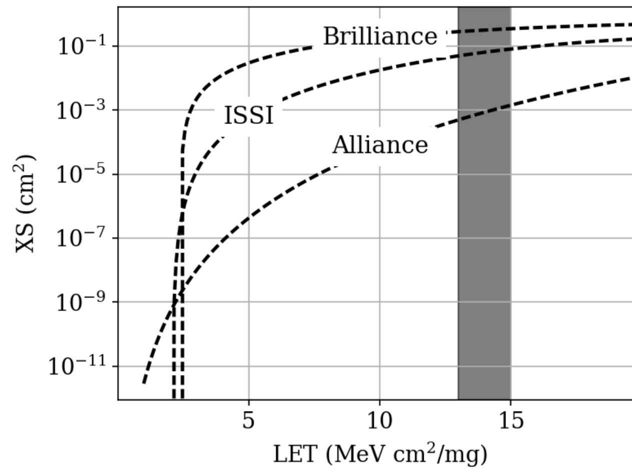

Figure 7.3: The heavy-ion Weibull functions of the tested SRAM. The shaded area represents the highest LET of recoils generated by electrons and protons and illustrates the difference in the cross-section in this region [3] IEEE®.

an estimated SEL cross-sections for all simulated particles. The experimental heavy-ion Weibull fit has been found in [67, 74] and can also be seen in Table 7.1 [3].

The electron-induced SEL cross-sections for Brilliance, ISSI and Alliance can be seen in Fig. 7.4, Fig. 7.5 and Fig.7.6. The IRPP model for the SRAMs for the FLUKA simulations for this work was based on the model in [74] for protons. Since a representative thickness was chosen as common for all memories and not explicitly fitted for each, the fit of the cross-sections and the experimental work is representative of the magnitude of the cross-section and meant as a first proof of concept.

The simulated SEL cross-section estimate has a good fit to the experimental measurements of the Brilliance SRAM. The simulated energy dependence is also visible on the experimental results and corresponds well to the energy dependence introduced by the inelastic interaction cross-section described in chapter 5. This strengthens the theory that nuclear interactions induced the events [3].

The experimental measurements of the ISSI SRAM also display an energy dependence of the cross-section, which would indicate nuclear events being responsible for inducing events. However, the absolute difference between the FLUKA estimation and the experimental results is about a factor 4. The difference can be explained by the choice of the SV geometry not being fitted individually for each memory, but the same geometry was used for all three as a first proof [3].

The experimental measurements of the Alliance SRAM were performed at three different energies, however no events were recorded in any of the irradiations due to the fact that (I) the Alliance memory is the least sensitive of the three, with an onset LET value of

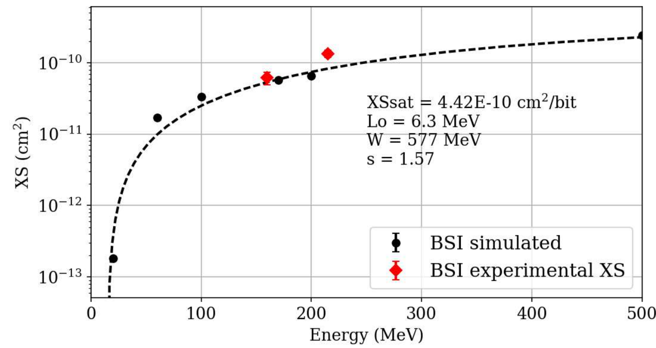

Figure 7.4: The simulated SEL cross-section for Brilliance [3] IEEE®

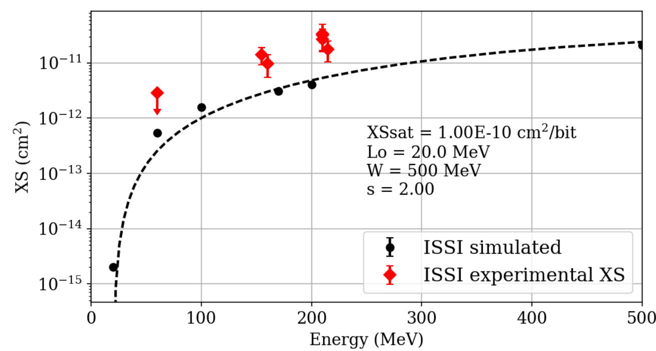

Figure 7.5: The simulated SEL cross-section for ISSI [3] IEEE®

15 MeV cm^2/mg, and a considerable test time would be needed to reach the required fluence. (II) The standby current of the memory increased a lot over the specifications, and the SEL measurements could not be deemed trustworthy, this phenomenon is described more in section 7.4. As a result, only upper limit values, which are given as the inverse of the fluence, are shown [3].

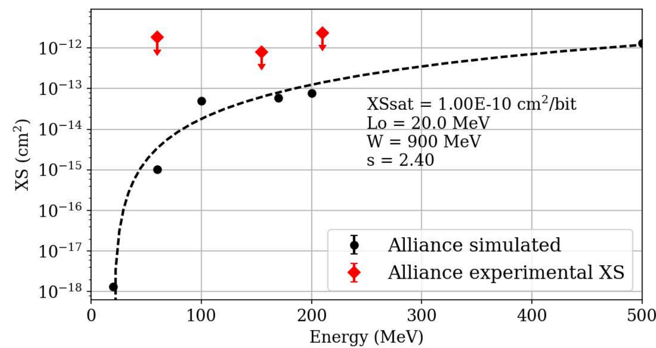

Figure 7.6: The simulated SEL cross-section for Alliance [3] IEEE®

8 Low-Energy Proton Testing

In this chapter, the low-energy proton sensitivity of the 28 nm Artix-7 based FPGA Arty and the 90 nm SRAM memories by Cypress, referred to as Cypress A for the CY62167EV30LL-45ZXA and Cypress B for the CY62157EV30LL-45ZSXI, and the 65 nm IS6164WV204816BLL by ISSI, both described in chapter 4, are discussed. The irradiations of both were performed at the RADEF facility in Jyväskylä, Finland. In addition, to fully characterizing the SRAM memories, additional heavy-ion irradiations at the RADEF facility were performed. Whereas the Arty does not display any sensitivity for low-energy protons, the SRAM memories show high sensitivity. Finally, the contribution that low-energy protons, and by extension electrons, have in the mixed-field environment at the CHARM facility is discussed. In addition, irradiations with boron carbide slabs were performed on the memories to estimate the contribution thermal neutrons have on the response rate of highly-integrated technologies in a mixed field.

8.1 Heavy Ion Testing of SRAM Memories

The heavy ion testing was performed in vacuum at the heavy ion line at the RADEF facility in Jyväskylä, Finland. The heavy ion facility is described in detail in section 4.3. The experimental setup was placed in vacuum to minimize the energy loss of the heavy ions in air. The memories were tested using the CERN SEU tester described in section 4.5.4. The memories were biased to the nominal 3.3 V. The power supply was additionally monitoring the current consumption of the memories and was set up to perform a reset in case of an SEL event, the results in such an event during a run were disregarded. The memories were tested in static mode - a checkerboard pattern was written to the memories before the irradiation, the memories received the fluence described in the results in Table 8.1, and were read after the irradiation, and the number of upsets was noted.

The results of the heavy ion testing were used to find an experimental heavy ion Weibull fit for the two memories. The results of fitting the experimental results to a Weibull curve can be seen in Table 8.2 and a visualization of the experimental results together with the Weibull curves can be seen in Fig. 8.1.

Component	Ion	LET (MeV cm^2/mg)	Energy (MeV)	Fluence (ions/cm^2)	SEU	Cross-Section (cm^2/bit)
Cypress A	15N	1.83	139.0	1.514E+05	930	3.613E-10
Cypress A	20Ne	3.68	523.0	1.705E+04	595	2.053E-09
Cypress A	40Ar	10.10	523.0	6.080E+03	705	6.821E-09
Cypress A	56Fe	18.50	523.0	3.520E+03	523	8.740E-09
Cypress A	82Kr	32.10	768.0	2.000E+03	557	1.638E-08
Cypress A	131Xe	60.00	1217.0	9.200E+02	670	4.284E-08
ISSI	15N	1.83	139.0	4.090E+04	605	4.351E-10
ISSI	20Ne	3.68	523.0	3.528E+04	994	8.287E-10
ISSI	40Ar	10.10	523.0	9.070E+03	566	1.835E-09
ISSI	56Fe	18.50	523.0	6.030E+03	743	3.624E-09
ISSI	82Kr	32.10	768.0	4.030E+03	803	5.860E-09
ISSI	131Xe	60.00	1217.0	2.010E+03	653	9.555E-09

Table 8.1: The results of the heavy ion irradiation of the ISSI and Cypress A memories at the RADEF facility. The fluence and the SEU are averaged to show the final cross-section calculation values

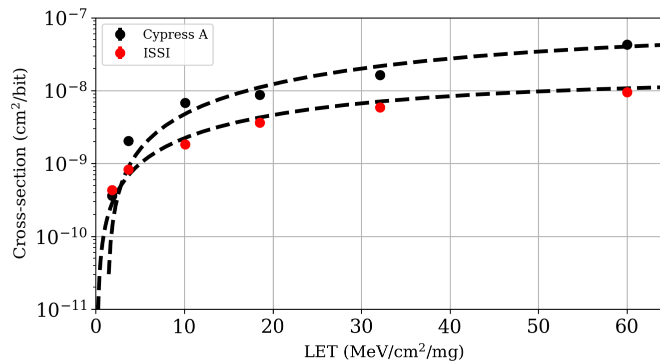

Figure 8.1: Results of the heavy ion irradiations and the Weibull fits for each device

Component	XSsat (cm^2/bit)	Lo (MeV/cm^2/mg)	W (MeV/cm^2/mg)	s
Cypress A	6.68E-08	1.27	62.28	1.33
ISSI	1.16E-08	0.20	40.00	1.20

Table 8.2: The experimental heavy ion Weibull fits for the memories.

8.2 Proton Testing of the SRAM Memories

The proton testing was performed at the low-energy proton line in vacuum for proton energies up to 5 MeV and at the high-energy proton line in air for energies higher than 5 MeV. The memories tested were ISSI 65 nm and the Cypress A SRAM memory described in section 4.5.4.

The memories were attached to the CERN SEU tester described in section 4.18. The two memories were tested in turn, and for the low-energy proton testing, the memories were also tilted at a 45° and 60° angles to estimate the angular dependency of the memories. In general, for angle testing the effective LET of the particle changes according to the cosine law described as

$$LET_{eff} = \frac{LET}{\cos\alpha} \tag{8.1}$$

where α is the tilt angle and LET_{eff} the effective LET of the particle. The RADEF facility provides the fluence, which already takes into account the angle as well as the effective number of particles decrease also following the cosine law.

The memories were programmed to a checkerboard pattern, and the static test was performed, meaning that the memories were written before the irradiation, the desired fluence of protons was delivered to the memory, and the memory was read out again, and the number of upsets was noted. The results of the simulation can be seen in Table 8.3 for the Cypress A memory and Table 8.4 for the ISSI.

The results of the low-energy (LE) proton testing show clearly that both the Cypress A and the ISSI memories are highly sensitive to direct ionization by protons. To evaluate if the upsets in the SRAM were caused by single protons or by cumulative charge deposited by more than one proton, the probability of two or more proton hitting the same cell during the relaxation time of a previous upset can be calculated as [17]

$$Pr(X_1||X_2) = (\phi A_{cell}\tau)^2 \tag{8.2}$$

where ϕ is the incident flux at the RADEF facility, A_{cell} is the size of the sensitive area, estimated to $1\,\mu m^2$ for both SRAM, and τ is the relaxation or response time for an upset event. As described in [17], the most appropriate time for the SRAM memories technology size would be 10 ns. The probability is then. $(1 \times 10^6\,p/cm/s \cdot 1\,\mu m^2 \cdot 10\,ns)^2 = 1 \times 10^{-16}$, which implies that the probability that these events are caused by a cumulative effect is negligible.

The comparison between the different components shows that the ISSI is more sensitive, as also proved by the heavy ion testing and the cross-section increase starts already below ~ 5 MeV. The Cypress A memory is slightly less sensitive, and the increase in cross-section is apparent at around ~ 1 MeV. The comparison between the different angles can be seen in Fig. 8.2.

Comparing the same component but at different angles, as seen in Fig. 8.3 reveals that the change in the tilting angle pushes the increase in cross-section to higher energies. This means that the effective LET of the particles increases, as predicted by the cosine law described in Eq. 8.1.

Energy (MeV)	Fluence (p/cm^2)	Tilt (Degrees)	Cross-Section (cm^2/bit)	Error (cm^2/bit)
0.6	1.400E+07	0	1.909E-11	5.698E-13
0.6	3.000E+06	45	6.746E-12	7.317E-13
0.6	3.010E+06	60	3.560E-13	1.678E-13
0.8	5.020E+08	0	1.632E-13	8.797E-15
0.8	5.000E+07	45	5.274E-13	5.011E-14
0.8	5.100E+07	60	5.497E-13	5.066E-14
1.0	1.010E+09	0	5.717E-15	1.161E-15
1.0	1.010E+09	45	9.488E-15	1.496E-15
1.0	5.070E+08	60	4.274E-14	4.480E-15
2.0	4.661E+09	0	2.363E-15	3.474E-16
2.0	1.040E+09	45	3.205E-15	8.566E-16
2.0	1.010E+09	60	3.654E-15	9.281E-16
3.0	4.050E+09	0	4.365E-15	5.066E-16
3.0	1.000E+09	45	4.286E-15	1.010E-15
3.0	1.000E+09	60	7.798E-15	1.363E-15
6.0	4.542E+09	0	6.330E-15	5.760E-16
6.0	3.020E+09	45	7.667E-15	7.775E-16
6.0	2.010E+09	60	9.861E-15	1.081E-15
12.5	1.620E+09	0	9.333E-15	1.171E-15
21.5	9.220E+08	0	1.750E-14	2.126E-15
30.0	1.214E+09	0	1.863E-14	1.912E-15
40.0	8.380E+08	0	2.245E-14	2.525E-15
53.0	1.559E+09	0	1.910E-14	1.708E-15

Table 8.3: The results of the proton irradiation of the 90 nm Cypress A memory at the RADEF facility

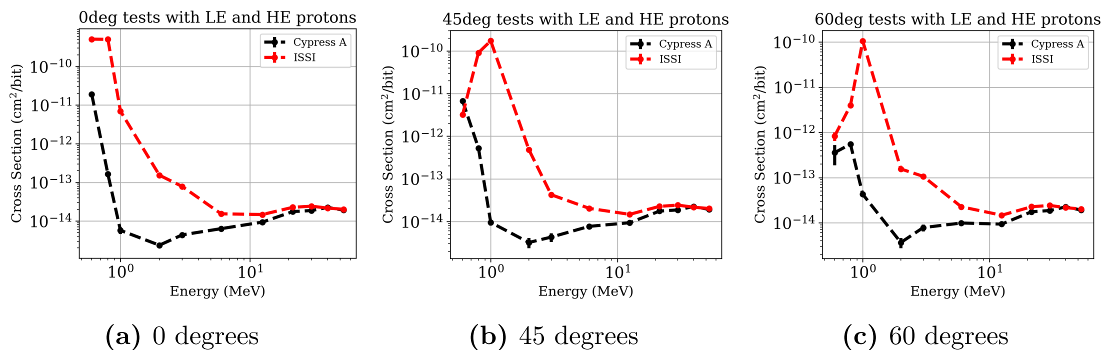

(a) 0 degrees **(b)** 45 degrees **(c)** 60 degrees

Figure 8.2: The comparison between different tilting angles from the proton testing of Cypress A and ISSI memories

Energy (MeV)	Fluence (p/cm^2)	Tilt (Degrees)	Cross-Section (cm^2)	Error
0.6	5.270E+06	0	5.082E-10	3.388E-12
0.6	4.250E+06	45	3.228E-12	3.007E-13
0.6	3.020E+06	60	8.278E-13	1.806E-13
0.8	1.070E+08	0	5.021E-10	7.474E-13
0.8	1.000E+06	45	9.113E-11	3.294E-12
0.8	4.010E+06	60	3.948E-12	3.424E-13
1.0	6.000E+08	0	6.981E-12	3.722E-14
1.0	6.556E+07	45	1.730E-10	5.605E-13
1.0	1.716E+07	60	1.056E-10	8.559E-13
2.0	5.120E+08	0	1.531E-13	5.967E-15
2.0	5.060E+08	45	4.848E-13	1.068E-14
2.0	1.000E+08	60	1.551E-13	1.359E-14
3.0	3.254E+09	0	7.832E-14	1.693E-15
3.0	5.090E+08	45	4.239E-14	3.149E-15
3.0	5.060E+08	60	1.063E-13	5.002E-15
6.0	8.750E+08	0	1.534E-14	1.445E-15
6.0	5.190E+08	45	2.024E-14	2.155E-15
6.0	5.110E+08	60	2.254E-14	2.292E-15
12.5	7.730E+08	0	1.467E-14	1.503E-15
21.5	3.030E+08	0	2.259E-14	2.979E-15
30.0	6.660E+08	0	2.413E-14	2.077E-15
40.0	8.170E+08	0	2.157E-14	1.773E-15
53.0	1.575E+09	0	2.011E-14	1.233E-15

Table 8.4: The results of the proton irradiation of the ISSI memory at the RADEF facility

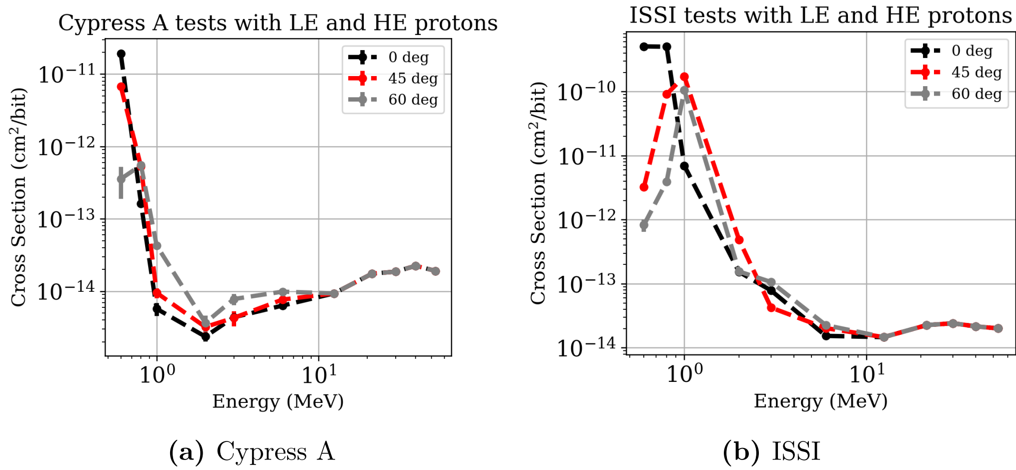

(a) Cypress A **(b)** ISSI

Figure 8.3: The comparison between different tilting angles from the proton testing of Cypress A and ISSI memories

8.3 Low-Energy Proton Testing of Artix-7

In addition to the SRAM memories, the Artix-7 test board Arty was tested in a low-energy proton beam at the RADEF facility in Jyväskylä, Finland. Since the Artix-7 is a highly integrated technology of the 28 nm, it would be expected, as described in [13], that the device has a low critical charge. Accordingly, the device can therefore also be sensitive to direct ionization by protons and hence a peak in the SEU cross-section would be expected at low proton energies.

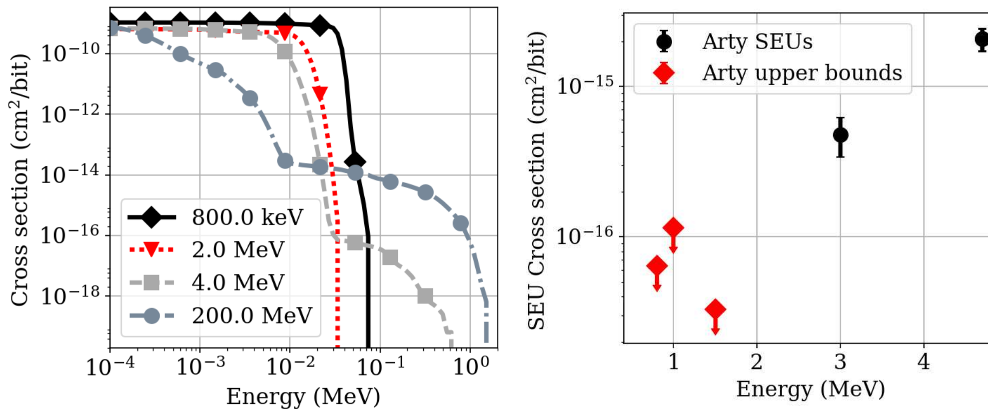

Figure 8.4: left) FLUKA simulation for the 300 nm × 300 nm sensitive volume geometry showing the cross-section as a function of deposited energy and right) results of the low-energy proton irradiation of the Artix-7 board showing the experimental cross-section as a function of beam energy [2].

To determine if a device is sensitive to direct ionization by charged particles, in theory, both electrons and protons could be used as the energy deposition cross-section shape, and the energy deposition mechanisms are similar, as explained in chapter 5. However, the absolute cross-section for electrons is orders of magnitude lower for electrons, and as such, the testing with protons requires a smaller fluence and therefore a much shorter testing time. Thus, the Arty was tested at the low-energy proton a line at RADEF. The test procedure was similar to the intermediate-energy electron tests on the same device, described in chapter 6 [2].

The proton beam tests were performed from 0.8 MeV to 4.7 MeV. A highly-integrated device such as the Artix-7 BRAM would be expected to display a direct ionization peak at around or below ~ 1 MeV, as seen in [57]. However, no events were recorded under 3 MeV, which indicates that the device is not sensitive to direct proton ionization, for the lower energies only upper bounds for cross-sections were found, which here are the inverse of the fluence. The results are summarized in Table 8.5 and illustrated on the right of Fig. 8.4.

FLUKA energy deposition simulations were performed on a 300 nm × 300 nm × 500 nm sensitive volume geometry, as described in chapter 5 and [2], the results can be seen in

Fig. 8.4. The cross-section for low deposited energy is constant (i.e. corresponding to the sensitive area) in the direct ionization region and then sharply falls off for higher deposited energies. The region of higher energy deposition is due to the nuclear/indirect ionization events depositing high energies near the sensitive volumes in the device. As can be seen, for energies below about 3 MeV, almost no energy is deposited through indirect ionization, which supports the experimental results [2].

RADEF Low Energy Proton				
Energy (MeV)	**Flux ($p/cm^2/s$)**	**Fluence (p/cm^2)**	**SEUs**	**Cross-section (cm^2/bit)**
4.7	5×10^7	1.21×10^{10}	36	2.07×10^{-15}
4.7	1×10^7	1.04×10^{10}	31	2.07×10^{-15}
3.0	6×10^7	1.74×10^{10}	12	4.79×10^{-16}
1.5	5×10^7	2.12×10^{10}	0	*3.27×10^{-17}
1	5×10^6	6.08×10^9	0	*1.14×10^{-16}
0.8	1×10^7	1.09×10^{10}	0	*6.37×10^{-17}
RADEF Electron				
Energy (MeV)	**Dose rate (rad/min)**	**Total Dose (krad)**	**SEUs**	**Cross-section (cm^2/bit)**
20.0	1.00×10^2	100	2	3.81×10^{-19}
VESPER				
Energy (MeV)	**Duration(h)**	**Fluence (e^-/cm^2)**	**SEUs**	**Cross-section (cm^2/bit)**
60	3.1	6.30×10^{11}	21	2.37×10^{-17}
63	18.6	3.80×10^{12}	93	1.70×10^{-17}
201	1.8	1.98×10^{11}	11	3.86×10^{-17}
201	4.3	4.66×10^{11}	38	4.76×10^{-17}

Table 8.5: Artix-7 irradiation results at the low energy proton and electron lines at RADEF and the VESPER facility. fields marked with * are the upper bounds for the cross-sections [2].

8.4 Mixed-Field Testing of the SRAM Memories

To evaluate the contribution of low-energy protons in a mixed-field environment, such as the accelerator environment at the LHC at CERN, testing at the mixed-fielding testing facility CHARM was performed.

The mixed-field testing facility CHARM is situated at CERN in Switzerland and is described in detail in section 4.4. The three memories tested were the two Cypress 90 nm (A and B) and the ISSI memories described in section 4.5.4. The memories were biased

at the nominal voltage of 3.3 V and placed in the mixed-field of CHARM mounted on the CERN SEU monitors. The memories were programmed in a checkerboard pattern and read periodically every 6 minutes due to the possibility of inducing an error in the CERN SEU tester rendering the readout impossible. This is because the whole setup was exposed to radiation due to the mixed-field extending throughout the irradiation room in the facility. A picture of the setup mounted on test position G0 in the CHARM facility can be seen in Fig. 8.5.

Figure 8.5: The CERN SEU monitors mounted on the test position at the CHARM facility at CERN.

As described in section 4.4, the CHARM facility has different configurations - the various test positions and also the configuration of the shielding. To convert from the counts on the secondary emission counter to the number of particles on target (POT), one has to multiply the counts with the calibration factor, as specified in [9]. Then, to obtain the number of high-energy hadrons (HEH) from the POT, a FLUKA simulated calibration factor has to be used [59]. The calibration factors used for the various test positions used in the experimental campaign can be seen in Table 8.6.

Configuration	HEH to POT Factor
CuOOOO	7.670×10^{-6}
CuCIIC	5.10×10^{-7}

Table 8.6: The calibration factors to convert from POT to HEH fluence for each configuration used in the experimental campaign at the CHARM facility in this work.

The results of all the irradiation performed at the CHARM facility can be seen in Table 8.7.

Comparisons with the RADEF high-energy protons runs can be made to evaluate the results of the mixed field irradiations. The highest energy tested at the RADEF facility

DUT	Configuration	HEH Fluence (p/cm^2/bit)	Cross-Section (cm^2/bit)	Comments
Cypress A	CuCIIC	5.270E+08	2.067E-14	
Cypress A	CuOOOO	2.418E+10	1.790E-14	
Cypress B	CuOOOO	1.176E+10	4.554E-14	
ISSI	CuCIIC	5.323E+08	7.183E-14	
ISSI	CuCIIC	1.060E+09	3.330E-14	boron
ISSI	CuOOOO	2.410E+10	2.485E-14	
ISSI	CuOOOO	8.520E+10	2.060E-14	boron

Table 8.7: The results of the mixed-field irradiations at the CHARM facility

was 53 MeV. This value is already at the saturation energy of the Weibull proton cross-section curve and therefore can be used as a direct comparison between the mixed-field measurements and the proton irradiation.

As can be seen in Fig. 8.6, the cross-section for both the Cypress A and the ISSI are very close to the mixed-field measurements. Since it was shown through the low-energy proton measurements that both devices are sensitive to direct ionization, the result implies that the overall contribution of low-energy protons and electrons to the mixed-field cross-section is negligible for this technology node.

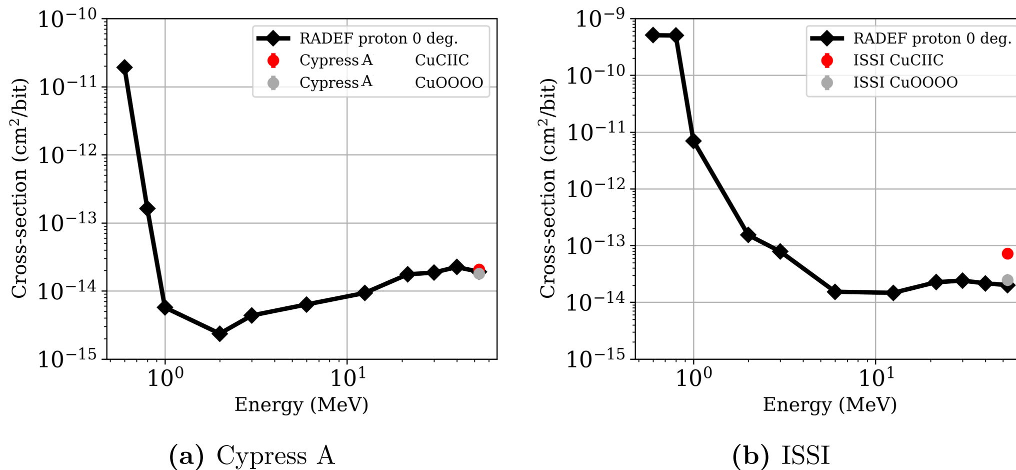

(a) Cypress A **(b)** ISSI

Figure 8.6: The comparison between the irradiations at the CHARM facility and the proton irradiations at the RADEF facility. The CHARM results are plotted at the highest energy tested at RADEF (53 MeV), whereas in reality the proton beam hitting the target has an energy of 24 GeV.

As opposed to the other mixed-field experimental comparisons with the proton cross-section, the ISSI shielded (CIIC) configuration cross-section is higher. It will be explained in the following section how this increase can be attributed to thermal neutrons.

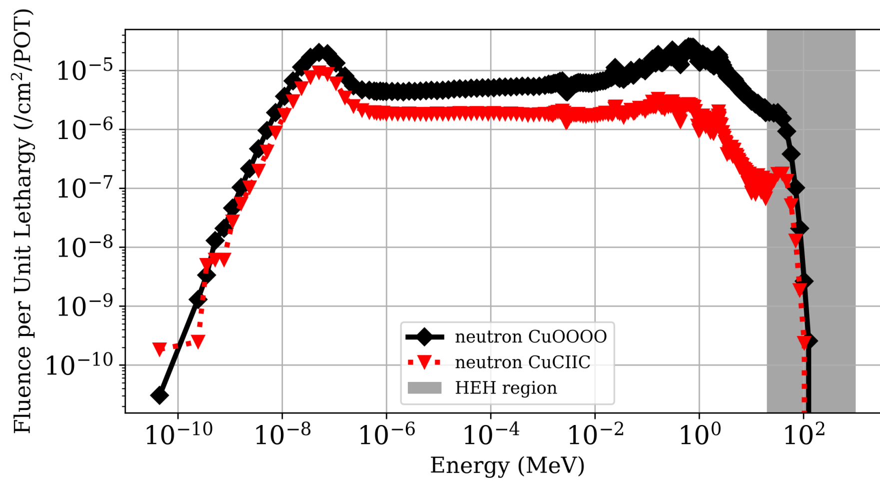

Figure 8.7: The comparison between the neutron spectra of the full shielding and no shielding with copper target configurations at the G0 position at the CHARM facility [59].

8.4.1 Thermal Neutron Contribution for the SRAM Memories

In addition, irradiations to estimate the effect that thermal neutrons have on the overall SEU cross-section of the ISSI memory were performed. As described in [76], boron carbide eliminates the thermal neutron contribution of the mixed-field. Therefore, irradiations were performed with the addition of boron carbide (B_4C) sheets; these are marked with the comment “boron” in Table 8.7. As seen in Fig. 8.8, the cross-section was reduced by factor ~ 2 for the shielded (CIIC) configuration with the addition of boron. However, the non-shielded configuration was hardly affected.

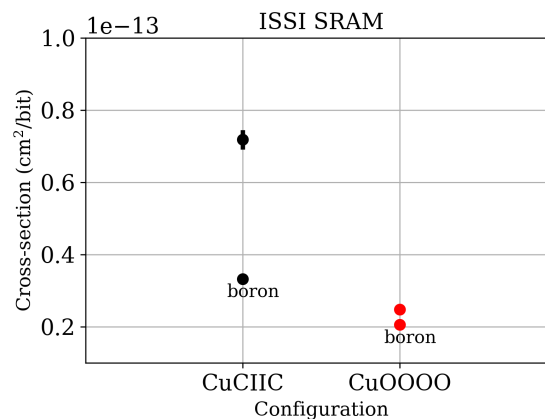

Figure 8.8: The comparison between the cross-section with and without the boron carbide (B_4C) sheets

This suggests that thermal neutrons have a sizable contribution to the overall SEU cross-section in the mixed-field environment. To precisely assess the contribution of the

cross-section from HEH and thermal neutrons the following equations can be used

$$
\begin{aligned}
N_{SEU} &= \sigma_{HEH}\Phi_{HEH_{eq}} + \sigma_{TH}\Phi_{TH} \\
N_{SEU} &= \Phi_{HEH}(\sigma_{HEH} + R\sigma_{TH})
\end{aligned}
\tag{8.3}
$$

where HEH stands for high-energy hadron equivalent, TH stands for thermal neutrons, R or hardness factor is the relation between the fluence of HEH to thermal neutrons, which describes the hardness of the environment, σ is the cross-section and Φ is the fluence. Here we assume that the total number of SEU is the combination of a contribution from both thermal neutrons and HEH.

Therefore, if we approximate the known experimental cross-section for HEH, which in our case is the high-energy proton irradiation result and the hardness factor R of our environment, we can estimate the cross-section for HEH and the cross-section for thermal neutrons in an indirect manner as follows:

$$
\begin{aligned}
R &= \Phi_{TH}/\Phi_{HEH} \\
\sigma^*_{HEH} &= \sigma_{HEH} + R\sigma_{TH} \\
\sigma_{TH} &= (\sigma^*_{HEH} - \sigma_{HEH})/R
\end{aligned}
\tag{8.4}
$$

The R factor for the G0 position at CHARM can be found in [77] and is 3.8 for the no shielding case (CuOOOO) and 21 for the full shielding case (CuCIIC). The hardness factor for the shielded case is ~ 5 times higher than for the non-shielded case, which implies that the relative amount of thermal contributions is considerably higher in the shielded case, as can be seen in Fig. 8.7.

For the Cypress A memory, the cross-section for the shielded and the non-shielded is quite similar, therefore as a first approximation, the device is not sensitive to thermal neutrons. The shielded CHARM cross-section is slightly lower than for the HE proton cross-section when applying Eq. 8.4, one finds that the contribution for thermal neutrons is very close to 0%. Therefore, it can be concluded that the Cypress A memory is not sensitive to thermal neutrons.

For the ISSI memory, the shielded configuration cross-section is higher than for the non-shielded configuration. As reflected by the higher R factor, the thermal neutron flux is higher, therefore devices which are sensitive to it would have a higher cross-section. This is also reflected in the ISSI cross-section, and the thermal neutron contribution is estimated as $2.46 \times 10^{-15}\,\text{cm}^2/\text{bit}$.

$$
\sigma_{TH_{CIIC}} = (7.183 \times 10^{-14} - 2.011 \times 10^{-14})/21 = 2.46 \times 10^{-15}\,\text{cm}^2/\text{bit} \tag{8.5}
$$

This thermal neutron cross-section can be assessed more precisely by using Eq. 8.3 and assuming the σ_{HEH} and σ_{TH} are both unknowns. We can then compare the two

configuration cases and we obtain two equation with two unknowns as follows:

$$\begin{aligned} \sigma^*_{HEH_A} &= \sigma_{HEH} + R_A \sigma_{TH} \\ \sigma^*_{HEH_B} &= \sigma_{HEH} + R_B \sigma_{TH} \end{aligned} \tag{8.6}$$

where $\sigma^*_{HEH_A}$ is the cross-section for the shielded case (CuCIIC) and $\sigma^*_{HEH_B}$ is the equivalent for the non-shielded case (CuOOOO). Since the thermal neutron cross-section remains constant between the shielding configurations, the thermal neutron cross-section can be found as

$$\begin{aligned} \sigma_{TH} &= \frac{\sigma^*_{HEH_B} - \sigma^*_{HEH_A}}{R_B - R_A} \\ &= \frac{(7.2 - 2.5) \times 10^{-14}}{21 - 3.8} \\ &= 2.73 \times 10^{-15}\,\mathrm{cm}^2/\mathrm{bit} \end{aligned} \tag{8.7}$$

The thermal neutron cross-section is therefore found to be $2.73 \times 10^{-15}\,\mathrm{cm}^2/\mathrm{bit}$, which is quite close to the first estimate of $2.46 \times 10^{-15}\,\mathrm{cm}^2/\mathrm{bit}$. This confirms that the shielded configuration cross-section has a sizable contribution from thermal neutrons, which in turn proves that the ISSI SRAM is sensitive to them.

9 Discussion and Radiation Hardness Assurance Implications

As electron-induced SEE is a relatively new topic, electron testing has not been included in most testing procedures and standards such as the ECSS [45] used for space applications. However, given the continuing development of electronics and the ever decreasing critical charges required to cause upsets in devices, in some circumstances electron-induced upsets could have a significant contribution to the overall upset rate. The general considerations for radiation hardness assurance (RHA) for electron-induced SEE will be discussed in section 9.2 and application-specific RHA for the Jovian environment, and more specifically the JUICE mission, will be discussed in section 9.3. An analysis of possible alternative sources for the electron-induced upsets is described in section 9.1. In addition, the contribution that low-energy protons have on a mixed-field cross-section is discussed in section 9.4, where also the thermal neutron impact on the overall cross-section is discussed.

9.1 Possible Alternative Causes of Electron-Induced SEE

In addition to the experimental results, possible alternative causes for the electron-induced SEU were analyzed. The first possible explanation to an alternative justification for the SEUs observed during the irradiation is the possibility that more than one electron hit the sensitive area of the device within a sufficiently small time window and the cumulative charge built up in the sensitive areas cause the upset [16]. To evaluate this, the probability of two or more electrons causing an upset in the same cell during the relaxation time of a previous upset can be calculated as [17]

$$Pr(X_1||X_2) = (\phi A_{cell}\tau)^2 \tag{9.1}$$

where ϕ is the incident flux obtained through FLUKA of the simulations of the spectra of the beam at the DUT position, A_{cell} is the area of the sensitive area and τ is the relaxation or response time for an upset event. As described in [78] and [79], the most appropriate time for the ESA monitor technology size would be 100 ps. The probability for the ESA SEU monitor is then $(2 \times 10^{14}\,\mathrm{e/cm/s} \cdot 10\,\mathrm{\mu m}^2 \cdot 100\,\mathrm{ps})^2 = 4 \times 10^{-6}$, where the flux is the

flux during one pulse. Also, even several electrons depositing the maximum possible energy through direct ionization would not be enough to reach the LET threshold [1]. This was shown experimentally with varying beam intensities for the SEU testing of the ESA SEU monitor as explained in chapter 6.

Secondly, neutrons created by the primary electron beam interacting with the various beamline elements could contribute to the SEU cross-section. As the SEU cross-section for neutrons is several magnitudes higher than for electrons, even small fluxes of neutrons can have an effect. A FLUKA simulation was performed with the basic geometry of the beamline upstream of the VESPER facility to analyze this possibility in more detail. The two main elements intercepting the beam are the BTV screen, which is a 1.1 mm chromium oxide screen used to monitor the beam size and position, and a 2 mm stainless steel beam exit window. The exact results are described in [1], a conclusion was that the yield of neutrons is eight orders of magnitude lower than of electrons [1].

The fluxes were folded with the appropriate Weibull fits for the ESA SEU monitor from [1] to estimate the effect this neutron contribution had on the final SEU cross-sections. The exact calculations can be found in [1] and the conclusion was that the resulting electron cross-section was four orders of magnitude higher than from neutrons. Therefore, the neutron contribution can be regarded as negligible [1].

Thirdly, experiments were performed to strengthen the conclusion of the first point presented in this section. As shown by [17], if prompt dose effects or pile-up caused the upsets seen during irradiations, the cross-section would vary exponentially with the intensity. Measurements with varying particle fluxes were performed to verify that this exponential relationship was not present in the experimental results. If the cross-section of the device is independent of the beam flux, the pile-up effect is ruled out. Measurements have been performed on the SEL-sensitive ISSI memory at 210 MeV with a beam charge of 3.5 pC with a cross-section of $(3.2^{+5.9}_{-1.0}) \times 10^{-11}\,\mathrm{cm}^2$ and at 215 MeV at 15 pC with a cross-section of $(1.76^{+3.83}_{-0.65}) \times 10^{-11}\,\mathrm{cm}^2$ [3]. The upper and lower limits were found assuming 95% confidence bounds. The difference between the cross-section is compatible with the statistical uncertainty and whats more the average cross-section value for the lower beam charge is higher, further confirming that this is not a pile-up effect. Additionally, the change in cross-section is then much less compared to the change in beam charge, which is increased by 4.3 times.

9.2 Electron-Induced SEE RHA

To ensure that a given component is free of proton-induced effects it has to be tested with heavy ions up to an LET of at least 40 MeV cm^2/mg, as described in [71]. Although most of the nuclear interaction products produced in silicon by protons are under ~15 MeV cm^2/mg,

high-Z materials present near the sensitive volumes in devices can produce fission fragments with energies close to these LET. In addition to the LET requirement, a component would have to be tested with the highest proton energy present in the intended environment to ensure it is completely SEE free [3, 71].

As discussed in chapter 5 and in [3], electrons can produce nuclear interaction product with LET values up to ~13 MeV cm^2/mg and fission fragments due to high-Z materials up to 40 MeV cm^2/mg in a similar manner to protons - through nuclear interactions. Therefore, similar testing guidelines can be applicable for electrons as for protons [3].

It was shown in chapter 5 through simulation and in chapter 6 experimentally, that the electron-induced SEEs are caused by the electro-and photo-nuclear reactions for devices with a relatively large critical charge ($\sim$ 10 fC) and is $\sim$ 3 orders of magnitude lower than for protons. A summary of the experimental electron- and proton-induced SEE cross-sections for devices tested in the scope of this work can be seen in Table 9.1. As is evident, the proton and the electron cross-sections ratio is constant for similar devices and upset types, as is the case for the SEL-sensitive memories. In addition, the ratio, which is similar to the inelastic interaction cross-section ratio between electrons and protons described in section 5, is evident in both larger technology node devices, such as the ESA SEU monitor (250 nm) and the smaller technology node devices, such as the Arty (28 nm).

Device	**Upset Type**	**Electron XS (cm^2)**	**Proton XS (cm^2)**	**p/e- ratio**
ESA SEU mon.	SEU	3.84×10^{-18}	2.6×10^{-14}	6.8×10^3
Arty	SEU	6×10^{-18}	8.7×10^{-15}	1.1×10^3
ISSI	SEL	3×10^{-11}	3.1×10^{-8}	1.0×10^3
Alliance	SEL	$5 \times 10^{-12}*$	7.5×10^{-9}	1.5×10^3
Brilliance	SEL	1.34×10^{-10}	3.1×10^{-7}	2.3×10^3

Table 9.1: Comparison between the proton and electron cross-section for devices tested in this work. The SEL cross-section values for protons for the ISSI Alliance and Brilliance memories are from [80]. *The electron SEL cross-section value of the Alliance memory is an upper limit.

The SEL cross-section for the memories in this work have an electron-induced SEL cross-section which is several orders of magnitude lower than for the equivalent proton cross-section. For the Brilliance memory, a proton saturation cross-section is $\sim 3 \times 10^{-7}$ cm^2 [67], whereas for electron testing it was found to be 3.3×10^{-10} cm^2.

As there are still not many high-energy electron facilities established as commercial test facilities, electron testing of components can be relatively complicated. A possible strategy for screening components for electron-induced effects is to use protons instead. As shown in chapter 5, protons have a very similar shape to the energy deposition curve; however, the absolute cross-section for nuclear events is several orders of magnitude higher. This means

that for SEE testing a smaller fluence and therefore a shorter testing time is required. This is also true for devices with high-Z materials near sensitive volumes as the maximum LETs of the fission fragments created through nuclear interaction are similar. It was also shown in this work that if the device is not sensitive to proton direct ionization, it is not going to be susceptible to electron direct ionization.

In general, in [71] it has been suggested for protons, that for device qualifications the radiation environment the device is to be used in should be taken into consideration when planning the testing. The same consideration can be applied to electron testing, with the additional factor that it is possible to substitute for proton testing instead. If the device is not sensitive to proton-induced SEE, it will not be sensitive to electron-induced SEE [3].

9.3 SEU Rate in the Jovian Atmosphere

Extra considerations have to be made as soon as shielding material is introduced in front of the electronics, the photon-induced SEE cross-section begins to dominate, even for small thicknesses of shielding. This is especially problematic in high-energy environments where electronics are protected from the radiation environment by shielding, such as space or high-energy physics experiments. An example of the case of the JUICE space mission is given below.

As previously discussed, secondary radiation is produced by energetic particles passing through the shielding materials. Bremsstrahlung, caused by the slowing down by electrons scattering off atomic nuclei, is considered a significant secondary source of radiation for the JUICE mission [11].

To estimate the SEU rate inside the spacecraft the spectrum of the secondary radiation, shown in chapter 4, is folded with the Weibull response of the ESA SEU monitor, the procedure is described in more detail in [1]. The resulting estimation for the cross-section contribution for each particle can be seen in Fig. 9.1. To evaluate the contribution of each particle group to the total error rate, only the trapped radiation was considered. The result for the combined contributions from trapped electron and proton spectra can be seen in the rightmost plot in Fig. 9.1. As shown, the neutron and proton contributions to the total upset rate are dominated by the trapped proton generated events, while the electrons and photons are dominated by the trapped electron induced events. Specifically, the secondary photons generated by trapped electrons passing through the shielding materials as described in [1] and chapter 4.

As described in chapter 5, the first estimation of the cross-section can be obtained by multiplying fluence with the Weibull saturation cross-section for each particle. Here the integrated fluence of secondaries relevant for SEE rate estimation generated by the Jovian trapped particle fluence passing through shielding, as seen in chapter 4, and the saturation

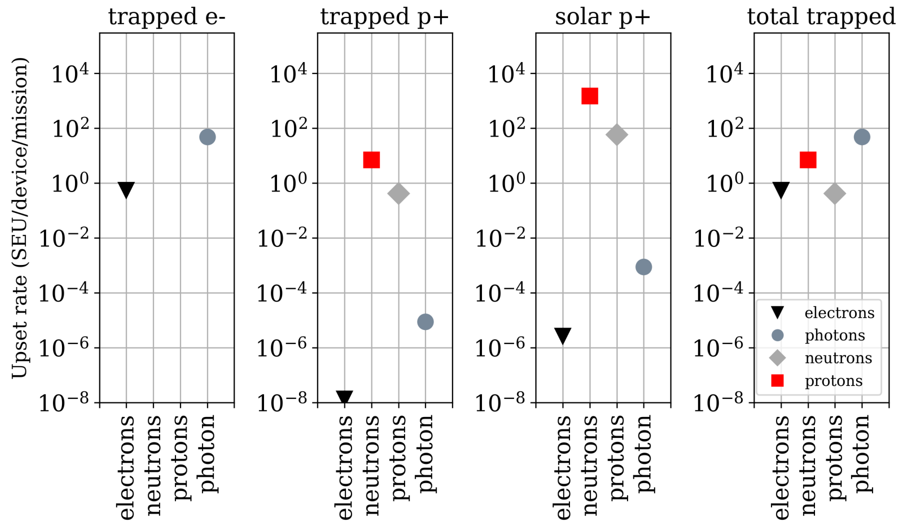

Figure 9.1: Upset rate for trapped protons and electrons and solar protons transported through shielding for each electrons, positrons, protons and neutrons [1]

cross-sections found for the ESA SEU monitor in [2] are multiplied to find a first estimation for the cross-section. As can be seen in Table. 9.2, the cross-section values as a first estimation correspond well to the more detailed folding described previously for photons and neutrons. However, due to the large energy range between the threshold energy and the energy by which the saturation cross-section is reached, the estimated electron SEU cross-section is higher for this first-step approach. However, it is important to note that even with this first approximation, the photon contribution remains one order of magnitude higher than the electron contribution, which confirms that the secondary photons have a substantial contribution to the overall SEU rate for devices with a large critical charge value.

	Secondaries - Trapped Electrons	
Particle	**Int. Fluence > 10 MeV (p/cm^2)**	**SEU XS (cm^2)**
electrons	4.2×10^{10}	5.23×10^{1}
protons	0	0
neutrons	0	0
photons	6.7×10^{10}	1.91×10^{2}
	Secondaries - Trapped Protons	
Particle	**Int. Fluence > 10 MeV (p/cm^2)**	**SEU XS (cm^2)**
electrons	5.3×10^{2}	3.58×10^{-7}
protons	1.7×10^{7}	7.49
neutrons	1.1×10^{6}	4.63×10^{-1}
photons	4.1×10^{4}	1.17×10^{-4}

Table 9.2: The integrated flux of secondaries created by propagating the trapped particle spectra through 20 mm Aluminium + Tantalum shielding and the estimated cross-section for the ESA SEU monitor, saturation cross-sections from [2]

9.4 Low-Energy Proton and Electron Contribution to the Mixed-Field

As shown in chapter 8, irradiations were made in a mixed-field facility to evaluate the impact low-energy protons and electrons have on the total mixed-field upset rate. To assess the results of the mixed field irradiations, comparisons with the RADEF high-energy protons runs can be made. The highest energy tested at the RADEF facility was 53 MeV. This value is already at the saturation energy of the proton SEE Weibull curve and therefore be used as a direct comparison between the mixed-field measurements and the proton irradiation.

As was shown in chapter 8, the cross-section for both the Cypress 65nm and the ISSI are very close to the mixed-field measurements. Since it was shown through the low-energy proton measurements that both devices are sensitive to low-energy protons, the result implies that the overall contribution of low-energy protons and electrons to the mixed-field cross-section is negligible.

However, since the shielded configuration cross-section for ISSI was a factor ~ 2 higher than the non-shielded one, other contributions to the cross-section had to be evaluated. The most probable cause for the increased cross-section is the thermal neutron contribution. To check this hypothesis boron carbide was added as shielding to the memories. As shown, the ISSI memory shows a sensitivity to thermal neutrons. The cross-sections for the irradiation results with the boron shielding and the results show a clear decrease in the contribution thermals have to the total cross-section, as shown in chapter 8. For the shielded case the

contribution from thermals drops from 12% to $\simeq 4\%$. Due to the significant drop in the thermal neutron contribution with the addition of the boron shielding, it can be concluded that the increased cross-section in the full shielding configuration is due to the thermal neutron contribution.

The R factor or the "risk" factor is the figure of merit in terms of the flux of thermal neutrons compared to high energy hadrons in an environment. The R factor enables for a quick approximation of the response of devices that are sensitive to thermal neutrons, such as the ISSI memory. Certain regions in high-energy physics experiments, such as some areas of the LHC accelerator at CERN, have a high R factor. This implies that the flux of thermal neutrons will have a significant impact on the SEU rate of the devices that are sensitive to them. When considering devices for these environments, it is therefore necessary to estimate their thermal neutron sensitivity.

10 Conclusions and Future Work

10.1 Conclusions

It has been shown through experiments and simulations in this work that electrons are capable of inducing single-event effects in modern electronic devices. An extensive experimental campaign conducted both at the Vesper facilities at CERN and the RADEF facilities in Finland show the main mechanisms inducing these events are the indirect energy deposition or nuclear events [1, 2]. As explained in [31], given that the critical charge of the device is small enough, it is possible that the cross-section can be dominated by other effects such as the Rutherford scattering. Furthermore, the results indicate that the cross-section of electron-induced upsets is independent of the technology node, proved by the comparison of a 250 nm device ESA SEU monitor and the Artix-7 test board Arty, which is a 28-nanometer device, as shown by simulations in chapter 5 and the experimental results in chapter 6 [1, 2]. It was also shown that electrons are capable of depositing enough dose to induce potentially destructive events such as latch-ups [3]. The experimental results vary from 12 MeV up to 20 MeV which enables us for the first time to draw a full Weibull cross-section of the electron-induced single-event effects.

The possible contribution from other particles, such as neutrons, created by the electron interactions with beamline elements of both the medical linac facility at RADEF and the VESPER facility were analyzed. In addition, numerical analysis was performed showing that the probability of pile-up effects being responsible for the SEUs observed was negligible. This conclusion was backed up further by performing irradiations with varying fluxes both at the medical linac at RADEF, with the addition of shielding material and during SEL testing at VESPER. All of the experimental results rule out the exponential increase in cross-section which is characteristic of pile-up effects [1−3, 17].

A study into the various shielding materials used in space missions and their contribution to the overall SEU cross-section was performed. The implications of the secondary photons, neutrons, and electrons created when the high-energy electrons pass through the shielding material are discussed. A good fit between the experimental and the simulated cross-sections is shown. This work demonstrates that even a small amount of shielding material has a significant impact on the overall SEU cross-sections and should, therefore, be accounted

for when evaluating the performance of components for use in shielded harsh radiation environments [1, 2].

A practical application of folding the Jovian trapped electron spectra with the experimental electron-induced SEU Weibull fit is shown. Even though the overall cross-section of electron-induced SEU is several orders of magnitude lower than that of protons, the large fluxes of trapped electrons in the Jovian atmosphere create the same order of magnitude of upsets through secondary particles like protons [1, 2].

First experimental evidence showing electron-induced SEL has been shown as a part of this work. It has been shown through simulation in [1] that electrons and photons are capable of producing nuclear interaction product with a LET of up to 13 $\mathrm{MeVcm^2/mg}$ and 15 $\mathrm{MeVcm^2/mg}$ respectively. Therefore, the SEL observed in the DUT are attributed to these nuclear interaction products. Moreover, a device with a LET onset value of 15 $\mathrm{MeVcm^2/mg}$ experienced no SEL events, which further implies that the silicon nuclear reaction products are responsible for the SEL events.

As electrons and photons are shown to be capable of producing products with similar LET values, the implication to RHA is similar to the one suggested for protons in [71]: one should test with the highest energy present in the intended environment. In addition, where high-Z materials are present, fission fragments with LETs of up to 45 $\mathrm{MeVcm^2/mg}$ are created. Therefore, testing with heavy-ions with LET values of at least 40 $\mathrm{MeVcm^2/mg}$ is advised [71]. Electrons and photons have been shown to produce fission fragments with similar LETs of up to $\sim 40\,\mathrm{MeVcm^2/mg}$. Therefore, a similar approach is proposed for electrons to cover the highest possible LET fragments generated. Proton testing can be seen as a suitable substitute since electrons, photons, and protons all produce fission fragments with similar LET values, due to tungsten interactions and beam-silicon recoils. The added benefit from proton testing is the lower fluence, and therefore time and cost, needed for device qualification.

Finally, the effect of low-energy protons, and as an extension electrons as the energy deposition mechanism is the same, in a mixed-field environment was analyzed. Experimental work at the CHARM facility at CERN showed that the contribution of these low-energy particles is negligible in both the 65 nm and 90 nm SRAM device tested. In addition, it was shown that the 65 nm device was sensitive to thermal neutrons by comparing experimental results from irradiations both with and without boron carbide shielding.

10.2 Future Work

Many aspects of the electron-induced SEE remain to be studied more in depth. Firstly, different single-event effects caused by electrons need further assessment. Single-event burnout (SEB) induced by electrons is one of these as power devices are used extensively

both within the space and high-energy domain. As was discussed in section 9.2, since electrons are capable of induced high LET nuclear interaction fragments, they are in theory also capable of inducing hard failures such as the SEB. Another effect is the displacement damage. With high fluences of electrons in the trapped radiation belts in the Jovian environment, many sensitive detectors and solar panels are directly exposed, leaving them vulnerable for this type of damage.

Additionally, a study involving different technology nodes of electronic components should be performed. As shown experimentally in chapter 6 and through simulations in chapter 5, the primary mechanisms by which electrons deposit energy in the sensitive volume is highly dependent on the critical charge of the device. This is similar to the effect that protons have, as direct ionization only affects devices with low enough critical charge values. Therefore, comparing different device generations in the same radiation environments would provide additional proof for this effect and help to determine the critical charge range for which the various effects dominate. A study involving the SRAM memories described in chapter 8 would be the most appropriate as tests with heavy ions, low- and intermediate-energy protons and a mixed-field radiation environment have been performed.

Some experiments have been performed as a part of this thesis to assess the contribution that photons have on the total cross-section. Additional simulations with varying degrees of shielding should be performed to cross-check the simulated increase. As the experimental and simulation results agree well for the experiments run with copper, discussed for experiments in chapter 6 and simulations in chapter 5, additional tests with varying shielding material thickness and density would complete the analysis and help in confirming the point where the photon contribution dominates over the electron contribution to the overall SEE cross-section.

Bibliography

[1] M. Tali, R. Alia, M. Brugger, R. Corsini, W. Farabolini, V. Ferlet-Cavrois, A. Mohammadzadeh, G. Santin, and A. Virtanen, “High-energy Electron Induced SEUs and Jovian Environment Impact,” *IEEE Trans. Nucl. Sci.*, vol. 64, no. 8, pp. 2016 – 2022, Aug 2017.

[2] M. Tali, R. Garcia Alia, M. Brugger, V. Ferlet-Cavrois, R. Corsini, W. Farabolini, A. Javanainen, M. Kastriotou, H. Kettunen *et al.*, “Mechanisms of Electron-Induced Single-Event Upsets in Medical and Experimental Linacs,” *IEEE Trans. on Nucl. Sci.*, vol. 65, no. 8, pp. 1715–1723, Jun 2018.

[3] M. Tali, R. G. Alia, M. Brugger, V. Ferlet-Cavrois, R. Corsini, W. Farabolini, A. Javanainen, G. Santin, C. B. Polo, and A. Virtanen, “Mechanisms of electron-induced single event latchup,” *IEEE Trans. on Nucl. Sci.*, Aug 2018.

[4] R. G. Alía, P. F. Martínez, M. Kastriotou, M. Brugger, J. Bernhard, M. Cecchetto, F. Cerutti, N. Charitonidis, S. Danzeca *et al.*, “Ultra-Energetic Heavy Ion Beams in the CERN Accelerator Complex for Radiation Effects Testing,” *IEEE Transactions on Nuclear Science*, 2018.

[5] R. G. Alia, M. Brugger, M. Cecchetto, F. Cerutti, S. Danzeca, M. Delrieux, M. Kastriotou, M. Tali, S. Uznanski *et al.*, “SEE testing in the 24 GeV proton beam at the CHARM facility,” *IEEE Trans. on Nucl. Sci.*, vol. 65, no. 8, pp. 1750 – 1758, Apr. 2018.

[6] F. Pozzi, R. Garcia Alia, M. Brugger, P. Carbonez, S. Danzeca, B. Gkotse, M. Richard Jaekel, F. Ravotti, M. Silari, and M. Tali, “CERN irradiation facilities,” *Radiation protection dosimetry*, pp. 1–5, 2017.

[7] M. Glorieux, A. Evans, T. Lange, A.-D. In, D. Alexandrescu, C. Boatella-Polo, R. G. Alía, M. Tali, C. U. Ortega *et al.*, “Single-Event Characterization of Xilinx UltraScale+® MPSOC under Standard and Ultra-High Energy Heavy-Ion Irradiation,” in *2018 IEEE Nuclear & Space Radiation Effects Conference (NSREC 2018)*. IEEE, 2018, pp. 1–5.

[8] CERN, “CERN - Accelerators & Schedules,” 2019.

[9] J. Mekki, M. Brugger, R. Alia, A. Thornton, N. D. S. Mota, and S. Danzeca, “CHARM: A mixed field facility at CERN for radiation tests in ground, atmospheric, space and accelerator representative environments,” *IEEE Transactions on Nuclear Science*, vol. 63, no. 4, pp. 2106–2114, 2016.

[10] JUICE Team, “JUICE environment specification, Issue 5 Rev 5,” ESTEC/ESA, Noordwijk, Netherlands, Tech. Rep., 2017.

[11] JUICE Team, “JUICE environment specification,” ESTEC/ESA, Noordwijk, Netherlands, Tech. Rep., 2015.

[12] European Space Agency, “JUICE mission - website,” http://sci.esa.int/juice/.

[13] J. T. Wallmark and S. Marcus, “Minimum size and maximum packing density of nonredundant semiconductor devices,” *Proceedings of the IRE*, vol. 50, no. 3, pp. 286–298, 1962.

[14] B. D. Sierawski, J. A. Pellish, R. A. Reed, R. D. Schrimpf, K. M. Warren, R. A. Weller, M. H. Mendenhall, J. D. Black, A. D. Tipton *et al.*, “Impact of low-energy proton induced upsets on test methods and rate predictions,” *IEEE Transactions on Nuclear Science*, vol. 56, no. 6, pp. 3085–3092, 2009.

[15] B. D. Sierawski, M. H. Mendenhall, R. A. Reed, M. A. Clemens, R. A. Weller, R. D. Schrimpf, E. W. Blackmore, M. Trinczek, B. Hitti *et al.*, “Muon-induced single event upsets in deep-submicron technology,” *IEEE Trans. Nucl. Sci.*, vol. 57, no. 6, pp. 3273–3278, 2010.

[16] M. J. Gadlage, A. H. Roach, A. R. Duncan, M. W. Savage, and M. J. Kay, “Electron-induced single-event upsets in 45-nm and 28-nm bulk CMOS SRAM-based FPGAs operating at nominal voltage,” *IEEE Trans. Nucl. Sci.*, vol. 62, no. 6, pp. 2717–2724, 2015.

[17] M. P. King, R. A. Reed, R. A. Weller, M. H. Mendenhall, R. D. Schrimpf, B. D. Sierawski, A. L. Sternberg, B. Narasimham, J. K. Wang *et al.*, “Electron-induced single-event upsets in static random access memory,” *IEEE Trans. Nucl. Sci.*, vol. 60, no. 6, pp. 4122–4129, 2013.

[18] W. D. Loveland, D. J. Morrissey, and G. T. Seaborg, “Modern nuclear chemistry,” Oct 2005.

[19] G. F. Knoll, *Radiation detection and measurement.* John Wiley & Sons, 2010.

[20] C. J. Z. M. Berger, M.J. and J. Chang. (2005) ESTAR, PSTAR, and ASTAR: Computer Programs for Calculating Stopping-Power and Range Tables for Electrons, Protons, and Helium Ions (version 1.2.3).

[21] J. Wellisch, M. Kossov, and P. Degtyarenko, "Electro and gamma nuclear physics in Geant4," *arXiv preprint nucl-th/0306012*, 2003.

[22] C. v. Weizsäcker, "Ausstrahlung bei stößen sehr schneller elektronen," *Zeitschrift für Physik*, vol. 88, no. 9-10, pp. 612–625, 1934.

[23] L. Claude and R. Pier-Giorgio, *Principles Of Radiation Interaction In Matter And Detection (4th Edition).* World Scientific Publishing Company, 2016.

[24] T. C. May and M. H. Woods, "A new physical mechanism for soft errors in dynamic memories," in *Reliability Physics Symposium, 1978. 16th Annual.* IEEE, 1978, pp. 33–40.

[25] T. May, "Soft errors in VLSI: Present and future," *IEEE Transactions on Components, Hybrids, and Manufacturing Technology*, vol. 2, no. 4, pp. 377–387, 1979.

[26] A. Samaras, P. Pourrouquet, N. Sukhaseum, L. Gouyet, B. Vandevelde, N. Chatry, R. Ecoffet, F. Bezerra, and E. Lorfevre, "Experimental Characterization and Simulation of Electron-Induced SEU in 45-nm CMOS Technology," *IEEE Transactions on Nuclear Science*, vol. 61, no. 6, pp. 3055–3060, dec 2014.

[27] J. M. Trippe, R. A. Reed, R. A. Austin, B. D. Sierawski, R. A. Weller, E. D. Funkhouser, M. P. King, B. Narasimham, B. Bartz *et al.*, "Electron-induced single event upsets in 28 nm and 45 nm bulk SRAMs," *IEEE Transactions on Nuclear Science*, vol. 62, no. 6, pp. 2709–2716, 2015.

[28] C. Inguimbert, R. Ecoffet, and D. Falguère, "Electron induced SEUs: microdosimetry in nanometric volumes," *IEEE Trans. Nucl. Sci.*, vol. 62, no. 6, pp. 2846–2852, 2015.

[29] M. J. Gadlage, A. H. Roach, A. R. Duncan, A. M. Williams, D. P. Bossev, and M. J. Kay, "Soft Errors Induced by High-Energy Electrons," *IEEE Transactions on Device and Materials Reliability*, vol. 17, no. 1, pp. 157–162, mar 2017.

[30] M. J. Gadlage, A. H. Roach, A. R. Duncan, A. M. Williams, D. P. Bossev, and M. J. Kay, "Multiple-Cell Upsets Induced by Single High-Energy Electrons," *IEEE Transactions on Nuclear Science*, vol. 65, no. 1, pp. 211–216, jan 2018.

[31] P. Caron, C. Inguimbert, L. Artola, N. Chatry, N. Sukhaseum, R. Ecoffet, and F. Bezerra, "Physical Mechanisms Inducing Electron Single-Event Upset," *IEEE Transactions on Nuclear Science*, vol. 65, no. 8, pp. 1759–1767, aug 2018.

[32] W. L. Dunn and J. K. Shultis, "Exploring Monte Carlo methods," *Contemporary Physics*, 2012.

[33] A. Ferrari, P. R. Sala, A. Fasso, J. Ranft, A. Ferrari, P. R. Sala, A. Fassò, and J. Ranft, "FLUKA: A multi-particle transport code," in *CERN 2005-10 (2005), INFN/TC 05/11, SLAC-R-773*, 2005.

[34] G. Battistoni, S. Muraro, P. R. Sala, F. Cerutti, A. Ferrari, S. Roesler, A. Fasso, and J. Ranft, "FLUKA: A multi-particle transport code," in *Proceedings of the Hadronic Shower Simulation Workshop*, vol. 896. AIP, 2006, pp. 31−49.

[35] SPENVIS Collaboration, "SPENVIS − Space Environment Information System version 4.6.7," 2015.

[36] G. Santin, V. Ivanchenko, H. Evans, P. Nieminen, and E. Daly, "GRAS: A general-purpose 3-D modular simulation tool for space environment effects analysis," *IEEE Trans. Nucl. Sci.*, vol. 52, no. 6, pp. 2294−2299, 2005.

[37] S. Agostinelli, J. Allison, K. Amako, J. Apostolakis, H. Araujo, P. Arce, M. Asai, D. Axen, S. Banerjee *et al.*, "Geant4−a simulation toolkit," *Nuclear Instruments and Methods in Physics Research Section A*, 2003.

[38] J. Allison, K. Amako, J. Apostolakis, H. Araujo, P. A. Dubois, M. Asai, G. Barrand, R. Capra, S. Chauvie *et al.*, "Geant4 developments and applications," *IEEE Transactions on Nuclear Science*, 2006.

[39] B. D. Sierawski, M. H. Mendenhall, R. A. Weller, R. A. Reed, J. H. Adams, J. W. Watts, and A. F. Barghouty, "CRÈME-MC: A physics-based single event effects tool," in *Nucl. Sci. Symp. Conference Rec. (NSS/MIC)*. IEEE, 2010, pp. 1258−1261.

[40] A. J. Tylka, J. H. Adams Jr, P. R. Boberg, B. Brownstein, W. F. Dietrich, E. O. Flueckiger, E. L. Petersen, M. A. Shea, D. F. Smart, and E. C. Smith, "CREME96: A revision of the cosmic ray effects on micro-electronics code," *IEEE Trans. Nucl. Sci.*, vol. 44, no. 6, pp. 2150−2160, 1997.

[41] R. A. Weller, M. H. Mendenhall, R. A. Reed, R. D. Schrimpf, K. M. Warren, B. D. Sierawski, and L. W. Massengill, "Monte Carlo simulation of single event effects," *IEEE Transactions on Nuclear Science*, vol. 57, no. 4, pp. 1726−1746, 2010.

[42] M. H. Mendenhall and R. A. Weller, "A probability-conserving cross-section biasing mechanism for variance reduction in Monte Carlo particle transport calculations," *Nuclear Instruments and Methods in Physics Research Section A: Accelerators, Spectrometers, Detectors and Associated Equipment*, vol. 667, pp. 38−43, 2012.

[43] FLUKA Collaboration, "FLUKA Online Manual," Dec. 2018.

[44] V. Vlachoudis *et al.*, "FLAIR: a powerful but user friendly graphical interface for FLUKA," in *Proc. Int. Conf. on Mathematics, Computational Methods & Reactor Physics (M&C 2009), Saratoga Springs, New York*, 2009.

[45] ECSS Secretariat, "ECSS-E-ST-10-04C space environment standard," 2008.

[46] CLEAR collaboration, "CLEAR Facility CERN," 2017.

[47] M. Tali and VESPER collaboration, "VESPER Facility," 2017.

[48] M. Brugger, A. Errahhaoui, M. Kim, H.-S. Lee, S. Roesler, and H. Vincke, "Activation benchmark study at a 2.5 GeV electron accelerator," *Progress in Nucl. Sci. and Tech.*, vol. 4, pp. 363–366, 2014.

[49] T. T. Böhlen, F. Cerutti, M. P. W. Chin, A. Fasso, A. Ferrari, P. G. Ortega, A. Mairani, P. R. Sala, G. Smirnov, and V. Vlachoudis, "The FLUKA code: developments and challenges for high energy and medical applications," *Nucl. Data Sheets*, vol. 120, pp. 211–214, 2014.

[50] A. Konefał, *Undesirable radioisotopes induced by therapeutic beams from medical linear accelerators.* INTECH Open Access Publisher, 2011.

[51] M. Tali and R. G. Alía, "Radiation Test Report ESA Monitor and RadFET," CERN, Tech. Rep., 2016.

[52] Ashland, "Gafchromic™ XR-SP2 industrial radiographic film."

[53] RADEF group, "RADiation Effects Facility RADEF - Linear electron accelerator," 2016.

[54] A. Virtanen, "Radiation effects facility RADEF," in *On-Line Testing Workshop, 2002. Proceedings of the Eighth IEEE International.* IEEE, 2002, p. 188.

[55] A. Virtanen, J. Hyvönen, K. Ranttila, I. Rekikoski, and J. Tuppurainen, "Heavy ion and proton test site at JYFL-accelerator laboratory," *Nuclear Instruments and Methods in Physics Research Section A: Accelerators, Spectrometers, Detectors and Associated Equipment*, vol. 426, no. 1, pp. 68–71, 1999.

[56] E. Liukkonen, "The Jyvaskyla K130 Cyclotron Project," in *12th International Conference on Cyclotrons and Their Applications*, 1991, pp. 40–42.

[57] H. Kettunen, V. Ferlet-Cavrois, P. Roche, M. Rossi, A. Bosser, G. Gasiot, F.-X. Guerre, J. Jaatinen, A. Javanainen *et al.*, "Low energy protons at RADEF-application to advanced eSRAMs," in *Radiation Effects Data Workshop (REDW), 2014 IEEE.* IEEE, 2014, pp. 1–4.

[58] J. C. Liu, K. R. Kase, X. S. Mao, W. R. Nelson, J. H. Kleck, and S. Johnson, "Calculations of Photoneutrons from Varian Clinac Accelerators and Their Transmissions in Materials," in *Slac-Pub-7404*, no. SLAC-PUB-7404, 1997, pp. 1–5.

[59] A. Infantino, "FLUKA Monte Carlo Modelling of the CHARM Facility's Test Area: Update of the Radiation Field Assessment," Tech. Rep., 2017.

[60] R. Harboe-Sørensen, F.-X. Guerre, and A. Roseng, "Design, testing and calibration of a "Reference SEU monitor" system," in *8th European Conference on Radiation and Its Effects on Components and Systems, RADECS 2005.* IEEE, 2005, pp. B3––1.

[61] R. Harboe-Sørensen, C. Poivey, A. Zadeh, A. Keating, N. Fleurinck, K. Puimege, F.-X. Guerre, F. Lochon, M. Kaddour *et al.*, "Proba-II technology demonstration module in-flight data analysis," in *12th European Conference on Radiation and Its Effects on Components and Systems, RADECS 2011.* IEEE, 2011, pp. 581–586.

[62] R. Harboe-Sørensen, C. Poivey, N. Fleurinck, K. Puimege, A. Zadeh, F.-X. Guerre, F. Lochon, M. Kaddour, L. Li *et al.*, "The technology demonstration module on-board PROBA-II," *IEEE Trans. Nucl. Sci.*, vol. 58, no. 3, pp. 1001–1007, 2011.

[63] R. Harboe-Sørensen, C. Poivey, F.-X. Guerre, A. Roseng, F. Lochon, G. Berger, W. Hajdas, A. Virtanen, H. Kettunen, and S. Duzellier, "From the reference SEU monitor to the technology demonstration module on-board Proba-II," *IEEE Trans. Nucl. Sci.*, vol. 55, no. 6, pp. 3082–3087, 2008.

[64] R. G. Alía, B. Biskup, M. Brugger, M. Calviani, C. Poivey, K. Røed, F. Saigné, G. Spiezia, and F. Wrobel, "SEU measurements and Simulations in a mixed field environment," *IEEE Trans. Nucl. Sci.*, vol. 60, no. 4, pp. 2469–2476, 2013.

[65] R. G. Alía, M. Brugger, S. Danzeca, V. Ferlet-Cavrois, C. Poivey, K. Røed, F. Saigné, G. Spiezia, S. Uznanski, and F. Wrobel, "SEE Measurements and Simulations Using Mono-Energetic Gev-Energy Hadron Beams," *IEEE Trans. Nucl. Sci.*, vol. 60, no. 6, pp. 4142–4149, 2013.

[66] M. Tali and R. G. Alía, "Radiation test report ESA monitor and radFET at the CALIFES facility," CERN, Tech. Rep. EDMS Doc. No. 17427812016, 2016.

[67] R. G. Alía, E. W. Blackmore, M. Brugger, S. Danzeca, V. Ferlet-Cavrois, R. Gaillard, J. Mekki, C. Poivey, K. Røed *et al.*, "SEL cross section energy dependence impact on the high energy accelerator failure rate," *IEEE Trans. Nucl. Sci.*, vol. 61, no. 6, pp. 2936–2944, Oct. 2014.

[68] R. G. Alía, C. Bahamonde, S. Brandenburg, M. Brugger, E. Daly, V. Ferlet-Cavrois, R. Gaillard, S. Hoeffgen, A. Menicucci *et al.*, "Sub-LET threshold SEE cross section

dependency with ion energy," *IEEE Trans. Nucl. Sci.*, vol. 62, no. 6, pp. 2797–2806, Dec. 2015.

[69] M. A. Clemens, "Energy deposition mechanisms for proton- and neutron-induced single event upsets in modern electronic devices," Ph.D. dissertation, Vanderbilt University, 2012.

[70] R. G. Alia, "Radiation fields in high energy accelerators and their impact on single event effects," Ph.D. dissertation, PhD thesis, University of Montpellier, 2014. 17, 2014.

[71] J. R. Schwank, M. R. Shaneyfelt, J. Baggio, P. E. Dodd, J. A. Felix, V. Ferlet-Cavrois, P. Paillet, D. Lambert, F. W. Sexton *et al.*, "Effects of particle energy on proton-induced single-event latchup," in *IEEE Transactions on Nuclear Science*, vol. 52, no. 6, 2005, pp. 2622–2629.

[72] J. R. Schwank, M. R. Shaneyfelt, P. E. Dodd, J. A. Felix, J. Baggio, V. Ferlet-Cavrois, P. Paillet, K. A. Label, R. L. Pease *et al.*, "Hardness assurance test guideline for qualifying devices for use in proton environments," in *IEEE Transactions on Nuclear Science*, vol. 56, no. 4, 2009, pp. 2171–2178.

[73] B. Doucin, Y. Patin, J. P. Lochard, J. Beaucour, T. Carriere, D. Isabelle, J. Buisson, T. Corbiere, and T. Bion, "Characterization of proton interactions in electronic components," *IEEE Trans. Nucl. Sci.*, vol. 41, no. 3, pp. 593–600, 1994.

[74] R. G. Alía, M. Brugger, S. Danzeca, V. Ferlet-Cavrois, C. Poivey, K. Røed, F. Saigné, G. Spiezia, S. Uznanski, and F. Wrobel, "Energy dependence of tungsten-dominated SEL cross sections," *IEEE Trans. Nucl. Sci.*, vol. 61, no. 5, pp. 2718–2726, Sept. 2014.

[75] G. Tsiligiannis, S. Danzeca, R. Garcia-Alia, A. Infantino, A. Lesea, M. Brugger, A. Masi, S. Gilardoni, and F. Saigné, "Radiation Effects on Deep Sub-micron SRAM-based FPGAs under the CERN Mixed-Field Radiation Environment," *IEEE Transactions on Nuclear Science*, 2018.

[76] M. Cecchetto, "Impact of thermal and intermediate energy neutrons on the semiconductor memories for the CERN accelerators," Ph.D. dissertation, CERN, department of information engineering University of Padova, 2017.

[77] F. S. G. Tsiligiannis, S. Danzeca, R. Garcia-Alia, A. Infantino, A. Lesea, M. Brugger, A. Masi, S. Gilardoni, "Radiation Effects on Deep Sub-micron SRAM-based FPGAs for CERN applications," *IEEE Trans. Nucl. Sci. (submitted)*, vol. NA, 2017.

[78] D. G. Mavis and P. H. Eaton, "Soft error rate mitigation techniques for modern microcircuits," in *IEEE Int. Reliability Physics Symp.*, 2002, pp. 216–225.

[79] P. E. Dodd, A. R. Shaneyfelt, K. M. Horn, D. S. Walsh, G. L. Hash, T. A. Hill, B. L. Draper, J. R. Schwank, F. W. Sexton, and P. S. Winokur, "SEU-sensitive volumes in bulk and SOI SRAMs from frst-principles calculations and experiments," *IEEE Trans. Nucl. Sci.*, vol. 48, no. 6, pp. 1893–1903, 2001.

[80] R. Secondo, R. Alia, P. Peronnard, M. Brugger, A. Masi, S. Danzeca, A. Merlenghi, J. Vaillè, and L. Dusseau, "Analysis of SEL on commercial SRAM memories and mixed-field characterization of a latchup detection circuit for LEO space applications," *IEEE Transactions on Nuclear Science*, vol. 64, no. 8, pp. 2107–2114, 2017.

Publications

Publication I

M. Tali, R. Alia, M. Brugger, R. Corsini, W. Farabolini, V. Ferlet-Cavrois, A. Mohammadzadeh, G. Santin, and A. Virtanen, "High-energy Electron Induced SEUs and Jovian Environment Impact," *IEEE Trans. Nucl. Sci.*, vol. 64, no. 8, pp. 2016 – 2022, Aug 2017

High-energy Electron Induced SEUs and Jovian Environment Impact

Maris Tali, Rubén García Alía, Markus Brugger, Veronique Ferlet-Cavrois, Roberto Corsini, Wilfrid Farabolini, Ali Mohammadzadeh, Giovanni Santin, Ari Virtanen

***Abstract*—We present experimental evidence of electron induced upsets in a reference ESA SEU monitor, induced by a 200 MeV electron beam at the VESPER facility at CERN. Comparison of experimental cross-sections and simulated cross-sections are shown and the differences are analyzed. Possible secondary contributions to the upset rate by neutrons, flash effects and cumulative dose effects are discussed, showing that electronuclear reactions are the expected SEU mechanism. The ESA JUICE mission, to be launched in 2022, presents a challenging radiation environment due to the intense high-energy electron flux in the trapped radiation belts. Insight is given to the possible contribution of electrons to the overall upset rates in the Jovian radiation environment. Relative contributions of both typical electron and proton spectra created when the environmental spectra are transported through a typical spacecraft shielding are shown and the different mission phases are discussed.**

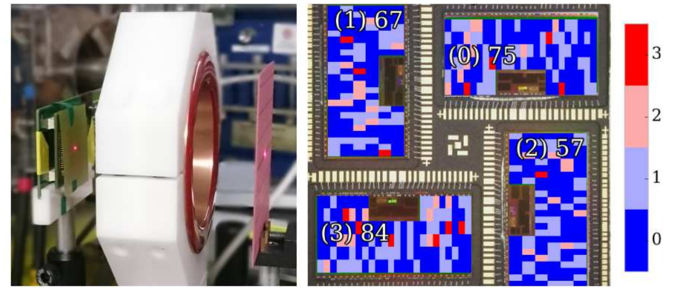

Fig. 1. LEFT) VESPER laser alignment system and the SEU monitor (left of picture) and the beam current transformer (middle) and the BTV (right of picture) at the DUT position RIGHT) VESPER commissioning run, distribution of SEUs in the ESA SEU monitor [8]

I. Introduction

In modern space applications, the feature size of the components has been steadily decreasing, driven by the ever-increasing need for larger storage and low power. These new technologies have been shown to be sensitive to direct ionization from singly charged particles, including protons, muons and even electrons [1] [2] [3], in addition to being sensitive to indirect ionisation events [4]. Moreover, similarly to traditional proton and neutron induced SEEs (Single Event Effects), electrons are also capable of causing these effects via electronuclear interactions [4]. Currently electron-induced direct and indirect ionization effects are not taken into account with commonly used error rate prediction tools, such as CREME96 [5], which estimate the direct-ionisation induced SEEs.

In this paper, irradiation with 200 MeV electrons at the VESPER (Very energetic Electronic facility for Space Planetary Exploration in harsh Radiation environments) facility at CERN (European Organization for Nuclear Research) is shown to cause single event effects in even a relatively large node size of $0.25\,\mu\mathrm{m}$ and with a relatively large LET (Linear Energy Transfer) threshold ($\sim 3\,\mathrm{MeVcm^2/mg}$). The obtained cross-section value for the electron induced upsets is several orders of magnitude lower than that obtained during proton or neutron irradiation. The cause for this difference is the associated nuclear reaction cross-sections. The experimental results are validated through series of simulations for an equivalent geometry for the ESA (European Space Agency) SEU (Single Event Upset) monitor. Possible secondary contributions to the upsets are discussed and demonstrated to be insignificant.

The planned JUICE (Jupiter ICy moon Explorer) mission by ESA, which will experience harsh trapped particle environments, has shown the need for better understanding of non-direct ionization events due to the intense and high-energetic trapped electron spectra. The space radiation environment presents a challenge for all electronics sent into space. This is especially true for the JUICE mission, which has to endure the harsh Jupiter radiation environment. The estimation of the error rates in electronics is an essential part of mission planning, as these can have serious consequences for the mission [6]. Therefore, the JUICE space environment specification has been developed. The specification is based on the ECSS (The European Co-operation for Space Standardization) Space Environment Standard [7]. This paper estimates the relative contributions of the trapped electron and proton induced upsets in a standard spacecraft shielding and discusses the effect these results can have on smaller technology sizes and upset rate prediction for the mission.

M. Tali, R. G. Alía, M. Brugger, R.Corsini and W. Farabolini are with CERN, CH-1211 Geneve 23, Switzerland. (e-mail: maris.tali@cern.ch)

M. Tali, V. Ferlet-Cavrois, G. Santini and A. Zadeh are with the European Space Agency, ESTEC, 2200 AG Noordwijk, The Netherlands.

M. Tali and A. Virtanen are with the Department of Physics, Accelerator Laboratory, University of Jyväskylä, FI-40014, Jyväskylä, Finland

This work was supported by the CERN/ESA collaboration, the VESPER, CHARM and R2E groups at CERN and the European Space Agency (ESA/ESTEC Contract No. 4000115379/15/NL/MH/GM), and the Academy of Finland under the Finnish Centre of Excellence Programme 2012-2017 (Project No. 2513553, Nuclear and Accelerator Based Physics).

II. The VESPER Facility

A. Facility Description

The ESA SEU monitor is a SEU-based particle detector, which has been calibrated in a broad range of test facilities

and can therefore be used as a reference in test conditions for which it has been previously characterized [9]. The layout of the memories used in the SEU monitor and a distribution of the upsets recorded during one of the runs can be seen in Fig. 1. The measurements took place in VESPER, which is a part of the CLIC (Compact Linear Collider) Test Facility CTF3 at CERN. The accelerator used in the test campaign is an electron linac, which provides a multi-purpose beam for accelerator technology tests with an energy up to 200 MeV [10]. After improvements to the beamline and beam monitoring, as of March 2016, the maximum beam size achieved was $4\,\mathrm{cm} \times 3.5\,\mathrm{cm}$ FWHM, which completely covers the sensitive area of our detector, which is $2\,\mathrm{cm} \times 2\,\mathrm{cm}$ [11]. In addition to this, a laser alignment system, which can be seen in Fig. 1, and a movable stage were installed at the test position for precise DUT alignment and to minimize the uncertainties related to beam intensity estimations.

B. *Facility Dosimetry*

The test position has a dedicated active dosimetry system. A BCM (beam current monitor) is installed directly downstream of the BTV (beam TV) screen used for beam profile monitoring at the DUT (device under test) position. The beam current transformer at the DUT position have been cross-calibrated using parallel beam measurements with a Faraday cup, which can be seen on the right in Fig. 2.

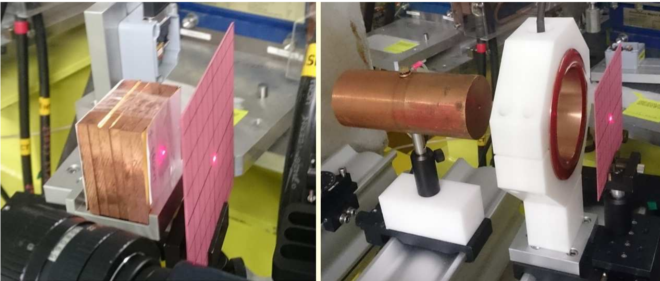

Fig. 2. LEFT) Gold activation experiment RIGHT) From left to right: Faraday cup, beam current transformer and the beam TV screen

A cross-calibration of the beam intensity, using dose measurements with a RadFET and a gold activation experiment, which can be seen on the left in Fig. 2, is currently ongoing. In addition, GafChromic film was used to measure the beam profile.

The gold foil activation measurement is based on an activation study performed at Pohang using a $2.5\,\mathrm{GeV}$ electron beam [12]. In the experiment the beam intensity was measured using the irradiation of a stack of copper blocks and gold foils . The mechanism of the decay is the production of ^{196}Au through the ^{197}Au(γ, n) reaction, or more precisely photon induced neutron emission. A detailed experimental cross-section exists for this reaction and is used in FLUKA [13] [14], a Monte-Carlo particle physics simulation package. The emission of decay photons from the ^{197}Au isotope were measured using a germanium detector, the results were compared to a FLUKA activation simulation. The absolute difference between the measurement and simulation was included as an error contribution to the experimental result [15] [8].

The GafChromic film was attached to the beam TV during the experiment and a densitometry measurement was performed after the irradiation to determine the beam intensity. The measurement serves as an additional check for the beam profile obtained with the beam TV and the RadFET.

III. Upsets induced in the ESA SEU monitor by 200 MeV electrons

A. *Experimental results*

The ESA SEU monitor was attached to a movable stage and the sensitive area was aligned using the laser alignment system. For the setup, a cable for the power supply connection and an Ethernet cable for the data acquisition connection to the control room were used. The ESA SEU monitor was placed $1\,\mathrm{cm}$ behind a BTV screen, a picture of the setup can be seen in Fig. 1.

Measurements were taken before the start of the irradiation to ensure that the background events were not causing upsets; no upsets were seen without the beam. Then, the beam was started and at the end of the irradiation period, the number of upsets was recorded together with their location address.

During the runs, the beam was well-aligned on the monitor, therefore uncertainty due to misalignment was ignored. The final number of SEUs at the end of each run, which was included in the cross-section calculation, was about 60 counts per die. Therefore, an average error due to count statistics was calculated to be 12.5%. In addition, an uncertainty on the dosimetry is conservatively estimated to be 25%. The total 2σ uncertainty is therefore estimated to be 30%.

The cross-section was calculated with the usual definition

$$\sigma = \frac{\#\ \mathrm{SEUs}}{\phi \times \#\ \mathrm{bits}} \tag{1}$$

where ϕ is the fluence, the size of each die of the ESA SEU monitor is $4\,\mathrm{Mbit}$. The average flux over the sensitive area was $4.54 \times 10^{8}\,\mathrm{e}-/\mathrm{cm}^2/\mathrm{s}$ and total fluence for the run was $9.95 \times 10^{12}\,\mathrm{e}-/\mathrm{cm}^2$. The dose deposited on the device was $3.19\,\mathrm{kGy(Si)}$. Using equation 1 the average cross-section was found to be $(7.17 \pm 2.26) \times 10^{-18}\,\mathrm{cm}^2$.

An additional run where a $5\,\mathrm{mm}$ copper block was placed directly in front of the ESA SEU monitor was made. The copper block enhances the photon production through bremsstrahlung, which in turn makes it possible to assess the contribution of photons to the cross-section. A simulation of the beam line with the spectra scored in a 2×2 cm thin silicon slab with and without the added copper slab shows the clear enhancement of the photon yield, as discussed further in section IV-D. The average cross-section for the photon runs was $(3.62 \pm 0.53) \times 10^{-17}\,\mathrm{cm}^2$. The cross-section increases by a factor of 5 with the addition of the $5\,\mathrm{mm}$ copper plate.

IV. Validation of experimental results

A. *FLUKA energy deposition simulations*

To be able to estimate the cross-section of the electron induced SEUs, a FLUKA simulation to calculate the energy

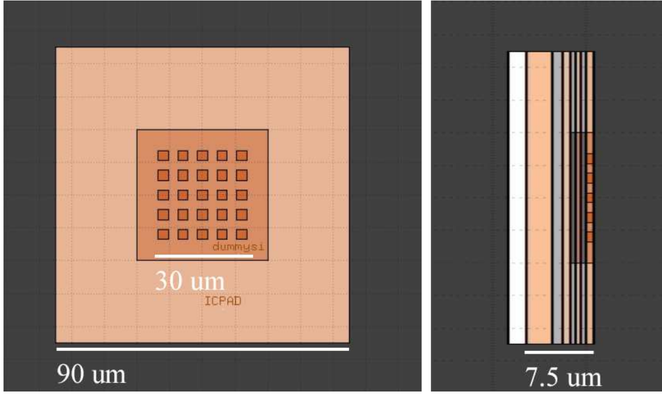

Fig. 3. FLUKA geometry for energy deposition simulations for the ESA SEU monitor [8]

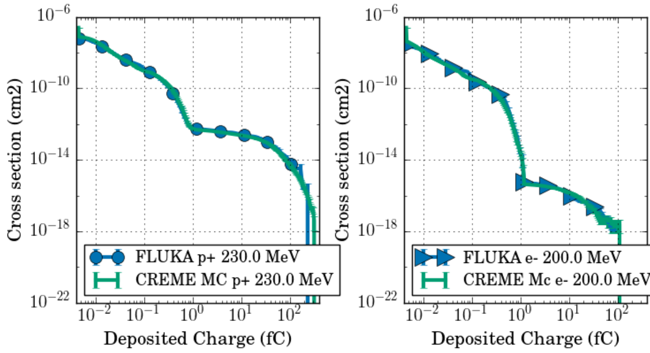

Fig. 4. Energy deposition for the ESA SEU monitor. Comparison between CREME MC and FLUKA [8]

deposition simulation in a simple ESA SEU monitor approximation geometry was performed. The geometry is a stack of aluminium and silicon dioxide layers, with the bottom layer representing the active silicon, which also contains cubes of sensitive volumes for energy deposition scoring, which can be seen in Fig. 3. The sensitive volumes were replicated 25 times to compensate for edge effects, for the simulation to give a more accurate estimation of SEUs caused by secondary particles and to enhance the statistical significance of indirectly ionizing events. A single sensitive volume is a cube with a $3\,\mu m \times 3\,\mu m$ sides, the width of the sensitive volume cluster is $30\,\mu m$. The target was shot with proton, electron, photon and neutron beams at different energies to estimate the single-event cross-sections, which can be seen in Fig. 5. The reverse integral cross-section is obtained by integrating the energy scored in the sensitive volumes in the direction of decreasing charge. Photons are included in the simulation due to the large associated fluxes in high-energy electron beams as a result of the bremsstrahlung in their passage through matter.

As a comparison to the FLUKA simulation, an equivalent simulation was also done using CREME-MC [16], which is a Geant4 based tool for SEE rate predictions. The geometry used was similar but with a single sensitive volume of $3\,\mu m \times 3\,\mu m \times 0.5\,\mu m$, the energy deposition was scored and reported as a cross-section, which can be seen in Fig. 4. A comparison of energy generated in the sensitive volumes scored from shooting the target with a $230\,\mathrm{MeV}$ proton and $200\,\mathrm{MeV}$ electron beam can be seen in Fig. 5. As can be noticed, though with a much lower associated probability, nuclear reaction induced energy deposition events from electrons and photons follow a similar distribution as those for protons and neutrons, and can therefore be considered capable of inducing similar effects.

To further study the recoil production from the electron and silicon interactions, several FLUKA simulations were run and comparisons were made with photons and neutrons.

B. *Electron induced SEU mechanisms*

Single event effects caused by electrons can be attributed to recoils produced by the interaction of electrons and photons with the silicon nuclei in or near the sensitive volumes [4]. This is similar to the mechanism through which protons cause single event effects [17], however the probability of such events occurring due to electrons is about 3 magnitudes lower as can be seen in Fig. 5. Here, one can observe the similar shape but lower cross-section of the energy deposition curve of electrons compared to protons.

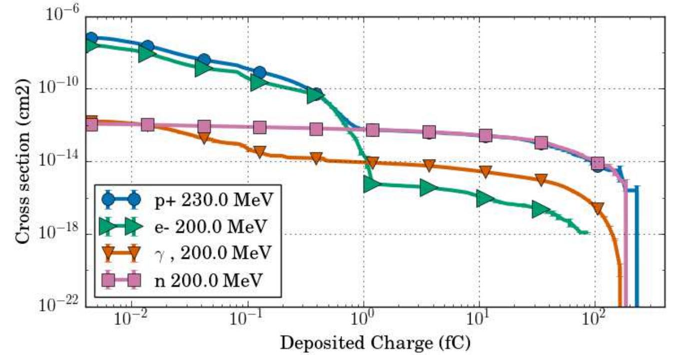

Fig. 5. Reverse integral energy deposition estimation for the ESA SEU monitor equivalent geometry in FLUKA. [8]

In addition, the inelastic interaction cross-section was simulated using FLUKA, which clearly shows this higher probability for proton interactions compared to electrons and photons in Fig. 6. One can also note the great dipole resonance at around $20\,\mathrm{MeV}$ for photons. This resonance contributes to the sudden increase in SEU cross-section for photons around this energy range, as is discussed further in section IV-C.

To further study these interactions, several FLUKA runs were made using a $200\,\mathrm{MeV}$ electron, photon and proton beam to compare the LET, seen in Fig. 9, and charge, seen in Fig. 7, of all recoils created. In addition, simulations to compare the kinetic energy, seen in Fig. 8, and scattering angle, seen in Fig. 10 of only the heavier recoils ($Z > 9$) were performed. All of the resulting simulations were normalized to the inelastic interaction cross-section for a direct comparison between the particles.

The simulations showed very similar distribution of charge and kinetic energy for photons and protons, whilst the electron value for electrons was about 1 magnitude smaller for larger

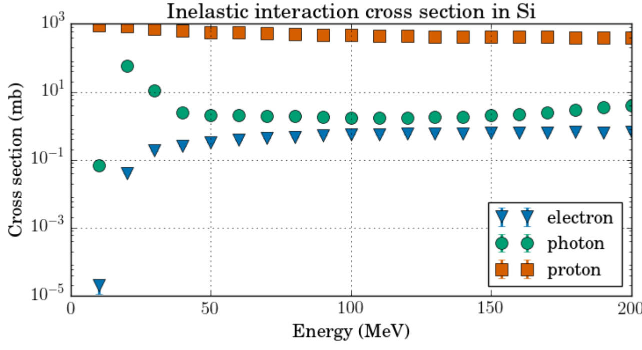

Fig. 6. Inelastic interaction cross-section for photons, neutrons and electrons interacting with a Si target

energies. The same result was seen for the LET distribution, here the highest LET produced by protons and photons is about $15\,\mathrm{MeVcm^2/mg}$ whilst for electron it's about $14\,\mathrm{MeVcm^2/mg}$. The distribution of the scattering angles is much more uniform for electrons, whilst protons and neutrons have mostly smaller scattering angles. The maximum charge of the recoils is also similarly lower for electrons.

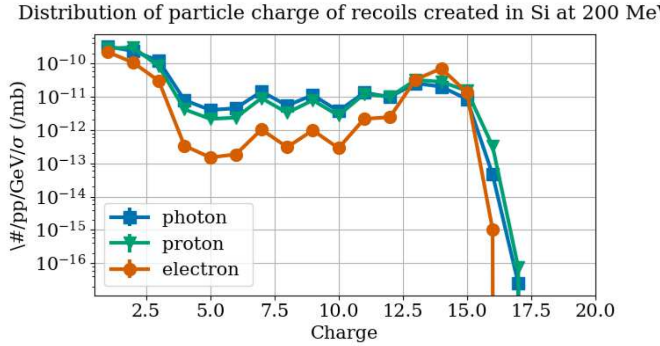

Fig. 7. Distribution of charge of recoils from electron beam interaction with silicon

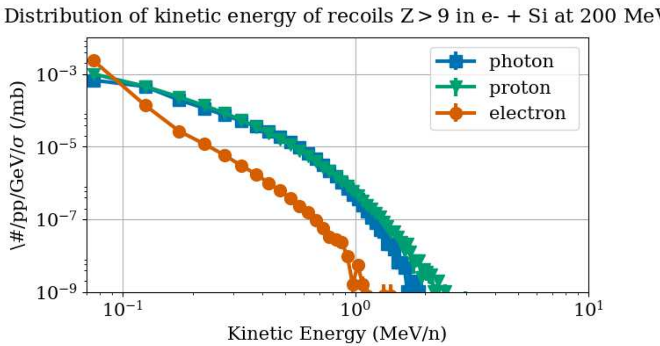

Fig. 8. Distribution of kinetic energy of recoils from electron beam interaction with silicon

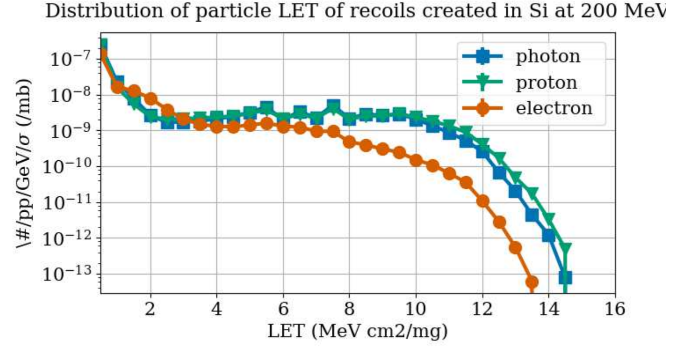

Fig. 9. Distribution of LET of recoils from electron beam interaction with silicon

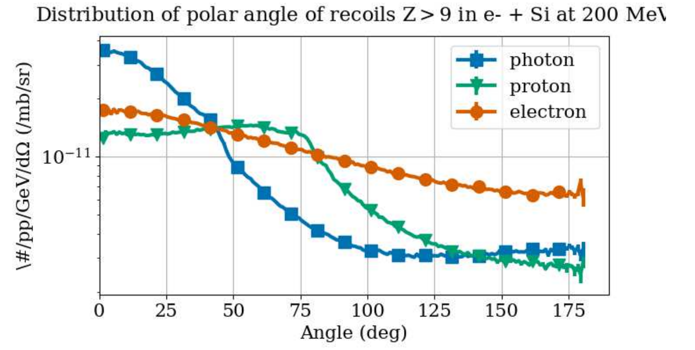

Fig. 10. Distribution of angle of recoils from electron beam interaction with silicon

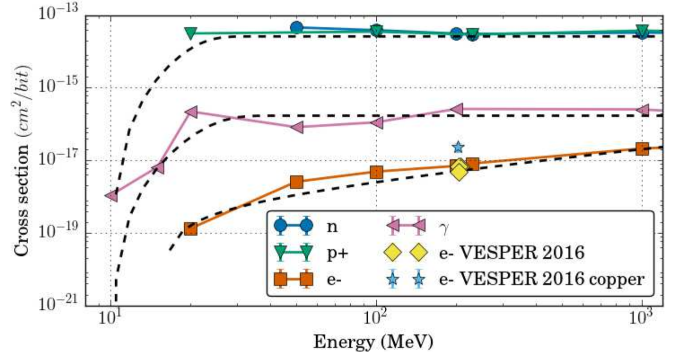

Fig. 11. Simulated cross-sections for the ESA SEU monitor. Measurements are shown, run with copper plate marked. Parameters of the Weibull fits can be seen in Table I. Weibull fits are shown with stippled lines. [8]

C. *ESA SEU monitor cross-section estimation*

To retrieve the simulated cross-sections for the ESA SEU monitor, the experimental heavy ion Weibull fit for the monitor was folded with the FLUKA energy deposition simulations [18]. The approach is based on the assumption that the heavy ion response of the component represents the SEU probability as a function of the deposited energy (i.e. LET times SV thickness). Therefore, the latter can be used in combination with the simulated probability of a particle depositing a given amount of energy through a nuclear interaction to retrieve the

Particle	XSsat (cm2/bit)	Eth(MeV)	W (MeV)	s
e-	8.08×10^{-17}	16	3946	0.9
p+	2.6×10^{-14}	3	18.2	1.67
n	2.6×10^{-14}	10	11.6	3.14
γ	1.76×10^{-16}	10	30	3

TABLE I
WEIBULL PARAMETERS FOR THE ESA SEU MONITOR

associated SEU cross section of that particle and energy. The method for the folding the spectra and the Weibull fits as a function of energy is written as

$$\sigma_p(E_p) = \int \sigma_{HI}(E_d) p(E_p, E_d)\ dE_d \tag{2}$$

where $\sigma_p(E_p)$ is the SEU cross-section for each particle, σ_{HI} is the SEU monitor heavy ion cross-section, $p(E_p, E_d)$ is the probability of depositing a charge E_d in the sensitive volumes in the ESA SEU monitor RPP model [19] [20], and correspond to the differential distributions shown in Fig. 5. The variables for the heavy-ion Weibull fit are: saturation threshold of $3.72 \times 10^{-8}\,\mathrm{cm^2/bit}$, a LET threshold of $3.0\,\mathrm{MeVcm^2/mg}$, W of $21.78\,\mathrm{MeVcm^2/mg}$ and s of 0.66 [21].

In the energy deposition simulations, a clear distinction between the direct and indirect energy deposition can be seen as a sharp drop in the deposited energy, as seen in Fig. 5. One can also see that there is a difference of three orders of magnitudes between the electron and proton indirect ionisation, this already indicates that the same difference will be seen in the respective cross-sections. We fitted a Weibull cumulative distribution function to the simulated cross-section values. The cross-section and Weibull fits are shown in Fig. 11, which confirms the expected order of magnitude differences. The details of the Weibull fits are listed in Table I.

D. Analysis of mechanisms for the observed errors

The first possible explanation to an alternative cause for the SEUs observed during the irradiation is the possibility that more than one electron hit the sensitive area of the device and the cumulative charge built up in the sensitive are caused the upset [4]. To evaluate this, the probability of two or more electrons causing an upset in the same cell during the relaxation time of a previous upset is found, this can be calculated as [1]

$$Pr(X_1||X_2) = (\phi A_{cell} \tau)^2 \tag{3}$$

where ϕ is the incident flux obtained through FLUKA of the simulations of the spectra of the beam at the DUT position, A_{cell} is the area of the sensitive area and τ is the relaxation or response time for an upset event. As described in [22] and [23], the most appropriate time for the ESA monitor technology size would be $100\,\mathrm{ps}$. The probability for the ESA SEU monitor is then $(2 \times 10^{14}\,\mathrm{e/cm/s} \cdot 10\,\mathrm{\mu m^2} \cdot 100\,\mathrm{ps})^2 = 4 \times 10^{-6}$. In addition, even several electrons depositing the maximum possible energy through direct ionization would not be enough to reach the LET threshold.

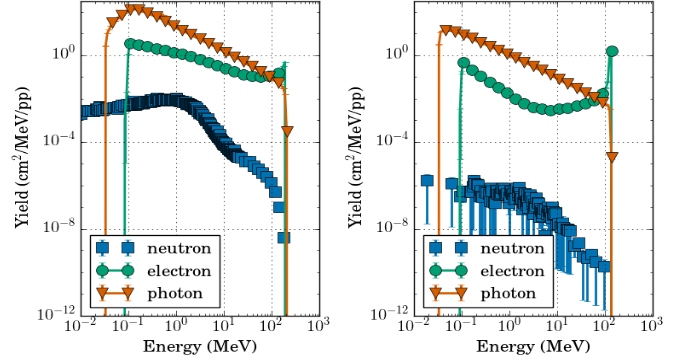

Fig. 12. Simulated spectra at the VESPER beamline DUT position: left) with copper block added directly in front of detector, right) without copper block

As further proof, an experiment with varying flux should therefore be performed in the future. To prove that the upsets are not caused by coinciding electron hits to the sensitive area, the cross-section would have to be independent of the flux, as shown in [4].

Another possible contribution to the upset cross-section are neutrons generated through electro- and photonuclear interaction with beamline elements upstream of the test position. To assess the contribution of neutrons in the spectra at the DUT position, a simple FLUKA simulation was set up with a model of the beam line. Only the elements directly in the beam path were included in the simulation: the stainless-steel exit window of the beam pipe and the chromox (chromium oxide) BTV screen used to monitor the beam position. The thicknesses of the BTV is $1.1\,\mathrm{mm}$ and it is located $10\,\mathrm{cm}$ upstream of the target, the thickness of the stainless-steel window is $2\,\mathrm{mm}$ and it is located $45\,\mathrm{cm}$ upstream of the target. The resulting spectra can be seen in Fig. 12. The neutron yield is on the order of eight magnitudes lower than that of electrons and photons.

To assess the relative contribution to the SEU cross-section between neutrons and electrons, the spectra retrieved from the beam line simulations has been folded with the cross-section curves retrieved from the energy deposition simulations. The resulting cross-section for neutrons is $6.69 \times 10^{-22} \pm 7.87 \times 10^{-23}\mathrm{cm}^2$, for photons $1.43 \times 10^{-17} \pm 1.41 \times 10^{-20}\mathrm{cm}^2$ and for electrons $4.93 \times 10^{-18} \pm 1.35 \times 10^{-21}\mathrm{cm}^2$. The electron contribution is 4 magnitudes larger than that of the neutrons. Therefore, the effect of the neutrons generated by the beam line is negligible.

An additional simulation where a $0.5\,\mathrm{cm}$ copper block was placed directly in front of the ESA SEU monitor was made. This is for the purpose of assessing the contribution of photons to the cross-section. A simulation of the beam line with the spectra scored in a 2×2 cm thin silicon slab with and without the added copper slab shows the clear enhancement of the photon yield in Fig. 12. The resulting cross-section for neutrons is $1.77 \times 10^{-18} \pm 7.54 \times 10^{-22}\mathrm{cm}^2$, for photons $9.92 \times 10^{-17} \pm 4.7 \times 10^{-20}\mathrm{cm}^2$ and for electrons $1.77 \times 10^{-18} \pm 7.54 \times 10^{-22}\mathrm{cm}^2$.

As described in [24], possible additional mechanisms that have the potential to produce SEUs are the secondary ions

Phase	Description	Duration (days)
Phase 0	Interplanetary transfer	2711
Phase 1	Transfer to Europa	458
Phase 2	Europa flybys	38
Phase 3	Jupiter high latitude phase with Callisto	248
Phase 4	Transfer to Ganymede	311
Phase 5a	Ganymede orbit insertion, elliptic orbits, and 5000 km circular orbit	152
Phase 5b	Ganymede 500 km altitude circular orbit	103
Phase 5c	Ganymede 200 km altitude circular orbit	30

TABLE II
DESCRIPTION OF JUICE MISSION PHASES

produced by elastic electron–nuclei scattering. However, as this is unlikely it is therefore ruled out as a contribution.

V. EFFECT OF ELECTRON SPECTRA IN THE JOVIAN ENVIRONMENT

A. JUICE mission environment

The space radiation environment presents a challenge for all electronics sent into space. This is especially true for the JUICE mission, which has to endure the harsh Jupiter radiation environment. The estimation of the error rates in electronics is an essential part of mission planning, as these can have serious consequences for the mission [6] Therefore, the JUICE space environment specification has been developed. The specification is based on the ECSS Space Environment Standard [7]. In general, the JUICE energetic radiation environment consists of charged particles trapped by the Jupiter magnetic field, solar protons and galactic cosmic rays. The main contribution to the radiation dose will be from the radiation belts and mainly from the high-energy electrons. The JUICE mission consists of 5 phases, which are described in Table II, the radiation contribution from each of these phases has been estimated and the total integral fluence from trapped electrons and protons can be seen in Fig. 13 [6].

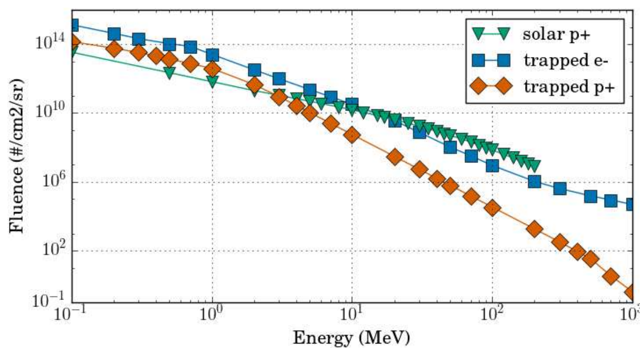

Fig. 13. JUICE mission, integral fluence of trapped protons, electrons and solar protons for the total 5 mission phases

B. SEU rate in the Jovian atmosphere

When evaluating radiation effects, it is often the secondary radiation from the shielding that is important. Electron induced Bremsstrahlung, caused by the slowing down by scattering off atomic nuclei, is considered a significant secondary source [6].

To estimate the spectra of particles created by the shielding, simulations were run using GRAS [25], which is a Geant4 based radiation analysis package targeting space applications. The trapped electron and proton spectra were transported through shielding of $20\,\mathrm{mm}$ of aluminium and tantalum shielding of equal weights. The effect of the shielding in creating secondary particles can clearly be seen in Fig. 14, where trapped proton and electron spectra have been transported through the shielding.

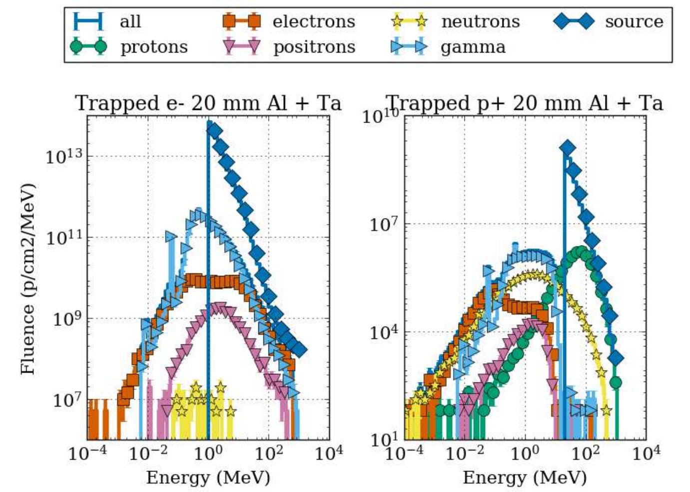

Fig. 14. JUICE mission, spectra transported through $20\,\mathrm{mm}$ aluminium and tantalum shielding

To estimate the SEU rate inside the spacecraft the spectrum of the secondary radiation is folded with the Weibull response of the ESA SEU monitor and multiplied by the number of bits in the whole device $(16\,\mathrm{Mbit})$. The Weibull fits for each particle group were discussed in section IV-C. The resulting estimation for the cross-section contribution for each particle can be seen in Fig. 15. To evaluate the contribution of each particle group to the total error rate, only the trapped radiation was considered. The result for the combined contributions from trapped electron and proton spectra can be seen in the rightmost plot in Fig. 15. The upset rate generated by trapped electrons is 3.08 ± 0.06 SEU/mission, 47.88 ± 1.2 SEU/mission for photons, 7.03 ± 0.013 SEU/mission for protons and 0.41 ± 0.003 SEU/mission for neutrons. The neutron and proton contribution to the total upset rate are dominated by the trapped proton generated events, while the electrons and photons are clearly dominated by the trapped electron induced events.

VI. SUMMARY AND CONCLUSIONS

In conclusion, as shown with the experimental results and the theoretical simulations, electrons are able to cause single event effects in even a relatively old technology. The nuclear

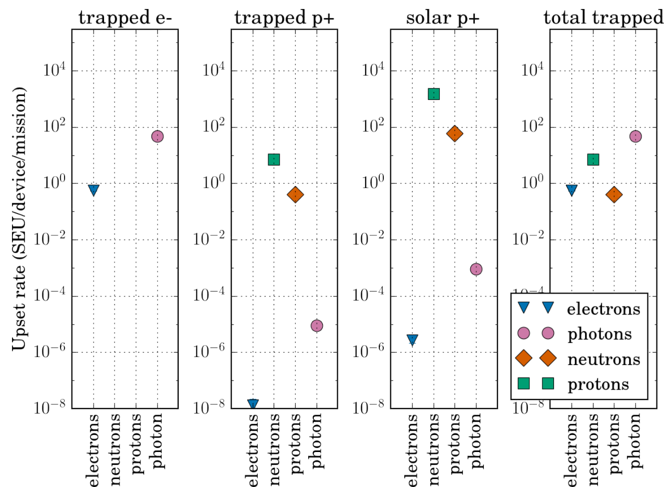

Fig. 15. Cross-section contributions per the whole ESA SEU monitor (16 Mbit) for the complete JUICE mission (total mission duration is 4051 days) from trapped protons and electrons and solar protons transported through shielding for each electrons, positrons, protons and neutrons

fragments responsible for the energy deposition, though generated with a much lower probability, are similar to those produced in well-known proton and neutron interactions

Furthermore, modern technologies used in critical applications in both space and high energy physics environments are down to tens of nanometers, which is several orders of magnitude smaller than of the ESA SEU monitor. These devices have a much lower critical energy and are therefore also more susceptible to upsets, including the indirect ionization events caused by electrons. As can be seen from the ESA SEU monitor energy deposition simulations, the cross-section for the indirect ionization events from electrons is dependent on incident particle energy. Therefore, there is a strong correlation between the smaller feature size and the overall cross-section contribution of electron induced upsets.

Despite the lower associated probability for interactions, the large electron fluxes in the trapped radiation belts in the Jovian environment relative to protons result in the photon fluxes produced when the particles pass through the shielding material, which in turn contributes to the overall SEU rate. In addition, considering that the experimental results were obtained with the ESA SEU monitor, which uses 0.25 μm transistor sizes, and that the technologies to be used in the JUICE mission will have much smaller technology sizes, electrons will have a sizable contribution to the SEU rate.

References

[1] M. P. King, R. A. Reed, R. A. Weller, M. H. Mendenhall, R. D. Schrimpf, B. D. Sierawski, A. L. Sternberg, B. Narasimham, J. K. Wang, E. Pitta, and Others, "Electron-induced single-event upsets in static random access memory," *IEEE Trans. Nucl. Sci.*, vol. 60, no. 6, pp. 4122–4129, 2013.

[2] B. D. Sierawski, J. A. Pellish, R. A. Reed, R. D. Schrimpf, K. M. Warren, R. A. Weller, M. H. Mendenhall, J. D. Black, A. D. Tipton, M. A. Xapsos, and Others, "Impact of low-energy proton induced upsets on test methods and rate predictions," *IEEE Trans. Nucl. Sci.*, vol. 56, no. 6, pp. 3085–3092, 2009.

[3] B. D. Sierawski, M. H. Mendenhall, R. A. Reed, M. A. Clemens, R. A. Weller, R. D. Schrimpf, E. W. Blackmore, M. Trinczek, B. Hitti, J. A. Pellish, and Others, "Muon-induced single event upsets in deep-submicron technology," *IEEE Trans. Nucl. Sci.*, vol. 57, no. 6, pp. 3273–3278, 2010.

[4] M. J. Gadlage, A. H. Roach, A. R. Duncan, M. W. Savage, and M. J. Kay, "Electron-induced single-event upsets in 45-nm and 28-nm bulk CMOS SRAM-based FPGAs operating at nominal voltage," *IEEE Trans. Nucl. Sci.*, vol. 62, no. 6, pp. 2717–2724, 2015.

[5] A. J. Tylka, J. H. Adams Jr, P. R. Boberg, B. Brownstein, W. F. Dietrich, E. O. Flueckiger, E. L. Petersen, M. A. Shea, D. F. Smart, and E. C. Smith, "CREME96: A revision of the cosmic ray effects on micro-electronics code," *IEEE Trans. Nucl. Sci.*, vol. 44, no. 6, pp. 2150–2160, 1997.

[6] JUICE Team, "JUICE environment specification," ESTEC/ESA, Noordwijk, Netherlands, Tech. Rep., 2015.

[7] ECSS Secretariat, "ECSS-E-ST-10-04C space environment standard," 2008.

[8] M. Tali, R. G. Alía, M. Brugger, V. Ferlet-Cavrois, R. Corsini, W. Farabolini, G. Santin, A. Virtainen, and A. Zadeh, "Mono-energetic electron induced single-event effects at the VESPER facility," in *Eur. Conf. Radiat. Its Eff. Components Syst. RADECS 2016*, no. C16-09-19.6, 2016.

[9] R. Harboe-Sørensen, F.-X. Guerre, and A. Roseng, "Design, testing and calibration of a "Reference SEU monitor" system," in *8th Eur. Conf. Radiat. Its Eff. Components Syst. RADECS 2005*. IEEE, 2005, pp. B3—-1.

[10] J. L. N. Quirante, R. Corsini, A. Grudiev, T. Lefevre, S. Mazzoni, R. Pan, F. Tecker, W. Farabolini, F. Peauger, D. Gamba, and Others, "CALIFES: A multi-purpose electron beam for accelerator technology tests," in *Proc. LINAC14*, 2014.

[11] W. Farabolini. (2016, jan) Irradiation tests in the CALIFES beam line - beam conditions. CLIC Workshop, [Online] Available: https://indico.cern.ch/event/449801/timetable/#20160119.detailed.

[12] M. Brugger, A. Errahhaoui, M. Kim, H.-S. Lee, S. Roesler, and H. Vincke, "Activation benchmark study at a 2.5 GeV electron accelerator," *Prog. Nucl. Sci. Tech.*, vol. 4, pp. 363–366, 2014.

[13] A. Ferrari, P. R. Sala, A. Fasso, J. Ranft, A. Ferrari, P. R. Sala, A. Fassò, and J. Ranft, "FLUKA: A multi-particle transport code," in *CERN 2005-10 (2005), INFN/TC 05/11, SLAC-R-773*, 2005.

[14] T. T. Böhlen, F. Cerutti, M. P. W. Chin, A. Fasso, A. Ferrari, P. G. Ortega, A. Mairani, P. R. Sala, G. Smirnov, and V. Vlachoudis, "The FLUKA code: developments and challenges for high energy and medical applications," *Nucl. Data Sheets*, vol. 120, pp. 211–214, 2014.

[15] M. Tali and R. G. Alía, "Radiation test report ESA monitor and radFET at the CALIFES facility," CERN, Tech. Rep. EDMS Doc. No. 17427812016, 2016.

[16] B. D. Sierawski, M. H. Mendenhall, R. A. Weller, R. A. Reed, J. H. Adams, J. W. Watts, and A. F. Barghouty, "CRÈME-MC: A physics-based single event effects tool," in *Nucl. Sci. Symp. Conf. Rec.* IEEE, 2010, pp. 1258–1261.

[17] M. A. Clemens, "Energy deposition mechanisms for proton- and neutron-induced single event upsets in modern electronic devices," Ph.D. dissertation, Vanderbilt University, 2012.

[18] R. G. Alía, C. Bahamonde, S. Brandenburg, M. Brugger, E. Daly, V. Ferlet-Cavrois, R. Gaillard, S. Hoeffgen, A. Menicucci, S. Metzger, and Others, "Sub-LET threshold SEE cross section dependency with ion energy," *IEEE Trans. Nucl. Sci.*, vol. 62, no. 6, pp. 2797–2806, 2015.

[19] R. G. Alía, M. Brugger, S. Danzeca, V. Ferlet-Cavrois, C. Poivey, K. Røed, F. Saigné, G. Spiezia, S. Uznanski, and F. Wrobel, "Energy dependence of tungsten-dominated SEL cross sections," *IEEE Trans. Nucl. Sci.*, vol. 61, no. 5, pp. 2718–2726, 2014.

[20] B. Doucin, Y. Patin, J. P. Lochard, J. Beaucour, T. Carriere, D. Isabelle, J. Buisson, T. Corbiere, and T. Bion, "Characterization of proton interactions in electronic components," *IEEE Trans. Nucl. Sci.*, vol. 41, no. 3, pp. 593–600, 1994.

[21] R. G. Alía, B. Biskup, M. Brugger, M. Calviani, C. Poivey, K. Røed, F. Saigné, G. Spiezia, and F. Wrobel, "SEU measurements and simulations in a mixed field environment," *IEEE Trans. Nucl. Sci.*, vol. 60, no. 4, pp. 2469–2476, 2013.

[22] D. G. Mavis and P. H. Eaton, "Soft error rate mitigation techniques for modern microcircuits," in *IEEE Int. Reliab. Phys. Symp.*, 2002, pp. 216–225.

[23] P. E. Dodd, A. R. Shaneyfelt, K. M. Horn, D. S. Walsh, G. L. Hash, T. A. Hill, B. L. Draper, J. R. Schwank, F. W. Sexton, and P. S. Winokur, "SEU-sensitive volumes in bulk and SOI SRAMs from frst-principles calculations and experiments," *IEEE Trans. Nucl. Sci.*, vol. 48, no. 6, pp. 1893–1903, 2001.

[24] C. Inguimbert, R. Ecoffet, and D. Falguère, "Electron induced SEUs: microdosimetry in nanometric volumes," *IEEE Trans. Nucl. Sci.*, vol. 62, no. 6, pp. 2846–2852, 2015.

[25] G. Santin, V. Ivanchenko, H. Evans, P. Nieminen, and E. Daly, "GRAS: A general-purpose 3-D modular simulation tool for space environment effects analysis," *IEEE Trans. Nucl. Sci.*, vol. 52, no. 6, pp. 2294–2299, 2005.

Publication II

M. Tali, R. Garcia Alia, M. Brugger, V. Ferlet-Cavrois, R. Corsini, W. Farabolini, A. Javanainen, M. Kastriotou, H. Kettunen *et al.*, “Mechanisms of Electron-Induced Single-Event Upsets in Medical and Experimental Linacs,” *IEEE Trans. on Nucl. Sci.*, vol. 65, no. 8, pp. 1715–1723, Jun 2018

Mechanisms of Electron-Induced Single Event Upsets in Medical and Experimental Linacs

Maris Tali, Rubén García Alía, Markus Brugger, Veronique Ferlet-Cavrois, Roberto Corsini, Wilfrid Farabolini, Arto Javainen, Maria Kastriotou, Heikki Kettunen, Giovanni Santin, Cesar Boatella Polo, Georgios Tsiligiannis, Salvatore Danzeca, and Ari Virtanen

***Abstract*—In this paper we perform an in-depth analysis of the single-event effects observed during testing at medical electron linacs and an experimental high-energy electron linac. For electron irradiations the medical linacs are most commonly used due to their availability and flexibility. Whereas previous efforts were made to characterize the cross-sections at higher energies, where the nuclear interaction cross-section is higher, the focus on this paper is on the complete overview of relevant electron energies. Irradiations at an electron linac were made with two different devices, with a large difference in feature size. The irradiations at an experimental linac were performed with varying energies and intensities to omit other possible effects.**

I. Introduction

In modern space applications, the feature size of components has been steadily decreasing, driven by the ever-increasing need for larger storage and lower power. These new technologies have been shown to be sensitive to direct ionization from singly charged particles, including protons, muons and even electrons [1] [2] [3] as well as to being sensitive to indirect ionization events [4]. Moreover, similarly to traditional proton and neutron induced SEEs (Single Event Effect), electrons are also capable of causing these effects via electro-nuclear interactions [4].

Lately, increased interest has been shown for understanding the exact mechanisms behind these electron induced events and on understanding the results of these tests. The task is made more difficult by several factors which play an important role in low-energy electron irradiation campaigns. Due to the low probability of SEE caused by electrons, extra care has to be taken to unfold the various mechanisms which are involved in creating these SEEs. In this paper, the possible contribution from other particles created by the electron interactions with the beamline elements of the linac are analysed, while the possible prompt dose effects and elastic scattering mechanisms are discussed. The importance of eliminating these charge pile-up effects contribution possibility by conducting tests with varying dose rates is shown.

Date of original submission: 29.09.2017, date of revised submission: 10.04.2018, date of acceptance: 18.05.2018

M. Tali, R. G. Alía, M. Kastriotou, M. Brugger, R.Corsini, S. Danzeca , G. Tsiligiannis and W. Farabolini are with CERN, CH-1211 Geneve 23, Switzerland. (e-mail: maris.tali@cern.ch)

M. Tali, V. Ferlet-Cavrois, G. Santin, C. Boatella Polo and A. Zadeh are with the European Space Agency, ESTEC, 2200 AG Noordwijk, The Netherlands.

M. Tali, A. Javainen, H. Kettunen and A. Virtanen are with the Department of Physics, Accelerator Laboratory, University of Jyväskylä, FI-40014, Jyväskylä, Finland

We perform an in-depth analysis of the SEE observed during testing at medical electron linacs. For electron irradiations these type of accelerators are most commonly used due to their availability and flexibility. Whereas previous efforts were made to characterise the SEE mechanisms at higher energies, where the nuclear interaction cross section is larger [5], this paper takes a closer look at the electron energies starting from the threshold region. While [5] analysed in detail the electro- and photonuclear reactions which cause upsets in larger technologies, this paper aims to complement the in-depth analysis with further experimental results, including different technology sizes.

Irradiations at a medical linac at the RADEF facility at Jyvaskyla, Finland were made with two different devices, with large difference in feature size: the ESA SEU (single-event upset) monitor [6] [7] and an Artix-7 Field Programmable Gate Array (FPGA) test board. The tests were done with different energies and different fluxes. In previous work [4] similar irradiations have been presented, however in the present study additional possible explanations for the mechanisms involved are given. To evaluate the sensitivity of the Artix-7 device to potential direct ionization effects, a low-energy proton test was performed. The ESA SEU monitor is considered to be insensitive to direct ionization due to the large, $0.25\,\mu m$ transistor size.

Additionally, tests with an experimental high-energy electron linac were performed at the VESPER facility at CERN, with energies ranging from $60\,MeV$ up to $200\,MeV$. The latter with the aim to give a more complete picture of the mechanisms governing the SEU at all energies relevant to the presented devices. As the Artix-7 displayed a higher cross-section, hypothesis for elastic electron/nucleon interactions as the main mechanism is presented, as suggested earlier by [8]. With all the relevant energies covered, a complete experimental electron-induced SEU Weibull fit could be found. This is relevant in light of the widespread use of commercial off-the-shelf (COTS) devices in demanding radiation environments. The irradiations at VESPER were performed with varying energies and intensities to rule out a potential prompt dose effect.

Additional tests were performed at VESPER with a slab of commonly used spacecraft shielding material, aluminium, placed in front of the detector. The goal was to evaluate the effect of secondary photons on the SEU cross-section of the ESA SEU monitor. In addition, a shielding material analysis was performed using FLUKA [9] [10]. The effect of the vari-

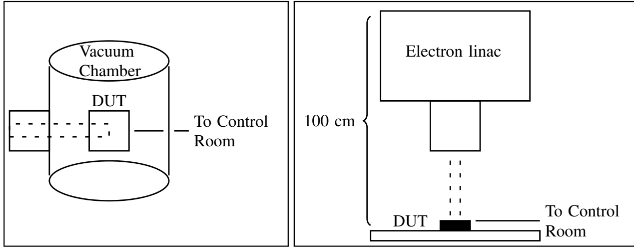

Fig. 1. Not to scale, left) Low-energy proton line test setup at RADEF right) Electron linac test setup, with the distance to the isocenter shown.

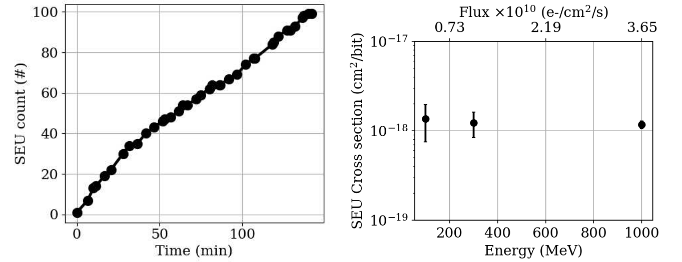

Fig. 2. Electron-induced SEUs in the ESA SEU monitor, left) upsets in time (dose rate $1\,\mathrm{krad(H_2O)/\,min}$, $20\,\mathrm{MeV}$) right) the cross section dependence on dose rate.

ous thicknesses of the materials on dose and flux of electrons, neutrons and photons was evaluated. The implications of the secondary particle creation on the ESA SEU monitor upset cross-section is evaluated and compared to the experimental measurements performed in VESPER.

Another motivation for a greater understanding in these electron-induced SEE are the planned missions to Jupiter. In the Jovian environment the greatest contribution to the overall dose level are the high-energy electrons in the trapped radiation belts [11]. The experimental electron-induced SEU Weibull fit was used to estimate the number of upsets in the ESA SEU monitor caused directly by the trapped electron spectra cited in [11].

II. Facilities and Test Setups

A. RADEF Facility

The RADEF (RADiation Effects Facility) consists of two caves. One contains the low- and high-energy proton and heavy ion lines and the other the electron linac [12]. The low-energy proton line can provide energies from about $500\,\mathrm{keV}$ to $6\,\mathrm{MeV}$. The maximum flux is dependent on the energy, at $1.5\,\mathrm{MeV}$ this corresponds to about $5 \times 10^7\,\mathrm{p/cm^2/s}$. The components under test are attached to a movable backplate in a vacuum chamber. The cables needed were connected through the vacuum feed-throughs to a computer at the control room as seen in Fig. 1 [13].

The electron linac at the RADEF facility, Varian 2100CD Clinac, is able to deliver electron beams with energies from $6\,\mathrm{MeV}$ up to $20\,\mathrm{MeV}$ and dose rates up to $1\,\mathrm{krad(H_2O)/min}$, which is a dose in water at the maximum calibration used in medical treatments. At the maximum dose rate the beam consists of $5\,\mu\mathrm{s}$ pulses with a period of $5\,\mathrm{ms}$. The typical beam size is $20\,\mathrm{cm} \times 20\,\mathrm{cm}$. For the irradiations a beam size of about $2\,\mathrm{cm} \times 2\,\mathrm{cm}$ was used. For the irradiations, the components are placed on a table located in the cave and connected to a computer in the control room through a $20\,\mathrm{m}$ Ethernet cable [14].

B. RADEF Test Setup

The irradiations were performed on two devices, the ESA SEU monitor and the $28\,\mathrm{nm}$ Artix-7 FPGA test board Arty, both at nominal voltage. The ESA SEU monitor consists of 4 SRAMs, the technology node size is $250\,\mathrm{nm}$ [7].

The ESA SEU monitor was placed on the table at the isocenter, at $100\,\mathrm{cm}$ from the exit window of the linac, as shown on the right in Fig. 1. The irradiations were performed with a fixed dose rate and the number of upsets was noted at the end of each run. In order to investigate the possibility of prompt dose effects, as discussed in [4], the irradiations were performed with varying pulse charge to change the electron flux. The pulse charge was changed by reducing the current given by the electron source, the time structure of the pulses did not change. The cross section did not show any pulse charge dependence, as can be seen on the right in Fig. 2. As a result, the possibility that the upsets are caused by charge build-up can be ruled out.

The Artix-7 test board was placed on the test table, at $100\,\mathrm{cm}$ from the linac exit window. The FPGA package was opened before the test. The FPGA was programmed with a checkerboard pattern prior to irradiation and had a total of $1.44\,\mathrm{Mbit}$ of block RAM (BRAM). The BRAM was read periodically during testing through the UART interface of the FPGA, and the number of upsets was noted, no write or read operations were performed between the readouts on the BRAM.

C. VESPER Facility

The VESPER facility, a part of the CLIC Test Facility CTF3 at CERN, is an electron linac, which provides a multi-purpose electron beam for accelerator technology tests. Since the recent upgrades to the beam-line and the possibility of running the facility using only one or two klystrons, the energy range of the facility is now improved and can reach from $60\,\mathrm{MeV}$ to $200\,\mathrm{MeV}$ [5].

D. VESPER Test Setup

The ESA SEU monitor was placed in the beam to evaluate the electron-induced SEU cross section and confirm its energy dependence as described in [5]. To evaluate the beam spot evolution over time, a radio-sensitive film HD-V2 was used to precisely estimate the fluence of electrons covering each die of the ESA monitor and therefore more precisely evaluate the SEU cross-section. As the beam spot size is usually sufficient to cover all of the 4 dies uniformly, a more precise analysis was only necessary for the lowest energy runs. A run performed at VESPER demonstrating the uniformity of the beam shape and the stability of the beam charge over time can be seen in Fig. 3. The beam charge at the facility is monitored using a

beam charge monitor and the total fluence for the cross-section calculations is found using this detector.

The Artix-7 test board was placed on the test position, at the same position as the ESA SEU monitor. The FPGA package was opened before the test. The beam size was chosen so that it uniformly covered the FPGA die. The remaining test procedure was identical to the test procedure at RADEF.

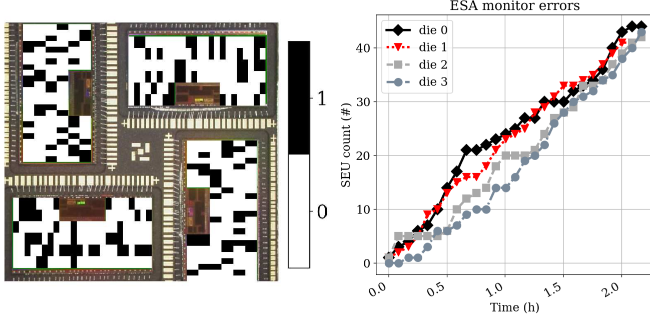

Fig. 3. left) Distribution of upsets in the ESA SEU monitor during a single run right) Evolution of upsets over time for the 4 die of the ESA SEU monitor.

III. Experimental results

A. *RADEF ESA SEU monitor electron irradiation results*

The ESA SEU monitor is programmed with a checkerboard pattern prior to irradiation and is then read out periodically, no read or write operations are performed between readouts. When an upset is found during the readout, the erronous bit is rewritten and added the seu count. The ESA SEU monitor was tested with 20 MeV, 16 MeV and 12 MeV electrons with varying electron fluxes. Due to the exceedingly low cross section, seeing an actual upset would require a high dose to the component, therefore at 12 MeV just an upper bound measurement was estimated. The test results are summarized in Table I. The cross section was calculated with the common definition:

$$\sigma = \frac{\#\ \text{SEUs}}{\phi \times \#\ \text{bits}} \quad (1)$$

where # SEUs is the number of SEU observed during the irradiation, # bits is the size of the memory array in bits and ϕ is the electron fluence in $\mathrm{e/cm^2}$. The ionization chambers in the linac give a dose measurement in terms of rad deposited in the maximum dose deposition depth in water. To estimate the number of electrons corresponding to a dose of 1 Gy, a FLUKA [9] [10] simulation was performed. In the simulation the energy deposited by a 20 MeV electron beam in a $1\,\mathrm{cm} \times 1\,\mathrm{cm} \times 0.1\,\mathrm{cm}$ block of air was scored, which gives us the LET in air. Although the dose of the accelerator was calibrated to water in the maximum dose depth, the LET in air is a close estimation of this value. The resulting calculated fluence to dose conversion factor is $3.65 \times 10^9\ \mathrm{e/cm^2/Gy}$.

B. *VESPER ESA SEU electron irradiation results*

To evaluate the cross-section over the complete energy range for the ESA SEU monitor, tests at 60, 115 and 175 MeV were performed. The experimental cross-section from VESPER fits well with cross-sections measured both with the medical linac from RADEF and earlier measurements performed at VESPER in 2016 [5], with results ranging from 16 MeV up to 200 MeV. A summary figure can be seen in Fig. 4.

TABLE I

ESA SEU monitor electron irradiation results at the RADEF and VESPER linac, *an upper bound has been given for the 12 MeV irradiation. For the VESPER linac runs which have been gruped together for the Weibull fit are shown with brackets.

RADEF linac				
Energy (MeV)	**Dose rate (rad/min)**	**Total Dose (krad)**	**SEUs**	**Cross section (cm^2/bit)**
20.0	1.00×10^3	160	115	1.17×10^{-18}
20.0	3.00×10^2	13.3	10	1.14×10^{-18}
20.0	1.00×10^2	6	5	1.36×10^{-18}
16.0	1.00×10^3	60	2	5.44×10^{-20}
12.0	1.00×10^3	10	0	*1.63×10^{-19}
VESPER linac				
Energy (MeV)	**Duration(h)**	**Fluence (e-/cm^2)**	**SEUs**	**Cross section (cm^2/bit)**
VESPER 2017				
62	19.0	1.39×10^{13}	277	2.45×10^{-18}
60	58.0	1.79×10^{14}	2974	2.08×10^{-18}
115	17.0	1.39×10^{13}	374	3.33×10^{-18}
175	7.9	1.16×10^{13}	579	6.17×10^{-18}
175	11.8	1.72×10^{13}	653	4.67×10^{-18}
VESPER 2016				
133	15.1	3.95×10^{12}	81	1.87×10^{-18}
133	14.8	4.20×10^{12}	141	3.42×10^{-18}
170	8.1	3.01×10^{12}	143	4.29×10^{-18}
170	13.9	5.09×10^{12}	169	2.88×10^{-18}
206	16.0	2.60×10^{13}	1558	5.97×10^{-18}
206	7.5	5.30×10^{12}	283	5.09×10^{-18}
206	16.0	1.04×10^{13}	545	4.68×10^{-18}

C. *Experimental Weibull fit for electron-induced SEU in the ESA SEU monitor*

Since electron measurements have now been performed over a wide energy range, a total electron-induced SEU cross-section Weibull fit could be found, as seen in Fig. 4. The parameters for the Weibull fit were as follows: XSsat = $3.84 \times 10^{-18}\ \mathrm{cm^2/bit}$, Lo = 16.0 MeV, W = 45.3 MeV and s = 0.62. The main difference between the simulated electron-induced SEU cross-section and the one reported in [5] is the width parameter W. The main reason for the difference is the fact that the Weibull fits were found separately for electrons and photons. As discussed in this paper, since the photons play an important role in the total SEU cross-section, the real response of devices to electron irradiation will be a combined contribution from electrons and photons. Therefore, to more accurately evaluate the electron-induced upset cross-section, an analysis of possible contributions of secondary particles should be performed.

To further estimate the secondary particle contribution, FLUKA simulations with various common spacecraft shielding materials placed in front of the ESA SEU monitor are

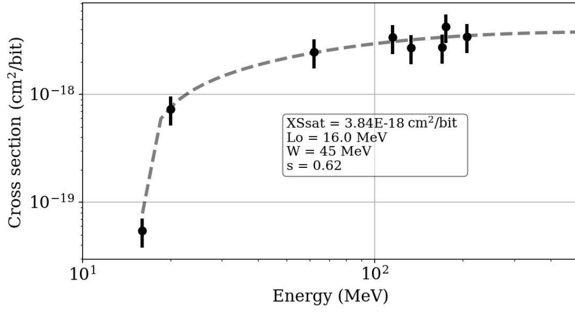

Fig. 4. The Weibull fit for electron induced SEU for the ESA SEU monitor based on measurements from the VESPER and the RADEF facility.

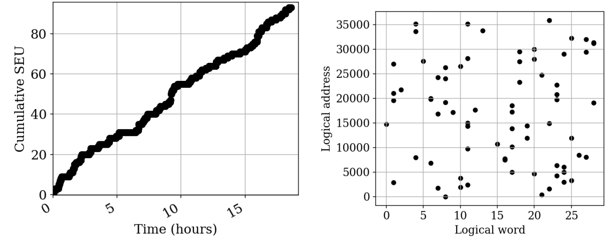

Fig. 5. left) Cumulative SEU of Artix-7 $60\,\mathrm{MeV}$ run at VESPER right) Logical map of SEU of Artix-7 $60\,\mathrm{MeV}$ run at VESPER.

described in section IV-D. To verify the FLUKA simulations, a measurement was performed in the VESPER facility with a slab of $1\,\mathrm{cm}$ of aluminium placed directly in front of the device. The resulting cross-section at $175\,\mathrm{MeV}$ was $3.26 \times 10^{-17}\ \mathrm{cm^2/bit}$, compared to $5.26 \times 10^{-18}\ \mathrm{cm^2/bit}$ without the aluminium slab, or about 6 times higher. This measurement result confirms the theory that secondary photons contribute to the upsets seen in electron beam irradiation. To rule out that the higher overall flux caused by the secondary particles created by the aluminium slab was causing a prompt dose effect, measurements with two different intensities were performed. For a beam charge of $9\,\mathrm{pC}$ a cross-section of $3.216 \times 10^{-17}\ \mathrm{cm^2/bit}$ was seen. At $2\,\mathrm{pC}$ the cross-section was 3.068×10^{-17}, the difference being 5% and therefore statistically comparable. As shown by [1], if the upsets were indeed caused by prompt dose effects, the cross-section would vary linearly with the intensity. Since the cross-section does not vary with the varying intensity, we can conclude that the upsets were caused by electro- and photo-nuclear interactions, as described in [5].

D. VESPER and RADEF Artix-7 electron irradiation results

Two irradiation runs were made with varying dose rate. Only 2 upsets in the memory array were observed during the irradiations. For a total deposited dose of $100\,\mathrm{krad}$, this corresponds to a cross section of $3.81 \times 10^{-19}\,\mathrm{cm^2/bit}$ at $20\,\mathrm{MeV}$.

The Artix-7 was irradiated at the 2 extreme energies at VESPER, $60\,\mathrm{MeV}$ and $201\,\mathrm{MeV}$. The resulting cross-sections are $2.01 \times 10^{-17}\,\mathrm{cm^2/bit}$ and $4.76 \times 10^{-17}\,\mathrm{cm^2/bit}$ respectively. An example of one of the $60\,\mathrm{MeV}$ runs can be seen in Fig. 5, which shows the linearity of the runs. An example of the distribution of the logical addresses can be seen in Fig. 5. Although the physical mapping of the BRAM is not available, a map of the logical addresses of the memory provides a first proof that these upsets are random, and not clustered or periodically occurring. A summary of both runs can be seen in Table II.

E. Experimental Weibull fit for electron-induced SEU in the Artix-7 BRAM

The experimental Weibull fit for the electron-induced SEU for the Artix-7 can be seen in Fig. 6. The parameters of the fit are as follows : XSsat = $5 \times 10^{-17}\ \mathrm{cm^2/bit}$, Lo = $19.9\,\mathrm{MeV}$, W = $100\,\mathrm{MeV}$ and s = 0.6. The first, and most important difference with the ESA monitor response is the absolute value of the saturation cross-section, the Artix-7 being 1 order of magnitude higher. According to the hypothesis that the photo- and electro-nuclear interactions cause these single event upsets, which holds for a device with a high critical charge like the ESA SEU monitor, as described in [5], the cross-section would have to be lower for smaller sensitive volume sizes. As the cross-section is clearly higher, an additional effect has to be contributing to the error generation. There have been several hypothesis into competing effects, such as elastic electron/nucleon interactions described in [8]. To get a first estimation of the cross-section of a more modern technology, such as the Artix-7, for photo- and electro-nuclear reaction induced SEU, an amalgamation of a physical RPP simulation and a complete nuclear physical simulation was used to estimate the critical charge for the device. First, energy deposition simulations for electrons and protons were made for the $0.3\,\mathrm{\mu m} \times 0.3\,\mathrm{\mu m}$ side sensitive volume geometry. Then, the experimental saturated SEU cross-section for protons for the same device, found in [15] to be $9 \times 10^{-15}\,\mathrm{cm^2/bit}$ was used. To estimate the critical charge for the Artix-7, the deposited energy at this saturation cross-section is used, and is found to be $3.7\,\mathrm{fC}$. Then, the electron simulation, seen on the left in Fig. 9, is used to estimate the photo- and electro-nuclear interaction cross-section at $3.7\,\mathrm{fC}$ of deposited charge and is shown to be $4 \times 10^{-18}\,\mathrm{cm^2/bit}$ at $200\,\mathrm{MeV}$ and $7 \times 10^{-20}\,\mathrm{cm^2/bit}$ at $20\,\mathrm{MeV}$.

Previous tests of the Artix-7 device for $20\,\mathrm{MeV}$ give the cross section to be in the order of a couple $10^{-18}\ \mathrm{cm^2/bit}$ [4]. The hypothesis given was electro- and photo-nuclear effects. The difference between the value obtained in this work and [4] can be explained by the large uncertainties in cross-section in the threshold region, and therefore are still compatible. However, at higher energies, the cross-section is clearly too large to be explained purely by the electro- and photo-nuclear events. It is feasible that a combination of the two effects, electro- and photo-nuclear and elastic electron/nucleon interactions, can explain the higher cross-section values at higher energies. Further studies are needed in order to more precisely simulate the effects and to understand for which technology nodes and critical charge values the effects are dominating.

As introduced in [16], the maximum energy an elastic electron silicon recoil can transfer displays a very strong

energy dependence on the initial electron energy. A 10 MeV electron deposits maximally about 10 keV whereas a 20 MeV electron deposits about 30 keV. Since the SEU cross-section displays a very strong energy dependence, it is conceivable that the critical energy lies somewhere between the 10 keV and 30 keV, which would explain this dependence.

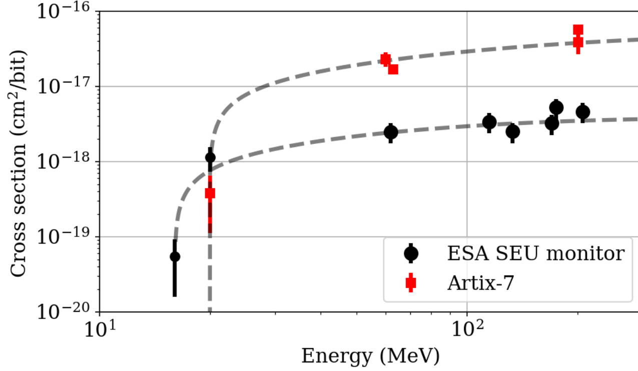

Fig. 6. The Weibull fit for electron induced SEU for the Artix-7 based on measurements from the VESPER and the RADEF facility.

TABLE II
ARTIX-7 IRRADIATION RESULTS AT THE LOW ENERGY PROTON AND ELECTRON LINES AT RADEF AND THE VESPER FACILITY. FIELDS MARKED WITH * ARE THE UPPER BOUNDS FOR THE CROSS SECTIONS

RADEF Low Energy Proton				
Energy (MeV)	**Flux ($p/cm^2/s$)**	**Fluence (p/cm^2)**	**SEUs**	**Cross section (cm^2/bit)**
4.7	5×10^7	1.21×10^{10}	36	2.07×10^{-15}
4.7	1×10^7	1.04×10^{10}	31	2.07×10^{-15}
3.0	6×10^7	1.74×10^{10}	12	4.79×10^{-16}
1.5	5×10^7	2.12×10^{10}	0	$*3.27 \times 10^{-17}$
1	5×10^6	6.08×10^9	0	$*1.14 \times 10^{-16}$
0.8	1×10^7	1.09×10^{10}	0	$*6.37 \times 10^{-17}$
RADEF Electron				
Energy (MeV)	**Dose rate (rad/min)**	**Total Dose (krad)**	**SEUs**	**Cross section (cm^2/bit)**
20.0	1.00×10^2	100	2	3.81×10^{-19}
VESPER				
Energy (MeV)	**Duration(h)**	**Fluence (e-/cm^2)**	**SEUs**	**Cross section (cm^2/bit)**
60	3.1	6.30×10^{11}	21	2.37×10^{-17}
63	18.6	3.80×10^{12}	93	1.70×10^{-17}
201	1.8	1.98×10^{11}	11	3.86×10^{-17}
201	4.3	4.66×10^{11}	38	4.76×10^{-17}

F. RADEF Artix-7 low-energy proton irradiation results

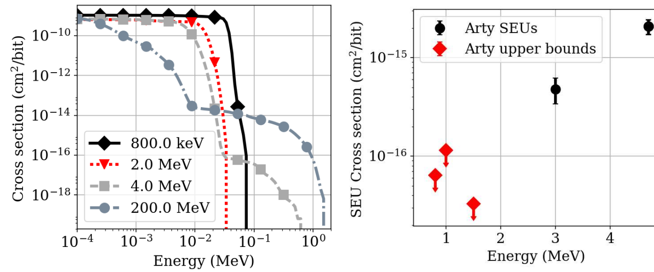

Fig. 7. left) FLUKA simulation for the 300 nm × 300 nm sensitive volume geometry and right) results of the low-energy proton irradiation of the Artix-7 board.

To investigate the possibility of direct ionization contributing to the SEUs, irradiations were done at a low-energy proton line at RADEF. The physical process through which electrons and protons cause upsets in this energy region are the same, with the maximum LET value for electrons being lower. Therefore, an irradiation with protons was selected. The tests were performed in vacuum, and the test procedure was identical to the electron linac tests performed with the same component.

The Artix-7 test board recorded no upsets below 3 MeV. For the lower energies, the upper-bound cross section has been estimated. The results are summarized in Table II and illustrated on the right of Fig. 7. It was observed that this device is not sensitive to direct ionization from protons, therefore, it can be concluded that the same holds true for electrons. FLUKA energy deposition simulations, which are described in more detail in section IV-B, were run and their results can be seen in Fig. 7. The cross-section as a function of critical energy is constant in the direct ionization region and then sharply falls off. The following peak in energy deposition comes from nuclear or indirect ionization events. As can be seen, for energies below about 3 MeV, almost no energy is deposited through indirect ionization, which supports the experimental results.

IV. ANALYSIS OF THE ELECTRON INDUCED SEU MECHANISMS

A. Analysis of the Electron Beam at the RADEF Linac

The dose rate of the RADEF linac is monitored by an ionization chamber. The linac has been characterized extensively, and precise dose depth measurements have been performed using PTW 30013 and PTW 34001 ionization chamber and a water phantom.

For the purpose of understanding precisely the upsets caused by the beam, the composition and spectrum of the beam particles was analysed in a FLUKA simulation. A first iteration of the linac geometry, which includes the main components interacting with the beam has been created. These are the 4 mm beryllium beam exit window, the 2.5 mm aluminium diffusion foil spreading the pencil beam from the accelerator and the two sets of 2.5 cm lead collimators to control the beam size.

For the 20 MeV beam, the exact electron beam kinetic energy is 22.3 MeV [17]. As a first approximation, the accuracy of the FLUKA simulation was assessed by comparing it with the dose depth curves obtained with the beam calibration measurements. The results are deemed suitable for this first analysis, and show a maximum discrepancy of about 15% up to a dose depth of 9 cm, as can be seen on the left of Fig. 8. The beam spectra were also simulated in order to estimate the contribution to the cross section of the relevant

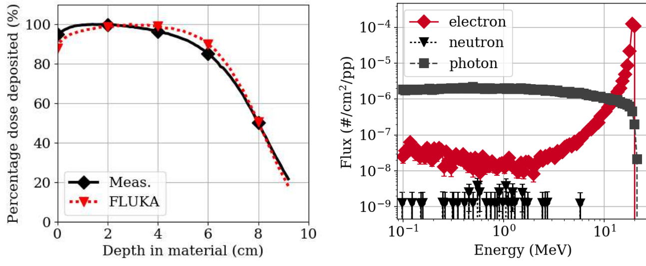

Fig. 8. left) Comparison of the FLUKA simulation and experimental measurements at the electron linac of 20 MeV electrons in water right) Flux of electrons, neutrons and photons scored at the surface of the water target in the clinac FLUKA simulation, logarithmic binning is used.

particles: electrons, photons and neutrons. Due to the electron beam interacting with various elements of the linac, there is a sizable flux of mostly bremsstrahlung photons generated by the electron-matter interactions.

B. FLUKA Energy Deposition Simulation

To estimate the energy deposited by 20 MeV electrons in the ESA SEU monitor, with a feature size of 0.25 µm and the Artix-7, with a feature size of 28 nm, two geometries were created. Both geometries consist of a stack of aluminium and silicon dioxide layers, with the bottom layer representing the active silicon, also containing cubes of sensitive volumes for energy deposition scoring. The geometry representative of the ESA SEU monitor had a sensitive volume side of 3 µm × 3 µm, which has been shown earlier to match well with experimental data [5]. Since no heavy-ion irradiation was performed for the Artix-7, an estimation for a more modern technology size SV was used. A side of 300 nm × 300 nm is a good estimation for a smaller features size, as described for a 45 nm technology in [4] where the procedure described in [18] was implemented. For both a sensitive volume depth of 0.5 µm was used.

The simulation results for electrons can be seen in Fig. 9.

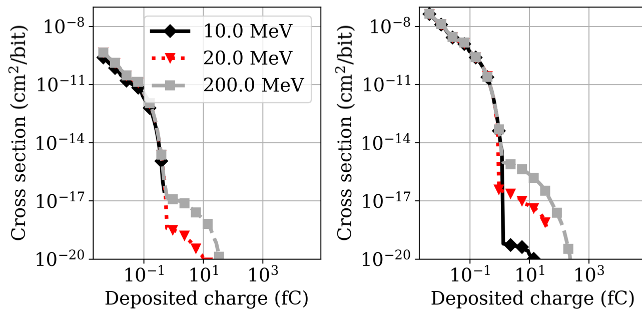

Fig. 9. FLUKA energy deposition simulations for the left) 0.3 µm × 0.3 µm and right) 3 µm × 3 µm sensitive volume geometries.

C. Contribution of Photons to the Cross Section

As observed from the first estimation of the fluxes of the particles created by the electron beam interaction with the linac elements in Fig. 8, in addition to electrons, photons with energies up to the beam energy are created. These photons have a higher probability of causing an upset at the same energy than an electron due to the higher nuclear interaction cross section. Because of this, the photon contribution to the SEU cross section is comparable to that of the 20 MeV electrons. To estimate the contribution of photons to the cross section, the simulated particle fluxes are folded with the Weibull responses for each particle, which were estimated in [5]. The folding of the simulated fluxes and the Weibull function is described as:

$$N_i/pp = \int \frac{d\phi_i(E)/pp}{dE} \cdot \sigma_i(E)\, dE \tag{2}$$

where N_i is the expected number of upsets per primary particle from FLUKA, $\frac{d\phi_i(E)/pp}{dE}$ is the flux per primary particle in $\#/\mathrm{MeV/pp}$ and $\sigma_i(E)$ is the Weibull estimated cross section for the given particle.

Finally, to obtain the estimated cross section σ_{calc}, the result N_i/pp has to be normalized to the total integrated flux of electrons per primary particle ϕ/pp, which primarily contribute to the dose. The flux per primary particle can be seen in Fig. 4, and is obtained from the FLUKA simulation of the electron linac. Therefore:

$$\sigma_{calc} = \frac{N_i/pp}{\int \phi(E)/pp\, dE} \tag{3}$$

For the ESA SEU monitor, the folding at 20 MeV, the contribution from electrons, $1.69 \times 10^{-19}\,\mathrm{cm^2/bit}$, and photons, $2.47 \times 10^{-19}\,\mathrm{cm^2/bit}$, is comparable. At 16 MeV, the Weibull fit threshold was estimated as 15.9 MeV [5], therefore only the photons contribute to the cross section, which is $6.56 \times 10^{-21}\,\mathrm{cm^2/bit}$. The neutron contribution at both energies was negligible.

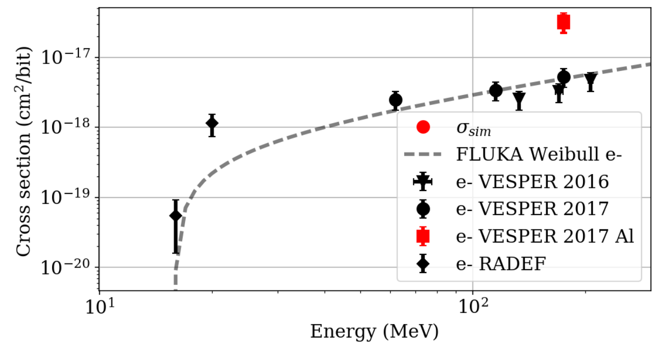

Fig. 10. The FLUKA based Weibull fit for electron induced SEU for the ESA SEU monitor [5] and the measurements from the VESPER and the RADEF facility, including a measurement with an aluminium slab, sum of σ_{sim} from (3) for each energy, from folding the Weibull fit and the simulated spectra, seen in Fig. 8.

D. Shielding Material Analysis

Due to the observation that photons have a large impact on the cross-section, a further study of this effect has been conducted. In space missions, it is imperative to protect the sensitive electronics inside the spacecraft from the harmful

effects of radiation. Often the shielding consists of several layers of material, and the general strategy is to place a thin layer of dense material, for example tantalum or lead in the outer layer and then a thicker layer of lower-density material, like aluminium on the inner layers. The combined effect is then that the high density material generates secondary particles and the thicker layer of material dampens the generated spectra of various particles. Although this strategy works well for dose, the amount of secondary photons generated presents a challenge. The effect of various thicknesses of shielding materials is then analysed. Whereas the impact of secondaries created in shielding in electron-dominated environments were studied in [19] and [20] in the context of displacement damage, this work focuses on single-event upsets.

Firstly, the materials chosen are commonly used in spacecraft shielding: aluminium, lead, tantalum and a final material chosen was copper for direct comparison with earlier experimental data from [5]. The material thicknesses were chosen from 1 to 40 mm, which are the typical thicknesses of shielding used. A 200 MeV electron beam impinged on the various thicknesses of the shielding material and the resulting secondary particle spectra and deposited dose in air were scored. The resulting particle spectra for aluminium and tantalum can be seen in Fig. 11. The denser material tantalum generates a much larger amount of secondaries, especially neutrons.

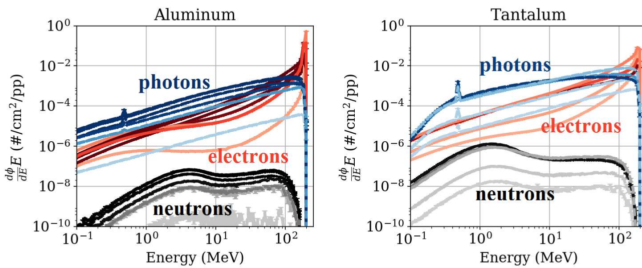

Fig. 11. Spectra of secondary particles generated by left) aluminium right) tantalum. Lighter color means thinner shielding, darker color means thicker shielding.

To estimate the contributions that the various particles have on the SEU cross-section for the ESA SEU monitor the flux of particles exceeding 10 MeV was found and can be seen in Fig. 12. The most obvious effect that the shielding has on the neutron and photon flux is that of increasing it by several orders of magnitude even after relatively small shielding thicknesses. As expected, the denser materials tantalum and lead produce more secondaries and the particle fluxes are therefore higher than for the less dense aluminium. However, the electron fluxes remain relatively constant regardless of shielding material and thickness. This is a good indication that the additional shielding will increase the SEU contribution for neutrons and photons, whereas the electron cross-section will remain relatively constant. It is worth noting that the neutron cross section is about 5 orders of magnitude lower than the electron cross-section. However, since the SEU cross-section of neutrons is much higher than that of the electrons and photons, the contribution has been further analysed.

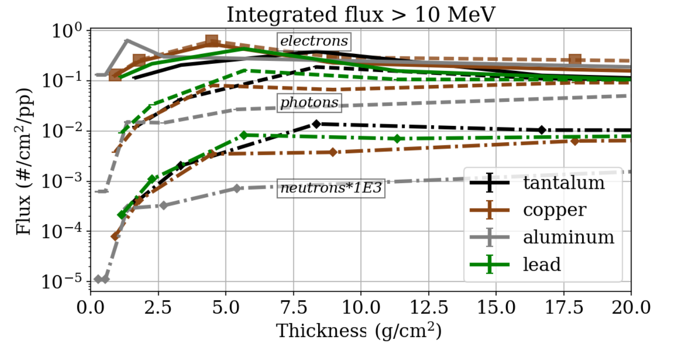

Fig. 12. Integrated flux over 10 MeV, these are the particles which mainly contribute to the SEU cross-section for the ESA SEU monitor.

To analyze the contributions of different particles to the SEU cross section of the ESA SEU monitor, the various particle spectra were folded with the corresponding Weibull response for each particle, described in [5], of the monitor and the results can be seen in Fig. 13. As expected, the contribution of photons to the cross-section is dominant after even thin shielding thicknesses, the increase of the cross section for aluminium is about two orders of magnitude for photons. Since aluminium is a commonly used shielding material, the analysis clearly demonstrates the challenges this radiation environment poses for even a relatively old technology. Even though the SEU cross-section for electrons is relatively constant, the real effect of the high-energy electrons is due to the secondary photons produced by Bremsstrahlung as these electrons travel through the shielding materials.

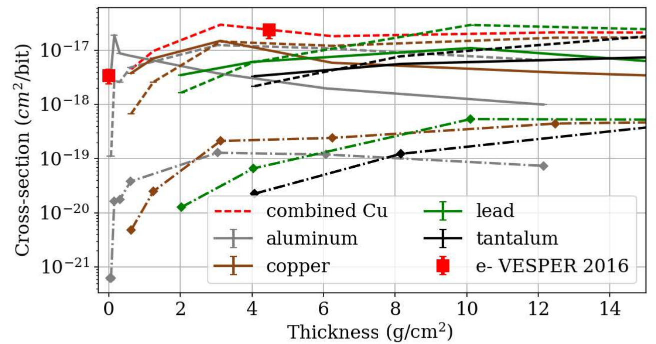

Fig. 13. SEU cross-section contribution for secondary protons, neutrons and photons produced by a 200 MeV electron beam transported through common shielding materials for the ESA SEU monitor. The line shows the electrons, the dashed line are the photons and the dashed and dotted line are the neutrons.

E. Analysis of Elastic Recoils Contribution to the cross section

In order for an elastic recoil to cause an upset, it has to deposit a higher charge than the critical charge limit for a given device. For the ESA SEU monitor the critical charge is considered to be about 10 fC. As discussed in [8], the maximum charge an elastic recoil can deposit at 20 MeV is about 0.5 fC. Therefore, it is impossible that an upset caused by an elastic interaction recoil takes place in our device

leading to the conclusion that for irradiations at medical linacs operating up to 20 MeV, the mechanism is disregarded as a contributor to the total SEU cross section.

F. Analysis of electron induced-upsets in a Jovian environment

In the Jovian environment the greatest contribution to the overall dose level are the high-energy electrons in the trapped radiation belts, as described in [11]. As described in [5], the secondary electrons and photons created by the trapped electrons traveling through the spacecraft shielding contribute most to the overall SEU cross-section when considering the ESA SEU monitor example. Since the experimental electron-induced SEU cross-section Weibull fit was found in this paper, we can directly fold the fit with the integrated trapped electron spectra from [11] to get an estimate of the ESA SEU monitor cross-section. The estimated cross-section was found to be 11.7 SEU/device/mission, which is in the same order of magnitude as the cross-section for the secondary particles found in [5]. Therefore, although the higher flux generated by the electrons traveling through shielding increases the overall upset rate, a considerable amount of upsets are caused directly by the trapped electrons themselves.

V. Summary and Conclusions

Experiments were performed with electrons at the VESPER Facility at CERN, with energies ranging from 60 MeV up to 200 MeV and at the RADEF facility from 12 MeV up to 20 MeV to cover the gap between the results in this paper and in [5]. This provides a more complete picture of the mechanisms governing the electron-induced SEU at all energies. For the first time complete experimental electron-induced SEU cross-section Weibull fits have been found. Irradiations were performed using two different devices, the ESA SEU monitor and an Artix-7 FPGA test board. Both the energies and also the fluxes were varied during the irradiations. The tests showed no indication of pulse charge dependence, therefore pile-up effects can be ruled out as a contribution to the cross section.

The contribution of photons to the cross-section was tested by placing a slab of aluminium in front of the detector, confirming that photons have a strong contribution to the overall electron-induced SEU cross-section. The SEU cross section showed a strong dependency on the beam energy. This result was confirmed by the FLUKA energy deposition simulations. The Artix-7 response indicates that an additional effect has to be considered for smaller transistor sizes, such as elastic electron/nucleon interactions described in [8] and that further analysis is needed to understand these effects.

The possible contribution from other particles created by the electron interactions with the beamline elements of the medical linac were analysed. Through simulations, the contribution from Bremsstrahlung photons to the overall cross section was found to be roughly equal to that of the 20 MeV electrons. In addition, a low energy proton irradiation was performed on the Artix-7 FPGA, showing that the device was not sensitive to prompt dose effects caused by protons and therefore also low energy electrons.

A study into the various shielding materials used in space missions and their contribution to the cross-section was performed using FLUKA. The implications of the secondary photons, neutrons and electrons created when the high-energy electrons pass through the shielding material is discussed. A good fit between the experimental and the simulated cross-sections is shown. This paper demonstrates that even a small amount of shielding material has a significant impact on the overall SEU cross-sections and should therefore be accounted for when evaluating the performance of components for use in harsh radiation environments.

Similarly to how one would evaluate the SEU performance of a component for protons, this paper demonstrates that the same method can be applied to electrons. A practical application of folding the Jovian trapped electron spectra with the experimental electron-induced SEU Weibull fit. Even though the overall cross-section of electron-induced SEU is several orders of magnitude lower than that of protons, the large fluxes of trapped electrons in the Jovian atmosphere create the same order of magnitude of upsets as the secondary particles.

References

[1] M. P. King, R. A. Reed, R. A. Weller, M. H. Mendenhall, R. D. Schrimpf, B. D. Sierawski, A. L. Sternberg, B. Narasimham, J. K. Wang, and E. Pitta, "Electron-induced single-event upsets in static random access memory," *IEEE Trans. Nucl. Sci.*, vol. 60, no. 6, pp. 4122–4129, Dec. 2013.

[2] B. D. Sierawski, J. A. Pellish, R. A. Reed, R. D. Schrimpf, K. M. Warren, R. A. Weller, M. H. Mendenhall, J. D. Black, A. D. Tipton, and M. A. Xapsos, "Impact of low-energy proton induced upsets on test methods and rate predictions," *IEEE Trans. Nucl. Sci.*, vol. 56, no. 6, pp. 3085–3092, Dec. 2009.

[3] B. D. Sierawski, M. H. Mendenhall, R. A. Reed, M. A. Clemens, R. A. Weller, R. D. Schrimpf, E. W. Blackmore, M. Trinczek, B. Hitti, and J. A. Pellish, "Muon-induced single event upsets in deep-submicron technology," *IEEE Trans. Nucl. Sci.*, vol. 57, no. 6, pp. 3273–3278, Dec. 2010.

[4] M. J. Gadlage, A. H. Roach, A. R. Duncan, M. W. Savage, and M. J. Kay, "Electron-induced single-event upsets in 45-nm and 28-nm bulk CMOS SRAM-based FPGAs operating at nominal voltage," *IEEE Trans. Nucl. Sci.*, vol. 62, no. 6, pp. 2717–2724, Dec. 2015.

[5] M. Tali, R. Alia, M. Brugger, R. Corsini, W. Farabolini, V. Ferlet-Cavrois, A. Mohammadzadeh, G. Santin, and A. Virtanen, "High-energy Electron Induced SEUs and Jovian Environment Impact," *IEEE Trans. Nucl. Sci.*, vol. 64, no. 8, pp. 2016 – 2022, Aug. 2017. [Online]. Available: http://ieeexplore.ieee.org/document/7944600/

[6] R. Harboe-Sørensen, C. Poivey, F.-X. Guerre, A. Roseng, F. Lochon, G. Berger, W. Hajdas, A. Virtanen, H. Kettunen, and S. Duzellier, "From the reference SEU monitor to the technology demonstration module on-board Proba-II," *IEEE Trans. Nucl. Sci.*, vol. 55, no. 6, pp. 3082–3087, Dec. 2008.

[7] R. Harboe-Sørensen, C. Poivey, N. Fleurinck, K. Puimege, A. Zadeh, F.-X. Guerre, F. Lochon, M. Kaddour, L. Li, and D. Walter, "The technology demonstration module on-board PROBA-II," *IEEE Trans. Nucl. Sci.*, vol. 58, no. 3, pp. 1001–1007, Jun. 2011.

[8] C. Inguimbert, R. Ecoffet, and D. Falguère, "Electron induced SEUs: microdosimetry in nanometric volumes," *IEEE Trans. Nucl. Sci.*, vol. 62, no. 6, pp. 2846–2852, Dec. 2015.

[9] A. Ferrari, P. R. Sala, A. Fasso, J. Ranft, A. Ferrari, P. R. Sala, A. Fassò, and J. Ranft, "FLUKA: A multi-particle transport code," in *CERN 2005-10 (2005), INFN/TC 05/11, SLAC-R-773*, Jan. 2005.

[10] T. T. Böhlen, F. Cerutti, M. P. W. Chin, A. Fasso, A. Ferrari, P. G. Ortega, A. Mairani, P. R. Sala, G. Smirnov, and V. Vlachoudis, "The FLUKA code: developments and challenges for high energy and medical applications," *Nucl. Data Sheets*, vol. 120, pp. 211–214, Jun. 2014.

[11] JUICE Team, "JUICE environment specification," ESTEC/ESA, Noordwijk, Netherlands, Tech. Rep., 2015.

[12] A. Virtanen, "Radiation effects facility RADEF," in *Proceedings of the Eighth IEEE International On-Line Testing Workshop (IOLTW 2002)*. IEEE, 2002, p. 188.

[13] H. Kettunen, V. Ferlet-Cavrois, P. Roche, M. Rossi, A. Bosser, G. Gasiot, F.-X. Guerre, J. Jaatinen, A. Javanainen, and F. Lochon, "Low energy protons at RADEF-application to advanced eSRAMs," in *Radiation Effects Data Workshop (REDW), DOI: 10.1109/REDW.2014.7004577*. IEEE, 2014, pp. 147–150.

[14] "RADiation Effects Facility RADEF - Linear electron accelerator," 2016. [Online]. Available: https://www.jyu.fi/fysiikka/en/research/accelerator/radef/facility/linac

[15] F. S. G. Tsiligiannis, S. Danzeca, R. Garcia-Alia, A. Infantino, A. Lesea, M. Brugger, A. Masi, S. Gilardoni, "Radiation Effects on Deep Submicron SRAM-based FPGAs for CERN applications," *IEEE Trans. Nucl. Sci. (submitted)*, vol. NA, 2017.

[16] A. Akkerman, J. Barak, and N. M. Yitzhak, "Role of Elastic Scattering of Protons, Muons, and Electrons in Inducing Single-Event Upsets," *IEEE Trans. Nucl. Sci.*, vol. 64, no. 10, pp. 2648–2660, Aug. 2017.

[17] J. C. Liu, K. R. Kase, X. S. Mao, W. R. Nelson, J. H. Kleck, and S. Johnson, "Calculations of Photoneutrons from Varian Clinac Accelerators and Their Transmissions in Materials," in *Slac-Pub-7404*, no. SLAC-PUB-7404, Nov. 1997, pp. 1–5. [Online]. Available: http://www.slac.stanford.edu/cgi-wrap/getdoc/slac-pub-7404.pdf

[18] R. A. Weller, M. H. Mendenhall, R. A. Reed, R. D. Schrimpf, K. M. Warren, B. D. Sierawski, and L. W. Massengill, "Monte Carlo simulation of single event effects," vol. 57, no. 4, pp. 1726–1746, Aug. 2010.

[19] C. Dale, P. Marshall, B. Cummings, L. Shamey, and A. Holland, "Displacement Damage Effects in Mixed Particle Environments for Shielded Spacecraft CCDs," *IEEE Trans. Nucl. Sci.*, vol. 40, no. 6, pp. 1628–1637, Dec. 1993.

[20] L. Alexander, S. Allen, and N. L. Bindoff, "Spacecraft displacement damage dose calculations for shielded CCDs," *High-Resolution Sensors and Hybrid Systems*, vol. 1656, pp. 476–487, Aug. 1992.

Publication III

M. Tali, R. G. Alia, M. Brugger, V. Ferlet-Cavrois, R. Corsini, W. Farabolini, A. Javanainen, G. Santin, C. B. Polo, and A. Virtanen, “Mechanisms of electron-induced single event latchup,” *IEEE Trans. on Nucl. Sci.*, Aug 2018

Mechanisms of Electron-Induced Single Event Latchup

Maris Tali[1], Rubén García Alía[2], Markus Brugger[2], Véronique Ferlet-Cavrois[3] Roberto Corsini[2], Wilfrid Farabolini[2], Arto Javanainen[1], Giovanni Santin[3], Cesar Boatella Polo[3], Ari Virtanen[1]

[1]Department of Physics, University of Jyväskylä, Jyväskylä, Finland
[2]CERN, Geneva, Switzerland
[3]ESA/ESTEC, Noordwijk, The Netherlands

***Abstract*—We discuss possible mechanisms by which electrons can induce Single Event Latchups in electronics. The energy deposition and the nuclear fragments created by electrons in silicon are analyzed in this context. The cross-section enhancement effect in the presence of high-Z materials is discussed. First experimental results of electron-induced latchups are shown in SRAM devices with low LET thresholds. The radiation hardness assurance implications and future work are discussed.**

I. Introduction

Energetic particles in space cause various failures in electronics. One of the more dangerous amongst these is the Single Event Latchup (SEL), because the only way to remove the potentially destructive effect is to power cycle the device. A large body of work exists describing the approaches behind and Radiation Hardness Assurance (RHA) qualification for SEL induced by protons [1]–[3] and neutrons [4]. Likewise, work is available showing electrons are capable of producing soft errors [5]–[7], however no experimental evidence of hard failures is so far available. The discussion around the electron-induced radiation effects in electronics has been motivated by the JUpiter Icy Moon Explorer mission (JUICE). In the Jovian environment electrons can reach energies up to a few hundred MeV and are the main contributor to the overall doses received by electronics [8].

It has been shown in [6] through simulations and experimental results that electrons and photons can produce soft errors through high-LET via nuclear interactions products with silicon. Such fragments are similar to those produced by protons [9] and can reach LET (in Si) values of $13\,\mathrm{MeVcm^2/mg}$ for electrons and $15\,\mathrm{MeVcm^2/mg}$ for photons, however with a much lower probability than that associated to proton and nuclear reactions [6]. Therefore, it is presumed that these recoils are in principle also capable of inducing hard errors in devices with a low enough LET threshold. Such effects include Single Event Latchups (SEL) or even Single Event Burnouts (SEB).

Through first experiments at the high-energy electron linac test facility VESPER at CERN, first SEL events were observed in an SRAM memories. Three different memories were tested with varying LET thresholds. The memories are highly sensitive to SEL effects, with an LET threshold of below $\sim 3\,\mathrm{MeVcm^2/mg}$. Despite the expectation that the LET production distribution of electrons and photons could also generate SEL for a low enough LET threshold, the experiential validation confirms that the associated energy, range and angular distribution of the nuclear fragments are compatible with SEL induction.

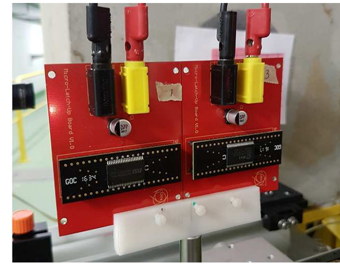

Fig. 1. Experimental setup for the SEL experiment at VESPER, test boards with SRAMs. The SRAM were moved into the beam by a movable stage.

It has been shown previously that high-Z materials present in some ICs greatly increases the probability of causing proton-induced latchup events [2]. This phenomenon introduces additionally a very strong cross-section dependence with energy, therefore requiting the need of testing at the maximum energy present in the working environment. In this work energy deposition simulations were made in FLUKA [10], [11] for electrons, using an integral rectangular parallelpiped (IRPP) geometry for previously described in [12]–[14]. The geometry includes a layer of tungsten to show the effect of the electron-tungsten interaction recoils on the overall energy deposition cross-section. An estimated cross-section was found by folding the previously measured heavy ion cross-section [15] and the FLUKA energy deposition simulations.

In addition, a simulation was performed to characterize the nuclear reaction products created by photons and electrons in tungsten as an extension for work done for protons in [2]. This work shows for the first time that also photons and electrons are also capable of inducing high-LET $\sim 40\,\mathrm{MeVcm^2/mg}$ fission fragments.

II. Facility and Test Setup

The experiments were conducted at the VESPER test bench located at the CLEAR experimental area at CERN [6]. The CLEAR facility is a general purpose electron linear accelerator

TABLE I
A SUMMARY OF THE SRAM MEMORIES TESTED AT VESPER [15]

Shorthand	Version	Size	Tech Node
Alliance	AS7C34098A-10TCN	4 Mbit	200
Brilliance	BS62LV8001BIP55	8 Mbit	180
ISSI	IS61LV5128AL-10TLI	4 Mbit	180

TABLE II
BRILLIANCE SRAM MEMORY IRRADIATION RESULTS AT VESPER, *AN UPPER BOUND HAS BEEN GIVEN FOR THE 60 MeV IRRADIATION, THE 210 MeV DEVICE WAS MOST LIKELY BROKEN

Energy (MeV)	Beam Charge (pC)	Beam size x (mm)	Beam size y (mm)	Total time (min)	Recorded SELs	cross-section (cm^2/Device)
160	11	12	13	25	26	6.14×10^{-11}
215	11	15	12	360	84	1.34×10^{-10}

for electronics and materials testing and accelerator technology development with energies ranging from 60 MeV to 200 MeV. The beam that was used is a dark current beam with a low charge from 3.5 pC to 20 pC per pulse. The beam was diffused using a chromox screen several meters upstream of the test position to cover the SRAM device on the test board.

The devices under test (DUT) were 3 SRAM memories from 3 different manufacturers, ISSI, Brilliance and Alliance, seen in Fig. 1, a summary of the three memories can be seen in Table I. The Brilliance device has been characterized by both a heavy ion beam and proton beams [14], [15], where they were referred to as SRAM F and BS62 respectively. The devices were biased through a programmable Agilent power supply which was also used for de-latching purposes. The SEL detection limit was set to 100 mA and the current was limited to 200 mA during the latchup events. The hold time was 300 ms and the cut time was 2 s. The total standby current consumption of the DUT differed per memory and was 30 mA for the ISSI, 10 µA for the Brilliance (the memory was in the low-power shut down mode during testing) and 12 mA for the Alliance memory.

III. EXPERIMENTAL RESULTS

The experiments were conducted at the VESPER test bench, test board was attached to the movable table. The beam size and intensity were logged by a Fast Beam Current Transformer (FBCT) located just in front of the Device Under Test (DUT) and by a sensitive YAG (yttrium aluminium garnet) fluorescent screen. Both of the detectors are logged and the variation of the beam size and intensity is saved during the test. The devices were biased to 3.3V, which is the nominal working current. The latchup system was controlled and the delatching was performed by the LabView program controlling the Agilent power supply. For all the runs the dark current beam was used at VESPER. The measurement was performed at room temperature.

A. Brilliance Experimental results

The Brilliance SRAM used in this work has a Heavy Ion LET threshold 2.4 MeVcm^2/mg , the date code is 09254, which is equivalent to the SRAM F described in [15]. The Alliance memory is referred to in the same work as SRAM C, with a threshold of 0 MeVcm^2/mg, and the ISSI memory as SRAM A, with a threshold of 2.1 MeVcm^2/mg. Recoils generated by electro- and photonuclear reactions in silicon reach LET values of up to 13 MeVcm^2/mg for electrons and 15 MeVcm^2/mg for photons, as discussed further in section IV-C and shown in [6]. This means that the main contribution to the SEL events observed in this SRAM during irradiation can be attributed to high-LET recoils created in the silicon. Since this SRAM has a high SEL sensitivity, it is a good first experimental proof of electron-induced SEL. In addition to the LET threshold, a more important value in terms of the cross-section is the $L_{1\%}$ value, which is the so-called onset LET value or the value at which the cross-section is 1% of the saturation cross-section [16]. The value is 15 MeVcm^2/mg for the Alliance memory [15], 6.5 MeVcm^2/mg for the ISSI memory [13] and 3.7 MeVcm^2/mg for the Brilliance. These values can also be seen in Table V.

B. ISSI Experimental results

Similar to the Brilliance memory, the ISSI memory has an LET threshold of 2.1 MeVcm^2/mg and therefore the cross-section is dominated by recoils generated by electro- and photonuclear reactions in silicon. The memory has a heavy ion saturation cross-section about an order of magnitude lower than the Brilliance memory which is also seen in the electron-induced SEL cross-section. The cross-section has a visible energy dependence already with the results at 210 MeV having a factor of ~ 2 higher cross-section than the 160 MeV results. Due to the low SEL counts the uncertainties of the results are large and more tests at lower energies would be needed to confirm the energy dependence at lower energies.

Another point to be made is that for the ISSI memory a measurement has been made at 210 MeV with a beam charge of 3.5 pC with a cross-section of $3.20 \pm 0.88 \times 10^{-11}$ and at 215 MeV at 15 pC with a cross-section of $1.76 \pm 0.72 \times 10^{-11}$. The difference between the cross-section is compatible with the experimental uncertainty, whereas the beam charges is changed by 4.3 times. This result excludes the possibility of the pile-up effect which would result in an exponential sensitivity of the SEL rate to the pulse charge [5].

C. Alliance Experimental results

The Alliance memory Weibull fit has a $L_{1\%}$ value of 15 MeVcm^2/mg [13]. This is higher than the LET of the highest silicon recoils created by electrons of 13 MeVcm^2/mg. Therefore as is the case for protons, the SEL cross section for this component is expected to be dominated by tungsten fission fragments, which are produced in a much smaller proportion than silicon fragments owing to the smaller associated volume.

TABLE III
ISSI SRAM MEMORY IRRADIATION RESULTS AT VESPER, *AN UPPER BOUND HAS BEEN GIVEN FOR THE 60 MeV IRRADIATION

Energy (MeV)	Beam Charge (pC)	Beam size x (mm)	Beam size y (mm)	Total time (min)	Recorded SELs	cross-section (cm^2/Device)
60	12	24	15	31	0	2.91×10^{-12}*
155	11	19	20	51	8	1.42×10^{-11}
160	12	13	13	30	5	9.84×10^{-12}
210	3.5	15	24	105	13	3.20×10^{-11}
210	4	15	24	50	6	2.72×10^{-11}
210	4	15	24	27	4	3.35×10^{-11}
215	15	12	13	196	6	1.76×10^{-11}

TABLE IV
ALLIANCE SRAM MEMORY IRRADIATION RESULTS AT VESPER, *AN UPPER BOUND HAS BEEN GIVEN FOR THE IRRADIATIONS AS NO SEL WAS OBSERVED DURING THE TESTS

Energy (MeV)	Beam Charge (pC)	Beam size x (mm)	Beam size y (mm)	Total time (min)	Recorded SELs	cross-section (cm^2/Device)
60	16.6	24	15	296	0	1.83×10^{-12}*
155	10	18	20	50	0	7.98×10^{-13}*
210	11	15	24	110	0	2.35×10^{-12}*

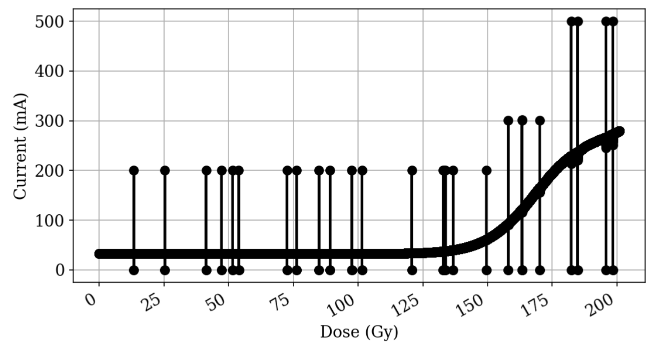

Fig. 2. The increase in current observed in the SRAM standby current during the experiments at VESPER.

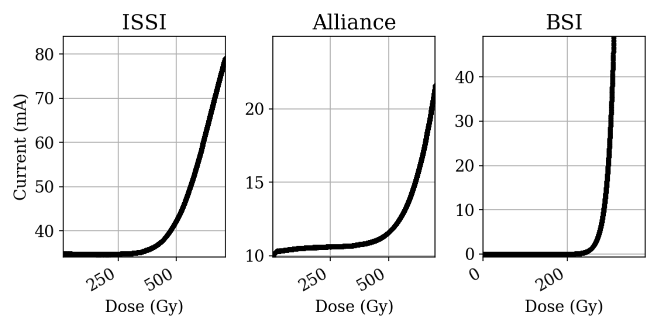

Fig. 3. The increase of the standby current in SRAM biased to nominal voltage. All the 3 devices showed an increase in current similar to the one observed at the VESPER facility.

D. TID Effect Observed During SEL Testing

Due to the low cross-section of electron-induced SEL the DUT receive a large deposited dose during the irradiation. During the experiments an increase of the current consumption was noted, as seen in Fig. 2. During the current increase the DUT continued to experience the SEL events. However, to make sure that the increase in the current did not affect the SEL cross-section results whenever the current increased above the nominal the test results were disregarded.

To better understand if the increase in the current was really caused by the deposited dose a TID test at the Co-60 facility at ESTEC in the Netherlands was conducted. All the 3 devices were exposed to the gamma radiation and the current was monitored during the whole experiment. All the DUT were biased at 3.3 V. For the BSI memory the CE and the $\overline{CE}$ pin were connected additionally so that the memory was turned off.

The increase of current in the 3 devices can be seen in Fig. 3. The overall conclusions for the test were that the current consumption of the ISSI memory starts to increase after about 330 Gy, of the Alliance memory after about 550 Gy and of the BSI memory after about 270 Gy. Therefore, extra care should be taken when testing components for electron induced SEEs due to the large associated fluences to obtain statistically meaningful results and he possible associated TID impact.

IV. ANALYSIS OF THE ELECTRON INDUCED SEL MECHANISMS

A. FLUKA Energy Deposition Simulation

To identify the effect that high-Z materials have on the energy deposited by high-energy electrons, protons, shown previously in [2], and photons in the SV of the SRAM, a FLUKA simulation was performed using a geometry described in [12]–[14] and seen in Fig. 4, where it is shown to be representative of the Brilliance SRAM used in this work. The ISSI and Alliance memory were represented with an SV thickness of 2.5 µm and 3.2 µm respectively in [15], however for a first assessment the 2 µm SV thickness is found as a satisfactory approximation of the most accurate SV thickness.

The geometry used is an IRPP model in grid of 5 x 5 sensitive volumes with a size of 20 µm × 2 µm × 4 µm and a back-end-of-line (BEOL) of 5 µm of SiO2. In addition to this, a layer of 122 nm tungsten placed 200 nm above the sensitive volumes, to assess the effect that high-Z materials have on the energy deposition.

A beam of either electrons, protons or photons impinged on the BEOL, thereafter the energy deposited in each sensitive volume was scored. The resulting reverse integral cross-section can be seen in Fig. 5. The cross-section has been normalized by the simulated beam surface and the actual sensitive volume surface [15].

There are several things to note when comparing the proton and electron cross-sections. (I) The electron and proton cross-sections have a similar shape, with a direct ionisation peak (marked as A in Fig. 5) and a secondary indirect ionisation peak (marked as B in Fig. 5). This peak is composed of secondary recoils that are created by both electron and proton

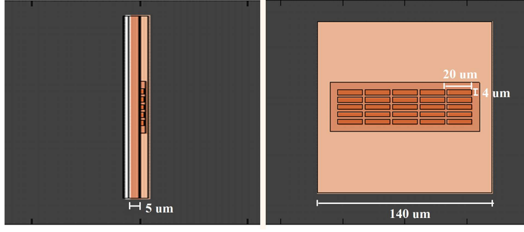

Fig. 4. Geometry of the sensitive volumes and Back-end-of-line

TABLE V
A SUMMARY OF THE WEIBULL PARAMETERS OF THE SRAM MEMORIES TESTED AT VESPER [15] [13].

Shorthand	XSsat (cm^2)	Lo (MeV cm^2/mg)	$L_{1\%}$ (MeV cm^2/mg)	W (MeV cm^2/mg)	s
ISSI	0.24	2.1	6.5	16.8	3.4
Alliance	0.13	0	15	27.6	7.4
Brilliance	0.60	2.4	3.7	13.7	1.8

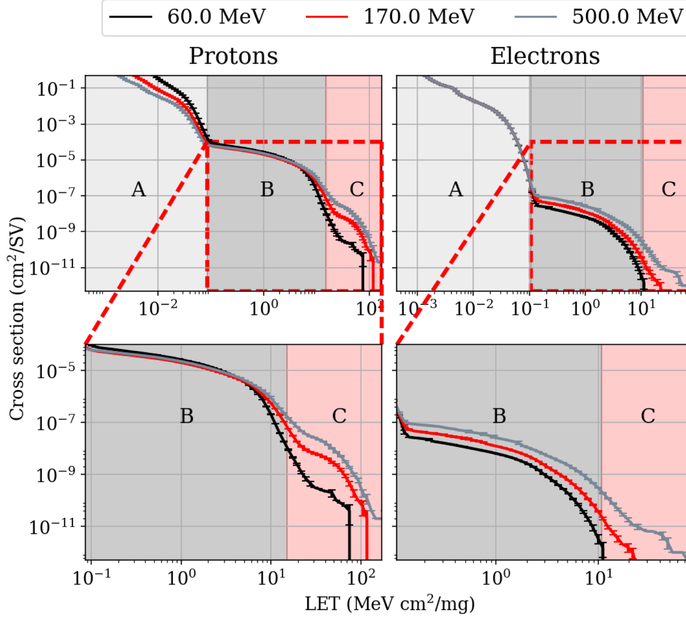

Fig. 5. Reverse integral of the energy deposition simulation in the sensitive volumes. Bottom row is a zoomed version of the top row to highlight the increase in cross-section due to the tungsten recoils. A) Direct ionisation peak B) Indirect ionisation peak, silicon recoils C) The tertiary peak created by recoils from particle-tungsten interaction

interaction with silicon. (II) The proton indirect-ionisation cross-section have no significant energy dependence, whereas electron indirect-ionisation cross-section shows a strong energy dependence. Both point (I) and (II) have been studied in [6]. (III) The introduction of tungsten in the BEOL of the device in the simulation introduces the third peak (marked as C in Fig. 5) in the cross-section. This peak is caused by fission fragments created by tungsten interaction with the particles, as shown in [2] for protons. The peak is not as apparent for electrons due to the lower probability and lower LET of these recoils, as shown in Fig. 10. As opposed to region (B), the energy deposition in the region (C) range exhibits a strong dependence with the incidence particle energy.

B. FLUKA Estimation of the cross-sections

To be able to estimate the cross-section of the electron-induced SEL effects an approach described in [15] has been used. Firstly, the heavy-ion cross-section of the memories is found experimentally and a Weibull function is fitted to the experimental data to obtain the relevant quantities for further analysis. These are the LET threshold Lo, the saturated cross-section value XSsat, the width parameter W and the shape parameter s. Then, energy deposition simulations are performed in FLUKA. Thereafter, the Weibull curve and the energy deposition curve obtained in FLUKA are folded for each primary beam energy simulation from FLUKA. Through this operation one obtains an estimation of the cross-section for different particle types, in this case electrons. The procedure for the folding is outlined in detail in [17]. The Weibull parameters for the SRAM mentioned in this work have been characterized previously in a heavy ion beam [13], [15] and can be seen summarized in table V.

The resulting cross-section estimates can be seen in Fig. 6 for Brilliance, Fig. 7 for ISSI and Fig.8 for Alliance. Although the memories all have different Weibull characteristics, the IRPP model used in this work should be a good estimate for the overall shape and cross-section for the memories. For the Brilliance memory the fit with the simulated cross-section is follows the overall shape and absolute value of the cross-section. The lower energy point also follows the theoretical decrease in cross-section well.

The ISSI memory follows the overall shape of the estimated cross-section curve well, however the absolute value of the experimental points is about a factor 4 higher than the simulated cross-section. This can be mainly attributed to by the fact that the IRPP model chosen for this work is very sensitive to the changes in the thickness of the sensitive volumes [15].

The Alliance result comparison with the simulated cross-section indicates that all the SEL upper limits are above the simulated cross-section which would explain why no SEL results were observed. In addition, the high onset LET value of $15\,\mathrm{MeVcm^2/mg}$ explains why the cross-section for this memory is lower compared to the other two memories. An additional limitation for reaching lower cross-sections with the Alliance SRAM is the TID onset limit described in section III-D. As an illustration the Weibull functions for the memories together with the relevant LET range for electrons ($13\,\mathrm{MeVcm^2/mg}$) and protons ($15\,\mathrm{MeVcm^2/mg}$) is plotted in Fig. 9. The heavy ion cross-section in this regions is about 2 magnitudes lower for the Alliance memory than for the ISSI and the Brilliance memories.

C. FLUKA Tungsten Fragment Simulation

To estimate the mechanism by which electrons are capable of producing SEL events, a tungsten nuclear fragment simulation was made. A pencil beam of either protons, photons or

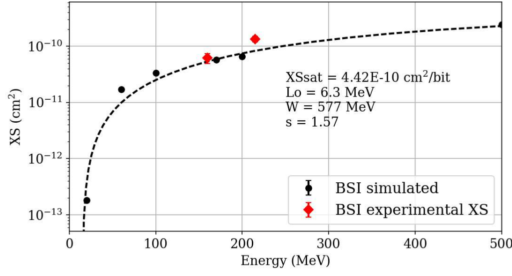

Fig. 6. The simulated SEL cross-section for BSI

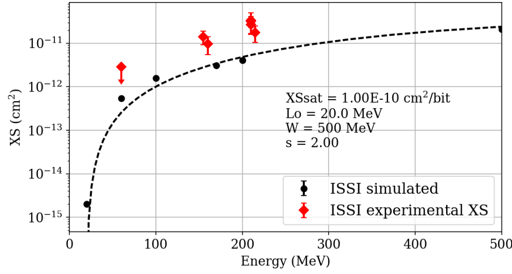

Fig. 7. The simulated SEL cross-section for ISSI

TABLE VI
INELASTIC INTERACTION CROSS-SECTION FOR ELECTRON, PHOTONS AND PROTONS USED TO NORMALIZE THE RESULTS OF THE FLUKA TUNGSTEN RECOIL SIMULATION

Energy (MeV)	Electron (mb)	Photon (mb)	Proton (mb)
50.0	0.325	2.1	578.0
200	0.648	3.98	403.0

electrons impinged on a cube of $5\,\mu\mathrm{m}$ side of tungsten. The quantities scored for the fragments are the LET in silicon, seen in Fig. 10, the charge, seen in Fig. 11 and the kinetic energy seen in Fig. 12. All these quantities were normalized to the inelastic interaction cross-section, as seen in Table VI.

The secondary fragments created in tungsten by protons, as can be seen in Fig. 10 have LETs up to $\sim 45\,\mathrm{MeVcm^2/mg}$. These fragments are shown to be responsible for the increase of cross-section in highly integrated circuits between $200\,\mathrm{MeV}$ and $500\,\mathrm{MeV}$ [2]. Fig. 10 also shows that the secondary fragments created by electrons in tungsten can have LETs up to $\sim 40\,\mathrm{MeVcm^2/mg}$. They are therefore theoretically capable to produce a similar increase in cross-section. Moreover, the highest LET values of the fragments created by electrons in tungsten is very similar to that of the protons. In addition, the tungsten enhancement effect creates a strong energy dependence for the maximum LET one can observe during electron testing. As seen in Fig. 10 on the left, at lower beam energies only silicon-like and tungsten-like secondary recoils are present.

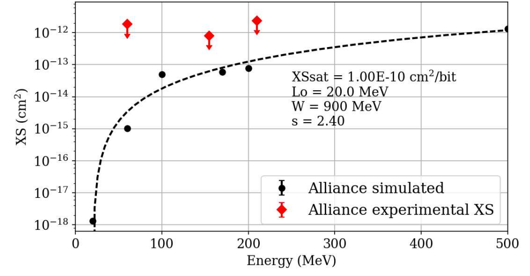

Fig. 8. The simulated SEL cross-section for Alliance

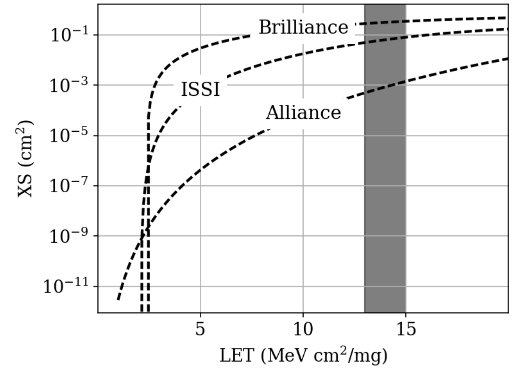

Fig. 9. The heavy ion Weibull functions of the tested SRAM. The shaded area represents the highest LET of recoils generated by electrons and protons and illustrates the difference in the cross section in this region.

V. RHA IMPLICATIONS

A possible strategy for assuring that components are free of proton induced SEL is to first test with heavy ions up to a given LET. For devices that do not include high-Z material this limit is set to $\sim 15\,\mathrm{MeVcm^2/mg}$. Due to the fact that high-Z materials interaction with protons creates high-LET fission fragments, it has been suggested that the heavy ion test should be performed with LET of at least $40\,\mathrm{MeVcm^2/mg}$ [2]. It was also suggested in [2] that to ensure that the component is completely SEL free for a given environment, one would have to test with the maximum energy of protons present in the environment. In this work it was shown that the photons and electrons are also capable of producing high-LET fragments of up to $40\,\mathrm{MeVcm^2/mg}$, however with a lower probability than protons. Therefore, in principle a similar guideline is relevant for electrons. If the environment the electronics is to be used in contains high-energetic electrons testing up to the aforementioned limit is also necessary in this case. The SEL cross-section for the memories in this work have a electron-induced SEL cross-section which is several magnitudes lower than for the equivalent proton cross-section. For the Brilliance memory, a proton saturation cross-section has been found to be $\sim 3 \times 10^{-7}\,\mathrm{cm^2}$ for protons [15], whereas for electron testing it was found to be $3.3 \times 10^{-10}\,\mathrm{cm^2}$. However, due to the HE electron facilities still being relatively rare, having quite a low flux and energy of electrons or are generally not built with electronics testing in mind, SEL testing at these facilities

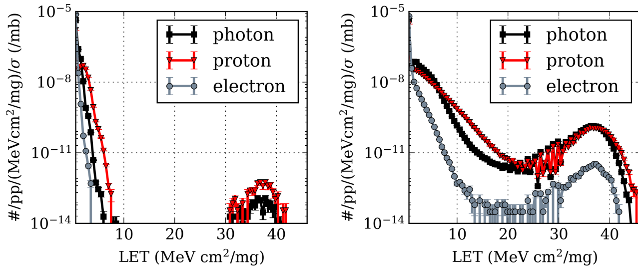

Fig. 10. Simulation of the LET of fragments generated by interaction with tungsten by protons, neutrons and photons. left) $50\,\mathrm{MeV}$ beam right) $200\,\mathrm{MeV}$ beam

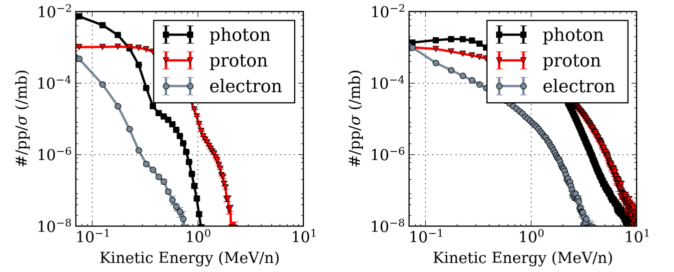

Fig. 12. Simulation of the kinetic energy of recoils generated by interaction with tungsten by protons, neutrons and photons. left) $50\,\mathrm{MeV}$ beam right) $200\,\mathrm{MeV}$ beam

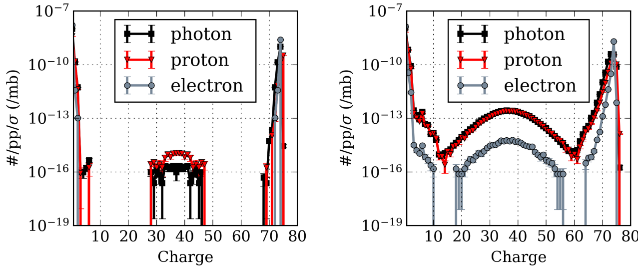

Fig. 11. Simulation of the atomic number of the fission fragments generated by interaction with tungsten by protons, neutrons and photons. left) $50\,\mathrm{MeV}$ beam right) $200\,\mathrm{MeV}$ beam

takes a long time and can be quite complicated. Therefore, an alternative approach is to perform the tests with protons instead since the produced fragments have similar LETs. Another advantage is that testing can be done in less time due to the lower fluence. However, this is not the case for direct-ionisation or elastic scattering, which have a higher cross-section than the indirect ionisation events. It was suggested in [2] that one has to consider the environment in which the device is to be operated in: the flux of the particles and the highest energy present in the environment, in which the device is to be used. The same consideration can be applied to electron testing, with the additional consideration that it is possible to substitute for proton testing instead. If the device is not sensitive to proton-induced SEL, it will not be sensitive to electron induced SEL.

VI. Future Work and Conclusions

In this work first experimental evidence showing electron induced-SEL has been shown. The DUTs had a LET threshold of $\sim 3\,\mathrm{MeVcm^2/mg}$ [14]. It has been shown through simulation in [6] that electrons and photons are capable of producing nuclear interaction product with a LET of up to $13\,\mathrm{MeVcm^2/mg}$ and $15\,\mathrm{MeVcm^2/mg}$ respectively. Therefore, the SEL observed in the DUT are attributed to these products. Moreover, a device with a LET onset value of $15\,\mathrm{MeVcm^2/mg}$ experienced no SEL events, which further implies that the recoils with high LETs are responsible for the SEL events.

It has been shown in [2] that the presence of high-Z materials in devices enhances the SEL cross-section for high energy protons. The fission fragments created by the proton and tungsten interaction can have a LET of up to $\sim 45\,\mathrm{MeVcm^2/mg}$. Similarly, it was shown in this work that electrons and photons are capable of producing fragments with a similar LET of up to $\sim 45\,\mathrm{MeVcm^2/mg}$, however with a much lower probability.

The experimental result comparison with the cross-section estimate obtained through FLUKA energy deposition simulations shows a good fit of the experimental data and simulation. The absolute value and the energy dependence were clearly seen in the Brilliance memory, the energy dependence was also seen on the ISSI memory. In addition, the ISSI memory was tested at different beam energies and the cross-section results were within the uncertainties from each other indicating no pile-up effect, which would imply an exponential increase in cross-sction with the energy [5].

Finally, as electrons and photons are shown to be capable of producing recoils with similar LET values, the implication to RHA is similar to the one suggested for protons in [2]: one should test with the highest energy present in the environment the device is to be used in. In addition, where heavy-Z materials are present fission fragment with LETs of up to $45\,\mathrm{MeVcm^2/mg}$. Therefore testing with heavy ions with LET values of at least $40\,\mathrm{MeVcm^2/mg}$ is advised [2]. Electrons and photons have been shown to produce fission fragments with similar LETs of up to $\sim 40\,\mathrm{MeVcm^2/mg}$. Therefore a similar approach is advised for electrons in order to cover the highest possible LET fragments generated. Proton testing can be seen as a suitable substitute since electrons, photons and protons produce fission fragments due to tungsten interaction and recoils due to beam-silicon interaction with similar LET values. The added benefit being the lower fluence and therefore time and cost needed for device qualification.

Acknowledgment

Sincere gratitude to Michele Muschitiello and Alessandra Costantino for their assistance with the Co60 testing at ESTEC. This work was supported by the CERN/ESA collaboration, the VESPER, CHARM and R2E groups at CERN and the European Space Agency (ESA/ESTEC Contract No. 4000115379/15/NL/MH/GM).

References

[1] J. R. Schwank, M. R. Shaneyfelt, P. E. Dodd, J. A. Felix, J. Baggio, V. Ferlet-Cavrois, P. Paillet, K. A. Label, R. L. Pease, M. Simons, and

L. M. Cohn, "Hardness assurance test guideline for qualifying devices for use in proton environments," in *IEEE Transactions on Nuclear Science*, vol. 56, no. 4, 2009, pp. 2171–2178.

[2] J. R. Schwank, M. R. Shaneyfelt, J. Baggio, P. E. Dodd, J. A. Felix, V. Ferlet-Cavrois, P. Paillet, D. Lambert, F. W. Sexton, G. L. Hash, and E. Blackmore, "Effects of particle energy on proton-induced single-event latchup," in *IEEE Transactions on Nuclear Science*, vol. 52, no. 6, 2005, pp. 2622–2629.

[3] M. A. Clemens, N. C. Hooten, V. Ramachandran, N. A. Dodds, R. A. Weller, M. H. Mendenhall, R. A. Reed, P. E. Dodd, M. R. Shaneyfelt, J. R. Schwank *et al.*, "The effect of high-z materials on proton-induced charge collection," *IEEE Transactions on Nuclear Science*, vol. 57, no. 6, pp. 3212–3218, 2010.

[4] M. A. Clemens, "Energy deposition mechanisms for proton- and neutron-induced single event upsets in modern electronic devices," Ph.D. dissertation, Vanderbilt University, 2012.

[5] M. J. Gadlage, A. H. Roach, A. R. Duncan, M. W. Savage, and M. J. Kay, "Electron-induced single-event upsets in 45-nm and 28-nm bulk CMOS SRAM-based FPGAs operating at nominal voltage," *IEEE Trans. Nucl. Sci.*, vol. 62, no. 6, pp. 2717–2724, 2015.

[6] M. Tali, R. Alia, M. Brugger, R. Corsini, W. Farabolini, V. Ferlet-Cavrois, A. Mohammadzadeh, G. Santin, and A. Virtanen, "High-energy Electron Induced SEUs and Jovian Environment Impact," *IEEE Trans. Nucl. Sci.*, vol. 64, no. 8, pp. 2016 – 2022, 2017. [Online]. Available: http://ieeexplore.ieee.org/document/7944600/

[7] M. P. King, R. A. Reed, R. A. Weller, M. H. Mendenhall, R. D. Schrimpf, B. D. Sierawski, A. L. Sternberg, B. Narasimham, J. K. Wang, E. Pitta, and Others, "Electron-induced single-event upsets in static random access memory," *IEEE Trans. Nucl. Sci.*, vol. 60, no. 6, pp. 4122–4129, 2013.

[8] JUICE Team, "JUICE environment specification," ESTEC/ESA, Noordwijk, Netherlands, Tech. Rep., 2015.

[9] D. M. Hiemstra and E. W. Blackmore, "LET spectra of proton energy levels from 50 to 500 MeV and their effectiveness for single event effects characterization of microelectronics," *IEEE Trans. Nucl. Sci.*, vol. 50, no. 6, pp. 2245–2250, 2003.

[10] A. Ferrari, P. R. Sala, A. Fasso, and J. Ranft, "FLUKA: a multi-particle transport code," No. INFN-TC-05-11, 2005. [Online]. Available: doi.org/10.5170/CERN-2005-010

[11] T. T. Böhlen, F. Cerutti, M. P. W. Chin, A. Fasso, A. Ferrari, P. G. Ortega, A. Mairani, P. R. Sala, G. Smirnov, and V. Vlachoudis, "The FLUKA code: developments and challenges for high energy and medical applications," *Nucl. Data Sheets*, vol. 120, pp. 211–214, 2014.

[12] R. G. Alía, C. Bahamonde, S. Brandenburg, M. Brugger, E. Daly, V. Ferlet-Cavrois, R. Gaillard, S. Hoeffgen, A. Menicucci, S. Metzger, and Others, "Sub-LET threshold SEE cross section dependency with ion energy," *IEEE Trans. Nucl. Sci.*, vol. 62, no. 6, pp. 2797–2806, 2015.

[13] R. G. Alía, M. Brugger, S. Danzeca, V. Ferlet-Cavrois, C. Poivey, K. Røed, F. Saigné, G. Spiezia, S. Uznanski, and F. Wrobel, "Energy dependence of tungsten-dominated SEL cross sections," *IEEE Trans. Nucl. Sci.*, vol. 61, no. 5, pp. 2718–2726, 2014.

[14] R. Garcia Alia, C. Bahamonde, S. Brandenburg, M. Brugger, E. Daly, V. Ferlet-Cavrois, R. Gaillard, S. Hoeffgen, A. Menicucci, S. Metzger, A. Zadeh, M. Muschitiello, E. Noordeh, and G. Santin, "Sub-LET Threshold SEE Cross Section Dependency with Ion Energy," in *IEEE Transactions on Nuclear Science*, vol. 64, no. 1, 2017, pp. 388 – 397.

[15] R. G. Alía, E. W. Blackmore, M. Brugger, S. Danzeca, V. Ferlet-Cavrois, R. Gaillard, J. Mekki, C. Poivey, K. Røed, F. Saigne, G. Spiezia, M. Trinczek, S. Uznanski, and F. Wrobel, "SEL cross section energy dependence impact on the high energy accelerator failure rate," *IEEE Transactions on Nuclear Science*, vol. 61, no. 6, pp. 2936–2944, 2014.

[16] E. Petersen, "Soft error results analysis and error rate prediction," in *IEEE NSREC Short Course*, 2008.

[17] R. G. Alía, M. Brugger, S. Danzeca, V. Ferlet-Cavrois, C. Poivey, K. Røed, F. Saigné, G. Spiezia, S. Uznanski, and F. Wrobel, "Energy dependence of tungsten-dominated SEL cross sections," *IEEE Trans. Nucl. Sci.*, vol. 61, no. 5, pp. 2718–2726, 2014.